COLOSSAL ELECTRORESISTANCE, MAGNETOIMPEDANCE, AND MAGNETOCALORIC EFFECTS IN SELECTED MANGANITES

ALWYN REBELLO

NATIONAL UNIVERSITY OF SINGAPORE

2010

COLOSSAL ELECTRORESISTANCE, MAGNETOIMPEDANCE AND MAGNETOCALORIC EFFECTS IN SELECTED MANGANITES

ALWYN REBELLO

(*M. Sc., Cochin University of Science And Technology, India*)

A THESIS SUBMITTED

FOR THE DEGREE OF DOCTOR OF PHILOSOPHY IN SCIENCE

DEPARTMENT OF PHYSICS

NATIONAL UNIVERSITY OF SINGAPORE

2010

ACKNOWLEDGEMENTS

I would like to express my sincere gratitude to my supervisor *Asst. Prof. Ramanathan Mahendiran*. I am grateful to him for imparting the knowledge of low temperature physics and introducing me to the exciting world of experimental physics. I have been motivated and inspired by him throughout the course of my Ph.D. His expertise and integral view towards research has helped me to tackle several difficult problems of my project and overcome the "uncertainties" of being the first graduate student of the lab. This thesis would not have been possible without his expert guidance, encouragement and continuous support.

I would like to thank *Prof. B.V.R. Chowdari* and *Prof. G.V. Subba Rao* for allowing me to use Advanced Battery Lab space in the early stage of my Ph.D. Also, *Prof. Rao*'s constructive comments on an important project in my Ph.D were very helpful.

My appreciation goes to *Dr. C. Krishnamoorthy, Dr. N. Sharma, Dr. Rucha P. Desai, and Dr. C. Raj Sankar* for helpful discussion and sharing of knowledge at different stages of this study. I am also thankful to all technical and administrative staff in the Physics department for their invaluable help.

I owe a deep sense of gratitude to all my colleagues in the lab [*Sujit, Vinayak, Suresh, Aparna, Mark, Zhuo Bin, Alex and Tan Choon Lye*] for their generous support and immense help provided throughout the period of my research work. I am indebted to all of them for creating a cheerful and cooperative working atmosphere in the lab.

I acknowledge National University of Singapore (NUS) and Faculty of Science for providing graduate student fellowship and president graduate fellowship.

Most importantly, I feel a deep sense of gratitude to my father *Charles Rebello* and my mother *Jain Gonsalvez*, to whom I dedicate this thesis. My thanks also go to my siblings (*Sini, Sinda, Ashly, Alex, Ashwin and Arun*) for the inspiration, prayers and affection shown to me. Last but not least, I thank *Vinitha* for always encouraging me to be optimistic at times of adversities in research.

TABLE OF CONTENTS

SUMMARY

Mn- based oxides (manganites) have attracted a huge attention since the discovery of colossal magnetoresistance (CMR), wherein a spectacular change in resistivity is observed under an external magnetic field. In this thesis, investigation of other intriguing properties such as colossal electroresistance, magnetoimpedance and magnetocaloric effect in selected manganites are presented.

Colossal electroresistance (CER), which refers to a huge change in the resistivity of a sample or resistivity switching induced by an electric field/current, is one of the hottest topics in applied physics and can be exploited for nonvolatile memory devices in future era of device miniaturization. Nevertheless, the physics behind the CER is poorly understood so far, in spite of considerable experimental and theoretical efforts. A comprehensive study of both direct and pulsed current induced electrical resistivity changes in a few manganese based oxides are presented in this thesis work. Various exotic current induced behaviors such as negative differential resistance, magnetoresistance avalanche and first order insulator to metal transition are also observed. Most importantly, concomitant changes in surface temperature of the samples were measured during the electroresistance experiments, which are not previously measured explicitly by many authors. A quantitative study is carried out to understand the role of joule heating and other intrinsic mechanisms, which account for the electroresistance in manganites of different electronic and magnetic ground states.

The practical applications of CMR are hindered by the requirement of a huge magnetic field ($\mu_0 H$> 1 T) to get a magnetoresistance (MR) of more than -10 %. An alternative approach to obtain a considerable MR is presented in this study, wherein both the resistive (R) and inductive reactance (X) of the complex electrical impedance ($Z = R+jX$) have been studied as a function of magnetic field over a wide frequency and temperature range. Interestingly, a huge ac magnetoresistance (-51 %) at 2 MHz, is obtained in a small magnetic field of 200 mT at room temperature in $La_{0.7}Sr_{0.3}MnO_3$. Our study of magnetoimpedance in this manganite reveals an unusual field dependence of the ac magnetoreactance. The

dependence of magnetoimpedance features on the measurement geometry is studied and plausible explanations to the observed intriguing features are discussed.

Magnetic refrigeration based on magnetocaloric effect, wherein a magnetic field induced change occurs in the magnetic entropy or adiabatic temperature, is a challenging topic of research from the view points of both fundamental physics as well as application. While majority of the published work in manganites focus on magnetic entropy change across the second-order phase transition (paramagnetic to ferromagnetic), we present a different approach to enhance the magnetocaloric effect. A large magnetocaloric effect is observed in $Sm_{1-x}Sr_xMnO_3$ (x = 0.3-0.5) due to the presence of magnetic nanoculsters, which preexist in the paramagnetic state. We demonstrate that magnetic oxides with nanoscale phase separation, particularly those with interacting superparamagnetic clusters in the paramagnetic phase, can be good candidates for magnetic refrigeration.

LIST OF PUBLICATIONS

Articles

- A. Rebello, and R. Mahendiran, "*Current driven discontinuous insulator-metal transition and low-field colossal magnetoresistance in $Sm_{0.6}Sr_{0.4}MnO_3$"*, **Appl. Phys. Lett.** 96, 152504 (2010).

- A. Rebello, and R. Mahendiran, "*Influence of length and measurement geometry on magnetoimpedance in $La_{0.7}Sr_{0.3}MnO_3$*", **Appl. Phys. Lett.** 96, 032502 (2010).

- A. Rebello, and R. Mahendiran, "*Current-induced magnetoresistance avalanche in $Nd_{0.5}Ca_{0.5}Mn_{0.95}Ni_{0.05}O_3$"*, **Solid. State. Commun.** 150, 961 (2010).

- A. Rebello, and R. Mahendiran, "*Magnetothermal cooling with a phase separated manganite"*, **Appl. Phys. Lett.** 95, 232509 (2009).

- A. Rebello, V. B. Naik, and R. Mahendiran, "*Huge ac magnetoresistance of $La_{0.7}Sr_{0.3}MnO_3$ in subkilogauss magnetic fields*", **J. Appl. Phys**. 106, 073905 (2009).

- V. B. Naik**,** A. Rebello, and R. Mahendiran, "*A large magnetoinductance effect in $La_{0.67}Ba_{0.33}MnO_3$*", **Appl. Phys. Lett.** 95, 082503 (2009).

- A. Rebello, and R. Mahendiran, "*Unusual field dependence of radio frequency magnetoimpedance in $La_{0.67}Ba_{0.33}MnO_3$*", **Euro. Phys. Lett.** 86, 27004 (2009).

- A. Rebello, and R. Mahendiran, "*Current induced electroresistance in $Nd_{0.5}Ca_{0.5}Mn_{0.95}Ni_{0.05}O_3$*", **Solid. State. Commun.** 149, 673 (2009).

- A. Rebello, C. L. Tan, and R. Mahendiran, "*Low-field magnetoimpedance in $La_{0.7}Sr_{0.3}MO_3$ (M = Mn, Co)*", **Solid. State. Commun.** 149, 1204 (2009).

- A. Rebello, and R. Mahendiran, "*Pulse width controlled resistivity switching at room temperature in $Bi_{0.8}Sr_{0.2}MnO_3$*", **Appl. Phys. Lett.** 94, 112107 (2009).

- A. Rebello, and R. Mahendiran, "*Composition dependence of magnetocaloric effect in $Sm_{1-x}Sr_xMnO_3$ (x=0.3–0.5)*", **Appl. Phys. Lett.** 93, 232501 (2008).

- S. K. Barik, A. Rebello, C. L. Tan, and R. Mahendiran, "*Giant magnetoimpedance and high frequency electrical detection of magnetic transition in $La_{0.75}Sr_{0.25}MnO_3$*", **J. Phys. D: Appl. Phys.** 41, 022001 (2008).

- A. Rebello, and R. Mahendiran, "*Spatial dependence of magnetoimpedance in $La_{0.67}Ba_{0.33}MnO_3$*", submitted to **Solid. State. Commun.** (2010).

- A. Rebello, and R. Mahendiran, "*Effects of direct and pulsed current on electrical transport and abrupt magnetoresistance in $Sm_{1-x}Sr_xMnO_3$* (x= 0.3, and 0.4)", submitted to **J. Appl. Phys.** (2010).

- A. Rebello, and R. Mahendiran, "*Anomalous ac magnetotransport in $Sm_{0.6}Sr_{0.4}MnO_3$*", submitted to **J. Appl. Phys.** (2010).

Conference Proceedings

- A. Rebello, and R. Mahendiran, "*Composition dependence of magnetocaloric effect in $Sm_{1-x}Sr_xMnO_3$ (x = 0.3-0.5)*", ICMAT, *Singapore* (2009).

- A. Rebello, and R. Mahendiran, "*Current-induced electroresistance in $Nd_{0.5}Ca_{0.5}Mn_{0.95}Ni_{0.05}O_3$*", ICMAT, *Singapore* (2009).

- A. Rebello, and R. Mahendiran, "*Negative differential resistance and current-induced multilevel resistivity switching in $Nd_{0.5}Ca_{0.5}MnO_3$ and La_2NiMnO_6*", AsiaNano Conference, Biopolis, Singapore (2008).

- A. Rebello, and R. Mahendiran, "*Room temperature giant magnetoimpedance in manganese oxides: Intrinsic and Extrinsic effects*", 3rd MRS-S Conference on Advanced Materials, IMRE, Singapore (2008).

- A. Rebello, V. B. Naik, S. K. Barik, M. C. Lam, and R. Mahendiran, "*Giant magnetoimpedance in oxides*", MRS-Spring, San Francisco (2010).

LIST OF TABLES

LIST OF FIGURES

LIST OF SYMBOLS

R	Resistance
ρ	Resistivity
σ	Conductivity
T	Temperature
T_S	Surface temperature
G	Effective thermal conductance
t	Time
V	Voltage
e	Electronic charge
I	Current
X	Reactance
L	Inductance
Z	Electrical impedance
M	Magnetization
H	Magnetic field
μ	Magnetic permeability
μ_0	Permeability of free space
μ_ϕ	Circumferential permeability
f	frequency
k_B	Boltzmann constant
δ	Skin depth
ε	Dielectric permittivity
ω	Angular frequency
S	Magnetic entropy
C	Curie Weiss constant
P_{eff}	Effective magnetic moment

C_p	Heat capacity
m	Mass

Chapter 1

Introduction

Multi-functionality is one of the main objectives of present generation material research, owing to the fascinating fundamental physics and technological significance involved. In particular, oxides have attracted a lot of attention in the past few decades since they show various exotic and versatile properties, such as colossal magnetoresistance, high temperature superconductivity, colossal electroresistance, metal-insulator transition, phase separation, charge, orbital and spin ordering, multiferroism (coexistence of ferromagnetic and ferroelectric ordering) etc. [1]. The intricate and delicate competitions between various degrees of freedom in oxides have been subjected to intense studies, in order to understand their electronic and magnetic properties. The spectacular sensitivity of various properties of these materials to different external stimuli like magnetic field, electric field, pressure, light, etc. offers numerous possibilities to exploit them for practical applications as multifunctional materials. Nowadays, one of the most striking challenges of solid state physics is to understand these intricate properties of transition metal compounds.

In this chapter, a brief state of the art review about the rich properties of manganese based oxides (manganites) and an overview of research activities in these materials are presented. The chapter is organized as follows. After a brief introduction on manganites, we discuss a few exotic phenomena like charge ordering, phase separation and related features in manganites. Following, we present a summary of colossal electroresistance (CER) effect in manganites, mainly focusing on the different characteristics of CER and proposed mechanisms. Next, a concise description on the ac counterpart of magnetoresistance, namely magnetoimpedance is provided. Then, a short review on magnetocaloric effect is presented. Finally, the scope and objectives of the work presented in this thesis are outlined and the chapter ends with a brief note on the organization of the rest of the thesis. The issues turned up with respect to the aforementioned effects investigated in selected manganites, in the present study, are emphasized in the introduction of the corresponding chapters.

1. 1 Brief introduction to manganites

1. 1. 1 Perovskites

A large family of transition metal oxides is known as the perovskites, which derive their name from a mineral $CaTiO_3$ and named after Russian mineralogist, L. A. Perovski. The general chemical formula of perovskites is ABX_3, where *A*-site is generally occupied by large cations such as rare earth ions or alkaline earth metal ions, *B*-site by smaller cations such as transition metal ions and *X* is an anion, usually oxide or halide. The structure of perovskite with highest symmetry is cubic, as shown in Fig. 1. 1(a). In a perovskite oxide (*X*=O), the picture of a basic structural unit can be easily visualized as: A set of BO_6 octahedra are linked together by corner-shared oxygen atoms, with *A* atoms occupying the space in between [Fig. 1. 1(b)]. The two major landmarks in the history of perovskite oxides are: (i) in 1986, Alex Müller and Georg Bednorz discovered high-temperature superconductivity in copper-based perovskite oxides[2] (ii) a few years after this, in 1993, more excitement greeted reports that certain manganese oxides, belonging to the perovskite structure showed a huge change in electrical resistivity when a magnetic field was applied [3]. This effect is generally known as magnetoresistance, but the resistivity change observed in these oxides was so large that it could not be compared with any other forms of magnetoresistance. The effect observed in these materials – the manganese perovskites – was therefore dubbed "colossal magnetoresistance (CMR)" to distinguish it from the giant magnetoresistance observed in magnetic multilayers.

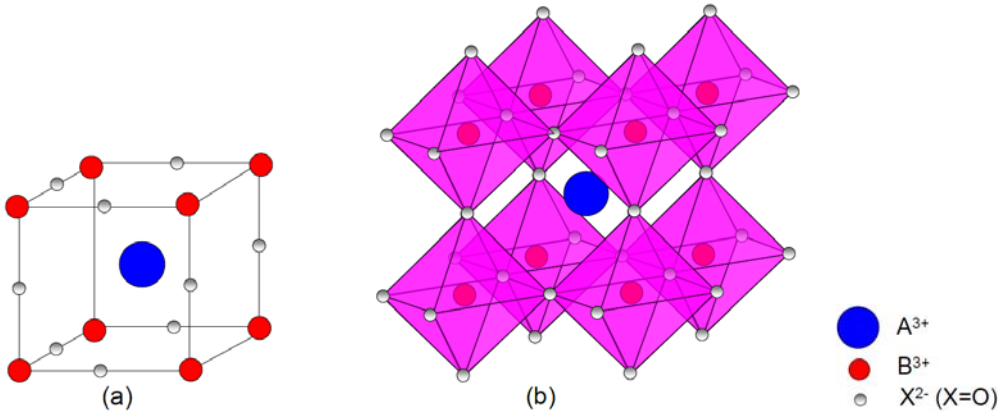

Fig. 1. 1: Schematic of (a) Cubic perovskite (ABX_3) and (b) BO_6 Octahedra

1. 1. 2 Important physical features of CMR manganites

1. 1. 2. 1 Crystallographic structure:

Manganites, of the general chemical formulae $RE_{1-x}AE_xMnO_3$ where *RE* is a rare earth element and *AE* is an alkaline earth element, has attracted a lot of attention both from the fundamental and technological point of view. The discovery of CMR in these materials raised expectations of a new generation of magnetic devices and sensors, and launched a frenetic scientific race to understand the cause of the effect. Today, the promise of great strides in technology remains a challenge, but these materials are receiving a lot of attention in their own right. The structure of $RE_{1-x}AE_xMnO_3$ is close to that of the cubic perovskite (ABX_3, where *A* is trivalent *RE* or divalent *AE* atom, *B* is Mn atom and *X* is O atom). The large sized *RE* trivalent ions and *AE* divalent ions occupy the *A*-site with 12-fold oxygen coordination. The smaller Mn ions in the mixed-valence state Mn^{3+}–Mn^{4+} are located at the centre of an oxygen octahedron, the *B*-site with 6-fold coordination. For a stoichiometric oxide, the proportions of Mn ions in the valence states 3+ and 4+ are respectively, 1–*x* and *x*. The structure of the manganites is governed by the tolerance factor [4],

$$t = (r_{Mn} + r_O)/\sqrt{2}(r_A + r_O)$$

Here, r_j (j= *A*, *B*, O) represents the (averaged) ionic size of each element and *t* measures the deviation from perfect cubic symmetry (t = 1). Generally, *t* differs appreciably from 1 and the manganites have, at least at low temperature, a lower symmetry (rhombohedral or orthorhombic structure). A possible characteristic distortion which influences the perovskite structure arises from the *A*-site size mismatch. The Mn-O-Mn bond angle is sensitive to the size of the A-site ion and is reduced from 180˚. The schematic of the distortion of structure due to A-site cation size mismatch is shown in Fig. 1. 2.

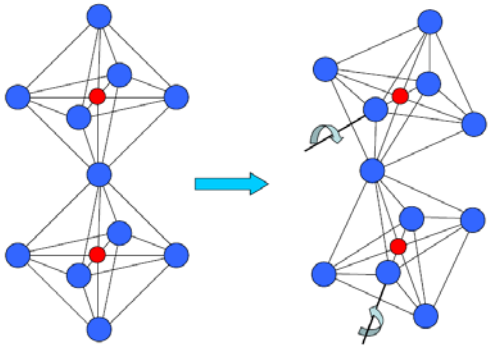

Fig. 1. 2: The buckling distortion due to A-site cation size mismatch.

1. 1. 2. 2 Electronic structure and orbital ordering:

The simple non-substituted perovskite compounds $L\mathrm{MnO_3}$, where L= La, Nd, Pr, etc. are insulators. In $\mathrm{LaMnO_3}$, for example, both the lanthanum and manganese are trivalent cations, and their combined charge is balanced by the oxygen ions. An isolated 3d Mn^{3+} ion has four electrons in its outermost energy level, and five degenerated orbital states (the schematic is shown in Fig. 1. 3) are available to the 3d electrons with l = 2. In a crystal, the degeneracy is partly lifted by the crystal field, which is an electric field derived from neighboring atoms in the crystal. In crystal field theory, the neighboring orbitals are modeled as negative point charges where the size and nature of crystal field effects depend crucially on the symmetry of the local octahedral environment [5].

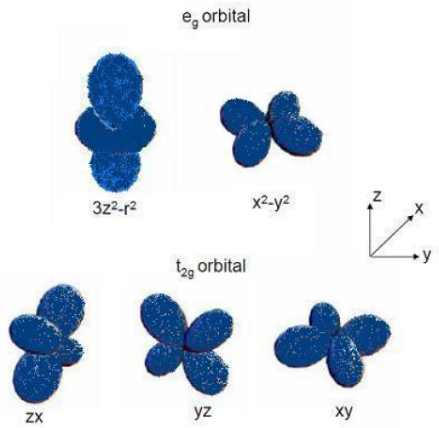

Fig. 1. 3: Five d orbitals. In the cubic crystal field, this fivefold degeneracy is lifted to two e_g orbitals [$(3z^2 - r^2)$ and $(x^2 - y^2)$] and three t_{2g} orbitals [(zx), (yz), and (xy)].

In an octahedral environment, the five d-orbitals are split by a crystal field into three t_{2g} orbitals (d_{xy}, d_{yz}, d_{xz}) and two e_g orbitals ($d_{3z^2-r^2}$ and $d_{x^2-y^2}$). For the MnO_6 octahedron in $LaMnO_3$, the energy difference due to crystal field splitting between the t_{2g} and the e_g levels is approximately 1.5 eV (the schematic is shown in Fig. 1. 4) [6]. The intra-atomic correlations ensure parallel alignment of the electron spins (first Hund's rule) for the Mn^{3+} and Mn^{4+} ions; the corresponding exchange energy of about 2.5 eV being larger than the crystal field splitting. The electronic configuration of Mn^{3+} is $3d^4$, $t_{2g}^{3\uparrow}\, e_g^{\uparrow}$ with $S = 2$ whereas Mn^{4+} is $3d^3$, $t_{2g}^{3\uparrow}$ with $S = 3/2$. The system chooses a ground state with effective magnetic moment,

$$\mu_{eff} = 2\mu_B\sqrt{(S(S+1))}.$$

Here L = 0 (so that J=S, $g_J = 2$) due to orbital quenching in 3d ions, where the crystal field interaction is much stronger than the spin orbit interaction. Their respective magnetic moments are $4\mu_B$ and $3\mu_B$, neglecting the small orbital contribution.

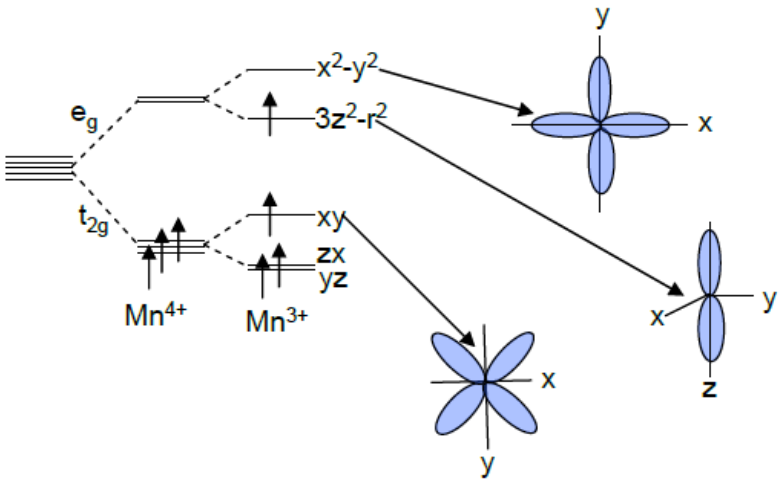

Fig. 1. 4: Energy levels and orbitals of Mn^{4+} and Mn^{3+} in a crystal field of octahedral symmetry and with axial elongation.

In a crystal field of symmetry lower than cubic, the degeneracy of the e_g and t_{2g} levels is lifted (Fig. 1. 4) for an axial elongation of the oxygen octahedron [7]. Although the energy of Mn^{4+} remains unchanged by such a distortion, the energy of Mn^{3+} is lowered. Thus, Mn^{3+} has a marked tendency to distort its octahedral environment in contrast to Mn^{4+}. The energy

cost of increased elastic energy is balanced by a resultant electronic energy saving due to the distortion; this phenomenon is known as the Jahn-Teller (JT) effect.

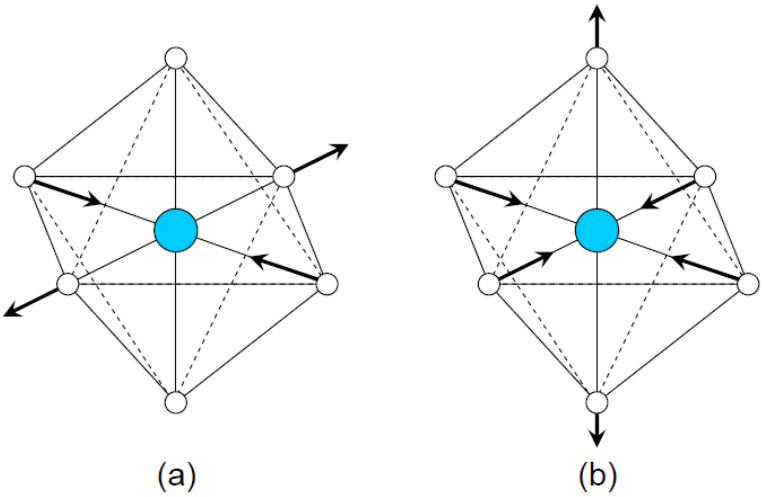

Fig. 1. 5: The relevant modes of vibration are (a) *Q*2 and (b) *Q*3 for the splitting of the e_g doublet (Jahn–Teller distortion).

As far as manganites are concerned there are 21 degrees of freedom (modes of vibration) for the movement of oxygen and Mn ions [8]. Out of these, only two types of distortion (modes of vibrations) are relevant for the splitting of the e_g doublet, i.e. JT distortion: *Q*2 and *Q*3 [7], which are shown in Fig. 1. 5. *Q*3 is a tetragonal distortion, which results in elongation or contraction of MnO_6 octahedra. In this case, either $d_{x^2-y^2}$ or $d_{3z^2-r^2}$ orbital will be filled preferentially. However, in the case of manganites the effective distortion is the basal plane distortion (called the *Q*2 mode) in which one diagonally opposite O pair is displaced outwards and the other pair displaced inward. In this case a certain superposition of $d_{x^2-y^2}$ and $d_{3z^2-r^2}$ orbitals is obtained [9], resulting in a rod-type or cross-type orbital ordering (Fig. 1. 6). These Jahn-Teller distortions are not independent from one Mn^{3+} site to another (cooperative Jahn-Teller effect) and a long range ordering is established throughout the whole crystal, which is also accompanied by a long range ordering of the orbital degree of freedom [7, 9]. In such a Jahn-Teller-distorted and orbital-ordered state, $LaMnO_3$ undergoes an antiferromagnetic transition at 120 K, where the spin-ordering structure is layer type (i.e. *A*-type, in which the ferromagnetic *xy* planes are coupled antiferromagnetically along the *z*-axis). The Jahn-Teller distortions, other than due to the *A* site mismatch, is rather effective in

the lightly doped manganites, i.e. with a large concentration, 1-*x*, of Mn^{3+} ions. On increasing the Mn^{4+} content, the Jahn–Teller distortions are reduced and the stabilization of the $3_{z^2-r^2}$ e_g orbital becomes less effective.

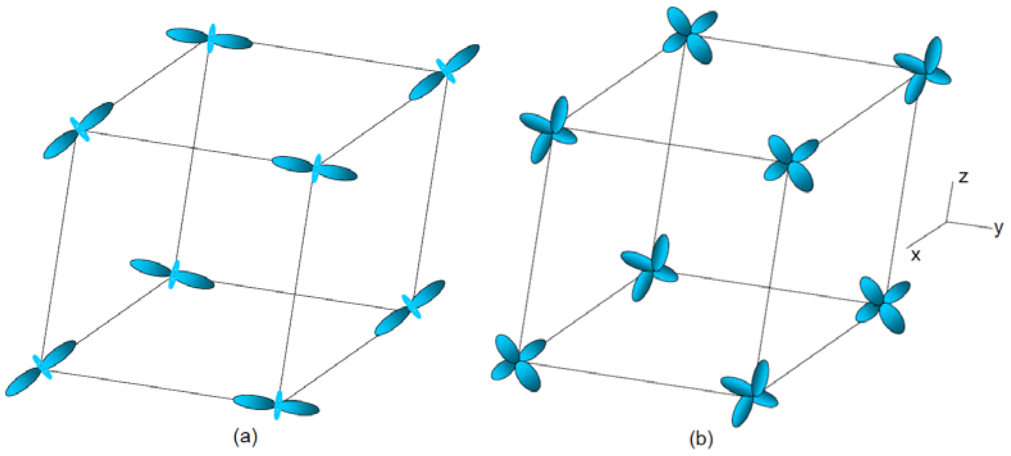

Fig. 1. 6: Schematic representation of (a) rod-type and (b) cross-type orbital ordering.

1. 1. 2. 3 Electrotransport in hole doped manganites and Colossal Magnetoresistance (CMR)

All the 3d (e_g and t_{2g}) electrons are subjected to electron repulsion interaction or the electron correlation effect and therefore tend to localize in the 100 % Mn^{3+} based parent compound, forming the so called Mott insulator [10]. The hole doping creates mobile Mn^{4+} species on the Mn sites, so that e_g electrons can be itinerant and hence play a role of conduction electrons. On the contrary, the t_{2g} electrons are stabilized by the crystal field splitting and regarded as always localized, forming the local spin (S=3/2) even in the metallic state. There exists an effective strong coupling between the e_g conduction electron spin (S=1/2) and t_{2g} localized spin following Hund's rule. In manganites, the exchange energy J_H (Hund's-rule coupling energy) exceeds the inter-site hopping interaction t^0_{ij} of the e_g electron between the neighboring sites, *i* and *j*. In this strong coupling limit, when $J_H >> t_{ij}$, the effective hopping interaction of the conduction electron is expressed as [11],

$$t_{ij} = t^0_{ij}\cos(\theta_{ij}/2).$$

This relation implies that the hopping depends on the relative angle (θ_{ij}) between the neighboring (classical) spins or the relative configuration of local spins (Fig. 1. 7) and the

ferromagnetic state is stabilized when the kinetic energy of the conduction electron is maximum (θ_{ij} =0). The ferromagnetic interaction via the exchange of the (conduction) electron was put forward by Zener in 1951 as the double exchange (DE) interaction [12]. Above or near T_C, the spins are dynamically disordered, thus reducing the effective hopping interaction and in turn increase the resistivity. Under an external magnetic field, the local spins are relatively aligned and this results in an increase in the effective hopping interaction. Thus the colossal magnetoresistance around T_C in manganites can be intuitively explained on the basis of double exchange model.

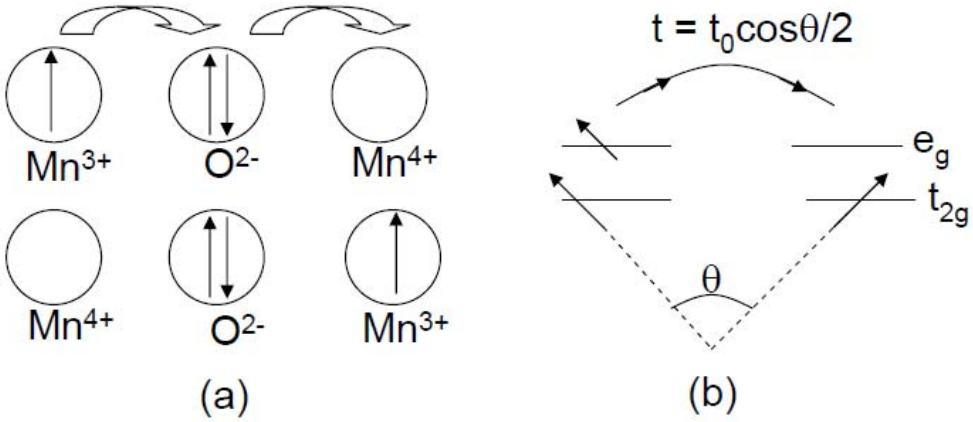

Fig. 1. 7: (a) Schematic representation of the double exchange mechanism proposed by Zener (b) sketch of de Gennes spin-canted states.

(a) $La_{1-x}Sr_xMnO3$: a canonical case

The properties of substituted lanthanum manganites, of the general formula $La_{1-x}AE_xMnO_3$ (AE = Ca, Sr, etc.), depend on the concentration of dopants (x) and the temperature [1]. For instance, x determines the magnetic and electronic ground states of $La_{1-x}Sr_xMnO_3$ (i.e., when AE = Sr). This compound is the most canonical double exchange system which shows the largest one electron bandwidth W, and accordingly less significantly affected by the electron-lattice and coulomb correlation effects. The hole- doping (substitution of La with Sr) is interpreted to favor the DE-type ferromagnetic coupling, producing the spin canting [13]. The spin canting angle continuously increases with increasing x, thereby transforming the canted antiferromagnetic phase (up to x=0.15) to ferromagnetic phase (for

x>0.15). With further doping, the Curie temperature T_C steeply increases, up to x= 0.3 and then saturates. The ferromagnetic transition temperatures (T_C) of the divalent substituted compositions are found to be highly susceptible to the amount of substitution and a fine-tuning of T_C is possible by varying the degree of substitution. Apart from the divalent ion substitution, self-doping and substitution at Mn-site by other transition metal ions are also known to cause rich variety of magnetic and transport properties in the lanthanum manganite family [1].

Urushibara *et al*. [14] has studied the temperature dependence of resistivity (ρ) of $La_{1-x}Sr_xMnO_3$ ($0<x<0.4$) in detail. In the samples $x<0.3$, the resistivity is reported to show a semiconductor behavior above T_C with $d\rho/dT< 0$, but at temperatures lower than T_C, a metallic behavior with $d\rho/dT > 0$. For the x=0.175 crystal, it was shown that the resistivity decreased steeply around T_C under the application of an external magnetic field. The magnetoresistance value is defined as

$$MR = [\rho(H)- \rho(0)]/\rho(0).$$

The magnetization (M) dependence of the MR at a temperature near above T_C is well expressed by a scaling function as

$$-[\rho(H)- \rho(0)]/\rho(0) = C(M/M_s)^2,$$

where M_s is the saturation magnetization in the ground state. The scaling constant C measures the effective coupling between the e_g conduction electron and the t_{2g} local spin. The magnitude of the MR has a close relation to the magnetization even in polycrystalline samples, showing a quadratic dependence [15]. There are two aspects to the field dependence in polycrystalline samples, where MR changes rapidly with H for low magnetic fields, followed by a gradual change at higher magnetic fields. One aspect is related to the ferromagnetic domain wall movement as in all ferromagnets and the other has to do with the grain boundaries which contribute substantially to the MR of manganites at $T << T_C$. It is interesting that the two distinct regimes seen in the MR-H curves for polycrystalline samples

at $T << T_C$ is generally absent in single crystals, where the magnitude of the MR increases almost linearly with H.

An important issue directly relating to the CMR effect is a semiconducting or insulating behavior above T_C in the low-x region, e.g. x=0.15-0.20 of $La_{1-x}Sr_xMnO_3$ or in narrower-W systems such as $La_{1-x}Ca_xMnO_3$. In such an x region, the negative MR effect is most pronounced around T_C and hence the origin of the semiconducting transport is of great interest. Millis *et al*. [16] pointed out that the resistivity of the low-doped crystals above T_C is too high to be interpreted in terms of the simple DE model and ascribed its origin to the dynamic Jahn-Teller distortion. Another possible origin of the resistivity increase near above T_C and the effective suppression by an external magnetic field has been ascribed to the Anderson localization of the DE carriers arising from the inevitably present random potential in the solid solution system [17], or to antiferromagnetic spin fluctuation which competes with the DE interaction [18]. An important issue relating to these instabilities is how we can take into account the orbital degree of the freedom of the e_g-state electrons and their possible strong inter-site correlation or coupling to the lattice degree of freedom. Goodenough pointed out that ferromagnetism is governed not only by double exchange, but also by the nature of the indirect superexchange interactions [19]. According to Goodenough-Kanamori rules, the Mn^{3+}-O-Mn^{4+} superexchange interaction is ferromagnetic while the Mn^{3+}-O-Mn^{3+} and Mn^{4+}-O-Mn^{4+} interactions are both antiferromagnetic. Antiferromagnetic superexchange coupling exists between Mn^{4+} ions via intervening oxygen, but the superexchange interaction with a Mn^{3+} ion can be antiferromagnetic or ferromagnetic depending on the relative orbital orientation. Therefore, it is expected that there exists a close interplay among charge carriers, magnetic couplings, and structural distortions in the mixed valent manganites.

1. 2 Charge ordering in correlated materials

An electron in a solid, if bound or nearly localized on a particular atom, can be described by three attributes; its charge (e^-), spin (S = ±1/2) and orbital. If correlations between different orbitals may be neglected, solving the problem of one of the orbitals is

often equivalent to solving the whole system. These orbitals hybridize to form a valence band. This so called one-electron picture ignores both intersite (like the Coulomb repulsion U) and even some intrasite correlations between the electrons (i. e., the charge transfer between O 2p and transition metal 3d states Δ). Nonetheless, the single electron approach has been very successful for the description of many of the properties of periodic solids. However, electronic correlations are responsible for some of the most fascinating properties such as superconductivity or magnetism in transition metal compounds. The strong correlations between the electrons in transition metal oxides classifies them as Mott insulators, where the ground state is mostly antiferromagnetic; however it is not the magnetic interactions that drive these materials into the insulating state. Rather it is the coulomb repulsions, which are still in operation even in the case of paramagnetic state. In doped manganites like $La_{1-x}Ca_xMnO_3$, the ionic radius of Ca is less than that of Sr, and hence the doping introduces more distortion into the crystal structure, thus reducing the bandwidth. Instead of the typical double exchange behaviour in the Sr doped manganite, a more complicated situation arises. We have already seen that spin-ordering and orbital-ordering play important roles in manganites. Now, we discuss the presence of charge ordering, which makes the physics of manganites more rich and complex.

1. 2. 1 Ordering phenomenon

Charge ordering is a phenomenon observed in solids wherein electrons become localized due to the ordering of cations of differing charges (oxidation states) on specific lattice sites. It can occur in widely different systems, ranging from wholly localized systems such as alkali halide ionic crystals to a wholly delocalised one such as the electron crystallization envisaged by Wigner. For an ordinary delocalized system of electrons, the kinetic energy due to the Pauli Exclusion Principle is much more important than the potential energy due to the coulomb repulsion. However the situation drastically changes when the electron concentration is low, when the potential energy becomes larger than the kinetic energy. In this situation, the kinetic energy will maintain the zero point motion of electrons around the equilibrium position and change the homogeneous state into an inhomogeneous

charge distribution, known as Wigner crystallization. This renders the material insulating. Charge-ordering in Fe_3O_4 has been known for some time [20]. The transition from the charge-ordered to the disordered state in Fe_3O_4 at 120 K, identified by Verwey as early as 1939, is associated with a resistivity anomaly.

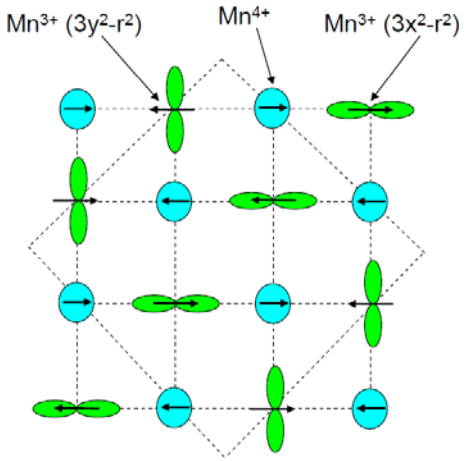

Fig. 1. 8: (a) Schematic diagram of spin, charge and orbital ordering in $La_{0.5}Ca_{0.5}MnO_3$.

Charge ordering has been found to occur in a few other transition metal oxides as well, but nowhere does it manifest itself as vividly as in rare earth manganites [21]. Accordingly, several of the rare earth manganites of the general composition $Ln_{1-x}AE_xMnO_3$ (*Ln* = rare earth, *AE* = alkaline earth) exhibit fascinating properties and phenomena associated with charge ordering. The occurrence of charge ordering in these manganites was first studied by Wollan and Koehler [22] and later examined by Jirak *et al.* [23]. The situation has since changed significantly due to the discovery of colossal magnetoresistance and other interesting properties in these materials [1]. For instance, in $La_{1-x}Ca_xMnO_3$, at x=0.5, a stable charge-ordered AFM state is found below T_C = 160 K (the schematic is shown in Fig. 1. 8). This charge ordered state can be explained by an ingenious model proposed by Goodenough [19]: Mn^{3+} and Mn^{4+} are arranged like a checkerboard, exhibiting the charge ordered, spin-ordered and orbital ordered states altogether. Since Mn^{3+} sites have a Jahn-Teller distortion, this periodic distribution of Mn ions reduces not only the Coulomb repulsive energy and exchange interaction energy, but also the Jahn-Teller distortion energy by the orbital ordering [24]. The first direct evidence for charge ordering was found in $La_{0.5}Ca_{0.5}MnO_3$ by Chen and Cheong

using electron microscopy [25]. Quasi-commensurate satellite reflections observed close to the onset of antiferromagnetism were interpreted as a result from the coherent ordering of $Mn^{3+}O_6$ and $Mn^{4+}O_6$ octahedra, as expected for a charge-ordered phase.

1. 2. 2 Phase separation (PS)

The phenomenon of charge/orbital ordering in manganites can coexist with ferromagnetic metallic phases, which makes it more attractive and surprising. The physics of solids with strongly correlated electrons appears to be dominated by states that are microscopically and intrinsically inhomogeneous in the most interesting range of temperatures and charge carrier (hole or electron) densities [26]. The most relevant examples are the cuprates at the hole- densities in the underdoped region and the manganites in the regime of colossal magnetoresistance (CMR). In cuprates the competition occurs between antiferromagnetic insulating and superconducting or metallic phases. On the other hand, in manganites the inhomogeneities arise from phase competition between ferromagnetic metallic and charge-ordered insulating phases. These microscopic and intrinsic inhomogeneities lead to phase separation (PS) in manganites [27]. Indeed, the existence of phase separation (PS) was envisioned by Nagaev [28] in an antiferromagnetic semiconductor, where the doping of electrons is expected to create a ferromagnetic phase embedded in an antiferromagnetic matrix. It was remarked that if the two phases have opposite charge, the coulomb forces would break the macroscopic clusters into microscopic ones, typically of nanometer scale size. Percolative transport has been considered to result from the coexistence of ferromagnetic metallic and insulating phases. PS is generally the result of a competition between charge localization and delocalization, the two situations being associated with contrasting electronic and magnetic properties. An interesting feature of PS is that it covers a wide range of length scales anywhere between 1 and 200 nm and is static or dynamic [27].

These intrinsically inhomogeneous states are more pronounced and universally accepted for manganites. These phase-separated states give rise to novel electronic and magnetic properties with colossal magnetoresistance (CMR) in doped perovskite manganites. CMR and related properties essentially arise from the double-exchange mechanism of

electron hopping between the Mn^{3+} and Mn^{4+} ions, which favors the ferromagnetic metallic phase below *T*c and the paramagnetic insulating state above *T*c. In the insulating state, the Jahn–Teller distortion associated with the Mn^{3+} ions localizes the electrons and favors charge ordering (CO) of Mn^{3+} and Mn^{4+} ions. This CO competes with double exchange and promotes the antiferromagnetic insulating (AFI) behavior [29]. Even in many of the manganites (exhibiting CMR) which are in FMM state at low temperatures, CO clusters occur. Thus in doped rare earth manganites CO (AFM) and FM clusters or domains coexist, the sizes of which are affected by the carrier concentration or composition, average size of the A-site cations, temperature and other external factors such as magnetic and electric fields [1, 27]. Phases with different charge densities and transport properties coexist as carrier-rich FM clusters or domains along with carrier-poor antiferromagnetic (AFM) phase. Such an electronic phase separation gives rise to microscopic or mesoscopic inhomogeneous distribution of electrons, and results in rich phase diagrams that involve various types of magnetic structures.

A clear evidence of electronic phase separation has been observed in several rare earth manganites in the past few decades and the phenomenon has been investigated by a variety of techniques [27]. Wollan and Koehler [22] have reported the coexistence of ferromagnetic and A-type antiferromagnetic reflections in the pioneer neutron diffraction study of $La_{1-x}Ca_xMnO_3$. Uehera *et al*. have demonstrated sound evidences of coexistence of metallic and insulating phases in $La_{5/8-Y}\ Pr_Y\ Ca_{3/8}MnO3$ using transport, magnetic and electron microscopy techniques [30]. A large but metallic ($\partial\rho/\partial T > 0$) resistivity far below the actual ferromagnetic transition clearly suggests the failure of a homogeneous picture, since only a percolative state can produce such large but metallic resistivity. To further strengthen their results, they carried out transmission electron microscopy and found 500 nm coexisting domains of CO insulator and FM metallic phases for Pr = 0.375 at 20 K. Fath *et al*. have provided further remarkable evidence of coexistence of inhomogeneous clusters of metallic and insulating phases employing scanning tunneling spectroscopy (STS) [31]. The cluster size was found to be as large as a fraction of a micrometer and depends strongly on magnetic

field. Other researchers have also studied the mixed phase tendencies by STS, STM and low temperature MFM [27, 32].

1. 2. 3 Melting of charge ordering and related aspects

The ordering of charge carriers in manganites has been accompanied by an increase in sound velocity, change in lattice parameters and anomalies in heat capacity, magnetization, resistivity and the activation energy for conduction [1]. Charge/orbital ordering can readily be melted to the ferromagnetic metallic state by application of various impulses such as magnetic field, pressure, electric field, photon and electron irradiation [1, 33]. For instance, the magnetic field-induced melting of charge ordered state was reported by Kuwahara *et al.* (1995) in $Nd_{0.5}Sr_{0.5}MnO_3$ [34]. The transition induced by the magnetic field is highly hysteretic and accompanied by drop in resistivity by as much as four orders of magnitude at low temperatures. In $Pr_{1-x}Ca_xMnO_3$ series, a similar huge magnetoresistance is reported, which results from the magnetic field induced CO–FMM transition. Irradiation with visible light at small electric fields is also reported to delocalize the CO state, causing an insulator–metal transition [35, 36]. The light induced insulator–metal transition in $Pr_{0.7}Ca_{0.3}MnO_3$ appears to generate a localized conduction path, although the bulk of the sample is insulating. Fiebig *et al*. [36] have shown that, upon photo-excitation, the resistance shows a gigantic decrease from a GΩ value to a metallic one.

1. 3 Colossal electroresistance (CER)

1. 3. 1 Background

In addition to the well-known case of the magnetic field and light irradiation induced insulator–metal transition, an electric field can cause the local insulator–metal transition [37]. This phenomena was first demonstrated in $Pr_{0.7}Ca_{0.3}MnO_3$, wherein the resistivity for different voltages applied to the sample differed by several orders of magnitude at low temperatures. In addition, it has been reported that resistivity of the crystal changes by several orders of magnitude during a voltage sweep when the voltage exceeds a threshold value. This spectacular electric field induced change in the resistivity by a few orders of magnitude, aptly

termed as colossal electroresistance (CER), has triggered a lot of excitement and research in the scientific community. The changes in the character of the conductivity of doped manganites (DM) under the electric field is most pronounced in the $Pr_{1-x}Ca_xMnO_3$ system and has been attributed to the field induced melting of charge ordering, the schematic is shown in Fig. 1. 9. Such a phase change, enabled by electric stimuli, is of enormous significance in the light of possible application as non-volatile fast memory devices.

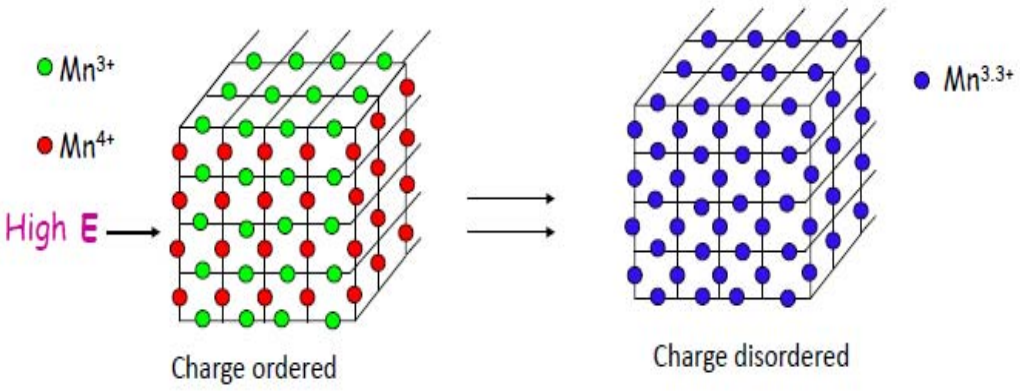

Fig. 1. 9: Schematic of the field induced melting of charge ordering.

Contemporary studies of electric field induced effects in thin films of several charge-ordered rare earth manganites including $Nd_{0.5}Ca_{0.5}MnO_3$ shows that very small dc currents (fields) destroy the CO state and give rise to insulator–metal transitions [1, 33, 38]. The current–voltage (*I-V*) characteristics are non-ohmic and show hysteresis. It was shown that the insulator–metal (I–M) transition temperature decreases with increasing current. The current induced I–M transition occurs even in $Y_{0.5}Ca_{0.5}MnO_3$, which is not affected by large magnetic fields [38]. Furthermore, there is no need for prior laser irradiation to observe the current induced I–M transitions. It is proposed that electric field causes depinning of the randomly pinned charge solid. There appears to be a threshold field in the CO regime beyond which non-linear conduction sets in along with a large broad-band conductivity noise. Threshold dependent conduction disappears around charge ordering temperature T_{CO} suggesting that the CO state is de-pinned at the onset of non-linear conduction. It has been also suggested that the

inhomogeneities or phase segregation present in these materials give rise to percolative conduction [38].

Gu *et al*. [39] theoretically considered the effect of electric field on a charge-ordered inclusion in a manganite medium subjected to phase separation. The electric field was assumed to concentrate at certain sites in the phase-separation medium. This field suppresses charge ordering, transforms the system from an antiferromagnetic into a ferromagnetic state, and stimulates the metal-insulator transition. It was suggested that the effects are a direct consequence of the Mott nature of strongly correlated electron systems (SCES), in which Coulomb interaction is suppressed by disordering, doping, and so on. When researchers study the electron transport in a medium subjected to phase separation (PS) under certain real conditions, they are dealing with the percolation transport of two resistor systems, namely, magnetically ordered (metallic) and charge-ordered (dielectric) systems, which form a complex structure in a film or single crystal. Thus, even a low electric field can significantly change the transport and magnetic properties of structures based on SCESs with PS.

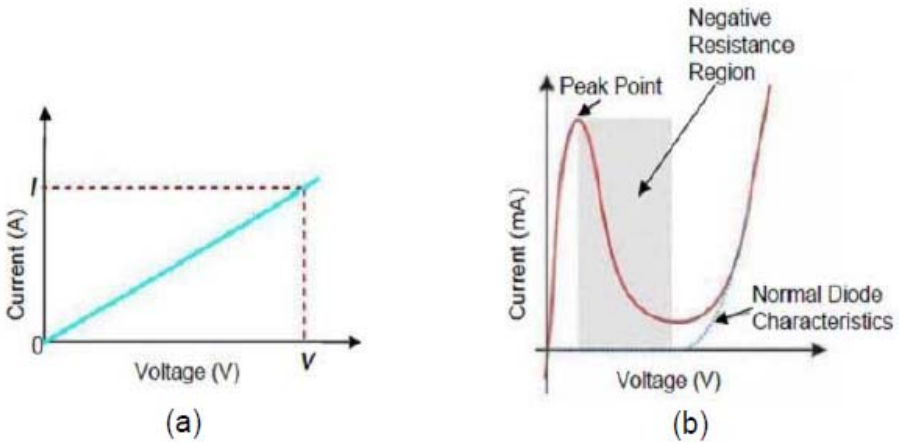

Fig. 1. 10: Comparison of the *I-V* curves of (a) ohmic resistor and (b) tunnel diode.

We compare the current-voltage (*I–V*) characteristics of a simple resistor with that of a tunnel diode in Fig. 1. 10. While the *I–V* curve of an ordinary resistor is linear, it shows a nonlinear behavior in diodes, tunnel diodes, Gunn diodes, avalanche diodes, etc. Interestingly, as discussed earlier, manganites also exhibit nonlinear conductivity, which finds application in electronic industry. As mentioned earlier, one of the first observations is the negative

differential resistance behavior (NDR) in charge-ordered $Pr_{0.67}Ca_{0.37}MnO_3$, wherein the voltage initially increases with current and then decreases above a threshold current [38]. This opens the possibility of these materials to be used in memory devices based on electric control of their resistance [40] and has generated a surge of interest in exploring nonlinear properties in other manganites.

1. 3. 2 Classification of electroresistance mechanisms

A radical change in the resistive properties of normal doped manganites under significant current injection conditions is observed and these effects were named differently in different works as (a) colossal electroresistance, (b) electric-field- and current-induced effects, (c) the reproducible effect of resistive switching for application in memory-containing devices, (d) electron instability effects (EIE), (e) field-induced resistive switching, (f) giant resistive switching, and the electric-pulse-induced resistive change reversible effect [41]. A huge variety of materials in a metal-insulator-metal (MIM) configuration have been reported to show hysteretic resistance switching [40]. In particular, colossal electroresistance (CER) memory phenomena found for many junctions between specific metal electrodes and correlated-electron oxides [42] has attracted enormous attention in the past few decades.

Different models were proposed to explain the aforementioned electroresistance effects:

(1) It is suggested that an electric field triggers the electrochemical migration of the oxygen defects and subsequently results in the switching behavior [43]. The resistive switching effect in a polycrystalline manganite was stimulated with spatially modulated oxygen vacancies.

(2) In heterojunctions, the interface is regarded as an oxygen-degraded interlayer. The redistribution of oxygen and oxygen vacancies in the near-boundary layer at a critical field is suggested to create a phase separation in the interface and thereby leading to a change in the resistive properties [44].

(3) In a similar investigation in a heterojunction based on LaSrMnO with a dielectric CeO_2 interlayer, the authors [45] envisioned the existence of electric domains in the dielectric CeO_2

interlayer that interact with oxygen vacancies. The movement of these vacancies under the electric field was attributed to the switching of the resistive states of the structure.

(4) The EIE were ascribed to the nature of the Mott transition at the normal metal-strongly correlated electron system (M-SCES) interface [46].

(5) Conceivable mechanisms for the resistive switching in MIM systems often consist of a combination of physical and/or chemical effects. However, they can be classified according to whether the dominant contribution comes from an electronic effect, a thermal effect, or an ionic effect. Caution must be exercised, because in many reports the switching mechanism has not yet been elucidated or suggestions are based on little experimental and theoretical evidence. Recently, resistive switching initiated by a voltage-induced partial dielectric breakdown and filamentary nature of the conductive path has been confirmed for NiO [47] and TiO_2 [48].

(6) Electronic charge injection and/or charge displacement effects are considered as another origin of resistive switching. For instance, a charge-trap model [49] has been proposed, in which charges are injected by Fowler–Nordheim tunneling at high electric fields and subsequently trapped at sites such as defects or metal nanoparticles in the insulator. This modification of the electrostatic barrier character of the MIM structure was ascribed to the changes in resistance. In another model, trapping at interface states is suggested to affect the adjacent Schottky barrier at various metal/semiconducting perovskite interfaces [50,51]. Another possible model is the insulator–metal transition (IMT), in which electronic charge injection acts like doping to induce an IMT in perovskite-type oxides such as (Pr,La)Ca MnO3 [37, 45] and SrTiO3:Cr [52].

(7) Finally, a model based on ferroelectricity has been proposed by Esaki [53] and theoretically described by few other researchers [54]. Here, an ultrathin ferroelectric insulator is assumed whose ferroelectric polarization direction influences the tunneling current through the insulator.

The origin of the CERM effect is under vital investigation, but a consensus has not yet been reached. The possibility of control of the chemical potential (doping level) of the

correlated insulator by an external bias field will open a new field for correlated-electron devices. The high sensitivity of the competing phases against the external field will be a key issue as well. Despite of the disagreement on the fundamental physical mechanisms, resistance switching of metal oxides has engendered recently strong interest in these materials for application in nonvolatile memories such as resistance random access memory (RRAM). One of the objectives of this research is to investigate CER in manganites.

1. 4 Giant magnetoimpedance (GMI)

When a soft ferromagnetic conductor carrying a small alternating current (ac) is subjected to an external magnetic field, the ac complex impedance of the conductor shows a large change and this phenomenon is known as giant magnetoimpedance (GMI). In other words, it is the ac counterpart for dc magnetoresistance, and consists of a change in the complex electrical impedance [$Z(\omega,H) = R(\omega,H) + jX(\omega,H)$] under an external static magnetic field (H). The complex impedance consists of ac resistance (R) and reactance (X) components. Magnetoimpedance (MI) is defined as

$$\mathrm{MI} = \frac{Z(0) - Z(H_{dc})}{Z(H_{dc})},$$

where *Z(0)* and *Z(H)* refer to the absolute impedances at zero fields and the external dc magnetic field applied respectively.

The discovery of giant magnetoimpedance (GMI) in metal-based amorphous alloys [55, 56, 57] has opened a new gateway in the development of high-performance magnetic sensors. Magnetic sensors based upon the GMI effect possess ultra-high sensitivity and therefore offer several advantages over conventional magnetic sensors such as fluxgate sensors, Hall effect magnetic sensors, giant magnetoresistive (GMR) sensors, and superconducting quantum interference device (SQUID) gradiometers [57]. For instance, the field sensitivity of a typical GMI sensor can reach a remarkable value as high as 500%/Oe compared to a GMR sensor (~1%/Oe) [57]. Magnetic sensors finds application in nearly all

engineering and industrial sectors, such as high-density magnetic recording, navigation, military and security, target detection and tracking, antitheft systems, non-destructive testing, magnetic marking and labelling, geomagnetic measurements, measurements of magnetic fields onboard spacecraft and biomagnetic measurements in the human body [56, 57]. The low price and high flexibility of GMI sensors warrants their wide-ranging application to replace other competing sensors. However, in actual ferromagnetic materials, the maximum value of GMI effect experimentally obtained to date is much smaller than the theoretically predicted value [57]. Therefore, there has been much efforts, focused mainly on special thermal treatments and/or on the development of new materials for the improvement of GMI properties [58, 59, 60]. For this, a thorough understanding of the GMI phenomena and the properties of GMI materials is required. Nonetheless, GMI devices are achieving a development stage that is mature enough to enter in the relevant area of extremely sensitive magnetic field sensors, a comparison with other sensors is provided in Table 1. 1.

Sensor type	Head length	Detectable field (Oe)	Response speed	Power consumption
Hall	10–100 μm	$1–10^6$	1 MHz	10 mW
GMR	10–100 μm	$0.1–10^2$	1 MHz	10 mW
GMI	1–2 mm	$10^{-8}–10^2$	1–5 MHz	10 mW
Flux gate	10–20 mm	$10^{-6}–10^2$	5 kHz	1W

Table 1. 1: Comparison of different magnetic sensors

Besides application point of view, impedance study is opening a new branch of fundamental research combining the micromagnetics of soft magnets with classical electrodynamics. Generally, GMI effect occurs at high frequencies and can be explained by classical electrodynamics. Radiofrequency (RF) is not homogeneous over the cross section of a conductor and it tends to concentrate near the conductor's surface and is called the skin effect. The exponential decay of current density from the surface towards the interior of the conductor is described by the skin depth:

$$\delta = \sqrt{\frac{2\rho}{\omega\mu}} \quad .$$

It depends on the circular frequency of the rf current ω ,the resistivity ρ, and the permeability μ. In non-ferromagnetic metals, μ is independent of frequency and the applied magnetic field; its value is very close to the permeability of a vacuum μ_0. In ferromagnetic materials, however, the permeability depends on the frequency, the amplitude of the ac magnetic field, the magnitude and orientation of a bias dc magnetic field, mechanical strain, and temperature. Applying a longitudinal dc magnetic field along the sample reduces the permeability and increases the skin depth, thus effectively reducing the impedance of the wire.

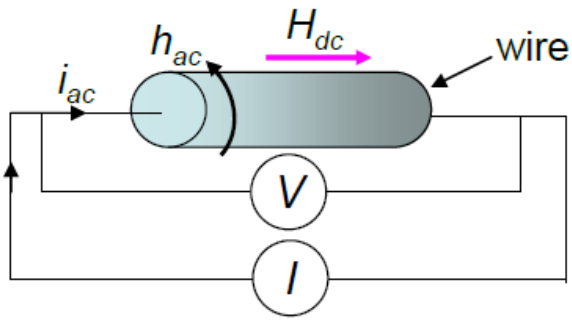

Fig. 1. 11: Schematic of the impedance circuit.

According to the definition of magnetoimpedance, the complex impedance of a magnetic conductor is given by the ratio V_{ac}/I_{ac}, where I_{ac} is the amplitude of a sinusoidal current $I = I_{ac}\exp(-j\omega t)$ passing through the conductor and V_{ac} is the voltage measured between the ends of the conductor. Fig. 1. 11 shows a schematic illustration of the impedance circuit. For a metallic ferromagnet with a length l and cross-sectional area A, assuming a linear approximation, its impedance can be expressed as follows:

$$\frac{Z}{R_{dc}} = \frac{lE_z(S)}{R_{dc}A\langle j_z\rangle_A} = \frac{j_z(S)}{\langle j_z\rangle_A},$$

where E_z and j_z are the longitudinal components of the electric field and current density respectively, R_{dc} is the dc electrical resistance, S denotes the value at the surface, and $< >_A$ is the average value over the cross section A. In ferromagnetic metals, where the displacement

currents can be neglected ($\dot{D} = 0$), and the material relations $E = \rho J$ and $B=\mu_0(H+M)$ hold, and using Maxwell's equations, the basic equation is obtained within the framework of classical electrodynamics of continuous media as

$$\Delta^2 H - \frac{\mu_0}{\rho}\dot{H} = \frac{\mu_0}{\rho}\dot{M} - grad(divM)$$

Separating the vectors H and M into their DC and AC components $H = H_0+h$, $M= M_0+m$ assuming $h, m \propto e^{i\omega t}$, the AC components are obtained as

$$\Delta^2 h - \frac{2i}{\delta_0^2} h = \frac{2i}{\delta_0^2} m - grad(divm),$$

where $\delta_0=\sqrt{(2\rho/\omega\mu_0)}$ is the nonmagnetic skin depth. A well known classical solution [61] for this equation for a cylindrical conductor with diameter 2a is

$$\frac{Z}{R_{dc}} = ka\frac{J_0(ka)}{2J_1(ka)},$$

where J_0 and J_1 are the Bessel functions of the first kind, and $k = (1 + i)/\delta_m$. In the later part of this thesis, how this solution involving the skin depth and permeability μ leads to a giant magnetoimpedance under an external magnetic field will be exemplified in detail. The observation of magnetoimpedance in soft metallic alloys and related research were received with much enthusiasm and it soon became clear that its interpretation requires a deep understanding of the micromagnetic characteristics of soft magnetic materials and its dependence on dynamic magnetism. However, the study of magnetoimpedance in manganites is rather scarce. Even though the dc magnetoresistance is studied in manganites extensively over the past few decades, the high frequency electrical transport has received less attention. Further, the practical application of dc magnetoresistance is hampered by the need of a high magnetic field to induce a resistivity change of > 10 % at room temperature [62]. In this research, we demonstrate magnetoimpedance studies as an alternative strategy to produce a low field ac magnetoresistance at room temperature in manganites. In addition, it is

demonstrated that impedance study can reveal additional features in manganites that cannot be observed in static measurements.

1. 5 Magnetocaloric effect (MCE)

Some magnetic materials become hot (cold) up on applying (removing) a magnetic field due to a large change in isothermal magnetic entropy or adiabatic temperature. This phenomenon is known as magnetocaloric effect (MCE). When the material is magnetized by the application of a magnetic field (H), the entropy associated with the magnetic degree of freedom, S_m, decreases. Under adiabatic conditions, the entropy change, ΔS_m, must be compensated for by an equal but opposite change in the entropy associated with the lattice, ΔS_l, resulting in a change in temperature of the material, ΔT, and leading to the magnetocaloric effect. The change in magnetic entropy [$\Delta S_M = \int_0^H \left(\frac{\partial M}{\partial T}\right)_H dH$, M is the magnetization] and hence MCE is expected to be maximum at the paramagnetic to ferromagnetic transition temperature (T_C). Majority of materials show second–order paramagnetic to ferromagnetic transition in which magnetic entropy change is moderate. An exception is metallic gadolinium that shows the largest magnetic entropy change (ΔS_m = 9.7 J/kg K for $\mu_0 H$ = 5 T at T_C = 293 K) in any elemental ferromagnets near room temperature due to its high moment (S = 7/2). Magnetic refrigeration based on MCE is highly eco-friendly and more energy efficient compared to the conventional vapor compression based refrigeration. It can be exploited for cryogenic cooling in aerospace and military applications and air-conditioner technology. A large temperature change observed in a Gd based alloy has triggered a frantic research and extensive efforts are underway in different laboratories to enhance the MCE by adopting optimal and alternative methods [63].A comprehensive summary of the MCE in manganites can be found in a recent review by Phan and Yu [64]. Besides a few other metallic alloys, manganese based oxides (manganites) are considered to be promising candidates for magnetic refrigeration due to low cost of synthesis, chemical

stability, and high magnetic entropy change over a wide range of temperature, thus noteworthy in the context of low-temperature refrigeration such as hydrogen liquefaction down to ~20 K. Other advantages of manganites are: 1. They can be easily prepared by the standard solid state or soft chemistry routes compared to expensive rare earth or inter-metallic based alloys 2. The T_C can be tuned anywhere between 100 K and 400 K by controlling the hole-doping (x) or the average ionic radii ($<r_A>$) of the *A* site cations 3. These materials exhibit either a second-order or a first-order paramagnetic to ferromagnetic transition depending on x and $<r_A>$ [65] and some compositions exhibit structural transition in the vicinity of ferromagnetic transition that could influence the MCE because of unusual strong coupling between lattice and magnetic degrees of freedom [66, 67] 4. Besides a second- order paramagnetic to ferromagnetic transitions at high temperature, Sr-based compounds with x = 0.5 such as $Pr_{0.5}Sr_{0.5}MnO_3$ show first-order lattice-coupled ferromagnetic to antiferromagnetic transition at low temperature. Application of a high external magnetic field not only transforms the antiferromagnetic phase into a ferromagnetic phase but also changes structural symmetry and volume which can lead to enhanced magnetic entropy ΔS_m, as shown for $Pr_{0.46}Sr_{0.54}MnO_3$ [68].

1. 6 Scope and Objective of the Present Work

A survey on the reported research papers showed that the mechanism behind the current induced effect on resistivity, particularly on the insulator-metal transition and nonlinear characteristics in manganites is not clearly understood yet. Many other effects like magnetoimpedance and magnetocaloric effects are less investigated in manganites. In this work, investigation of colossal electroresistance, magnetoimpedance and magnetocaloric effects in selected manganites are presented. The focus of our work is to understand the basic mechanism behind electroresistance properties in manganites, enhance the low field magnetoresistive properties at room temperature and investigate magnetocaloric effects in selected manganites. The main objectives of this thesis are as follows,

- To investigate different characteristics of colossal electroresistance effect in $Nd_{0.5}Ca_{0.5}Mn_{1-x}Ni_xO_3$ (x=0.0, 0.05, 0.07) manganite series.
- Investigation on the mechanism of CER in the above manganites which show prominent electroresistance behavior.
- To study the current induced effect on resistivity in $Sm_{1-x}Sr_xMnO_3$ (x=0.4,0.5) manganite series.
- Investigation of magnetocaloric effect in $Sm_{1-x}Sr_xMnO_3$ (x=0.3-0.5) manganite series.
- To develop alternative experimental strategies to enhance the low field magnetoresistive properties in a well known canonical double exchange manganite, $La_{0.7}Sr_{0.3}MnO_3$ at room temperature.
- To study the effect of measurement geometry on the magnetoimpedance properties in manganites.

1. 7 Organization of the Thesis

The rest of this thesis is organized as follows. In chapter 3, the study of electroresistance in a series of manganites $Nd_{0.5}Ca_{0.5}Mn_{1-x}Ni_xO_3$ is detailed. Chapter 4 describes the study of current induced magnetoresistance avalanches in $Nd_{0.5}Ca_{0.5}Mn_{1-x}Ni_xO_3$. Chapter 5 discusses the magnetotransport and magnetocaloric effects in $Sm_{1-x}Sr_xMnO_3$. In chapter 6, the current induced effects on resistivity in $Sm_{1-x}Sr_xMnO_3$ as a function of temperature and nonlinear transport are discussed in detail. In chapter 7, low field magnetoimpedance in a canonical double exchange manganite, $La_{0.7}Sr_{0.3}MnO_3$ is described. This study highlights an alternative strategy to produce a low field magnetoresistance and reveals an unusual field dependence of magnetoimpedance. Chapter 8 provides the summary of main results described in this thesis and their applications with an outlook of future research and development in this field.

Chapter 2

Experimental Methods

In the present study, electroresistance, magnetoimpedance and magnetocaloric properties were investigated in manganites which were synthesized mainly by standard solid state route. Various commercially available instruments and indigenously developed setups were used in the experiments.

2. 1 Synthesis methods

The common methods of synthesis of oxide materials are the ceramic (also known as solid state method and high-temperature method), solgel, combustion, co-precipitation, etc [69]. Except the first one, all the other methods belong to the class of soft-chemical routes of synthesis. In the present study, standard solid state method has been mainly utilized. The sample purity is very important, and hence the starting chemicals used for the synthesis in the present study were of the purity at 99.9 %. A furnace with controlled heating and cooling arrangements was used for heating the samples from 323 K to 1473 K (Carbolite, U.S.A) and the samples were heated in high purity alumina crucibles or boats.

2. 1. 1 Ceramic Method

Ceramic method involves the heating of mixed starting solid chemicals at high temperatures so that the ionic diffusion results in the formation of a stable compound. The solid state ionic diffusion requires high thermal energy and is generally a slow process. Hence, high temperatures and longer heating durations are required for the movement of ions and reorganization of the structures. In a typical ceramic method, the components in the form of metal oxides, carbonates, or other easily decomposable salts of organic acids, etc., were taken in the required stoichiometric proportions. The weighed components were mixed thoroughly in an agate mortar using a pestle. The well-ground mixtures were then initially heated at 1273 K and further at various temperatures with many intermediate grindings in order to ensure the sample homogeneity. All the samples were characterized for their phase purity, after each heating cycle, using powder X-ray diffraction method and accordingly, the

processing conditions were modified to obtain single phase materials. The same samples, of a particular composition, prepared under same sintering and grinding protocols showed reproducible electrical and magnetic transport properties.

2. 2 Characterization Methods

2. 2. 1 X-ray Diffraction

The powder X-ray diffraction (XRD) technique is used to identify which crystalline phases are present in a solid material [70]. Each crystalline material has its own characteristic powder X-ray diffraction pattern, which serves as a fingerprint for its identification. The powder X-ray method serves to indicate the completeness of a reaction and the presence/absence of unwanted side products and impurity phases.

In the present study, Philips X'PERT MPD (Cu-Kα (1.542 Å) radiation) powder X-ray diffractometer was employed for the structural characterization of the polycrystalline samples. For the usual phase analysis, a scan rate of 4º/minute was used and slow-scan measurements were done at a scan rate of 0.25º/minute, to identify the presence of small amounts of impurity phases. The least-squares method was used to fit the powder diffraction data in order to calculate the unit cell parameters. The computer programs used for the powder XRD analysis was PowderCell 2.3 (Kraus, W. and Nolze, G., downloaded from web www.ccp14.ac.uk).

2. 2. 2 Magnetotransport measurements

The low temperature measurements of the samples in different magnetic fields in this work were conducted in a Physical Property Measurement System (PPMS) supplied by Quantum Design Inc. (USA) which precisely controls the temperature and magnetic fields. The PPMS system used in this work can vary the temperature from ~4K to 400K and has a superconductor electromagnet which can generate different magnetic fields, up to 7 T.

A Quantum Design Vibrating Sample Magnetometer (VSM), attached to the PPMS was used for the magnetic characterization of the sample, which is a fast and sensitive DC

magnetometer. The basic measurement is accomplished by oscillating the sample near a detection (pickup) coil and synchronously detecting the voltage induced. By using a compact gradiometer pickup coil configuration, relatively large oscillation amplitude (1-3 mm peak) and a frequency of 40 Hz, the system is able to resolve magnetization changes of less than $10e^{-6}$ emu at a data rate of 1 Hz. The VSM module consists primarily of a VSM linear motor transport (head) for vibrating the sample, a coil set puck for detection, electronics for driving the linear motor transport and detecting the response from the pickup coils, and a copy of the MultiVu software application for automation and control.

Fig. 2. 1: Photograph of the Vibrating Sample Magnetometer (VSM) module attached to Physical Property Measurement System (PPMS)

2. 2. 3 Colossal electroresistance measurements

The four probe *dc* and pulsed *I-V* characteristics of bar shaped polycrystalline samples were measured using source-measure units (Keithley 2400 and Yokagawa GS610) interfaced to the PPMS. In the four-probe method, separate pairs of wires are used for providing the current through the sample and measuring the voltage across it. The advantage of such a four-wire method over the conventional two-wire method is that the contact resistance due to electrical contacts with the material and the wire resistance can be avoided. Another effect that may arise during the resistance measurement is due to the dissimilar metal contact, which results in a thermal voltage. This can be nullified by changing the direction of

the current. The PPMS system used in this work can vary the temperature from ~4K to 400K and has a superconductor electromagnet, which can generate magnetic fields up to 7 T. The electrical contacts were made with Ag-In alloy or Ag paste and the results were found to be identical. The sample was glued to a thin mica substrate with GE-7031 varnish which was anchored to the standard PPMS brass sample puck.

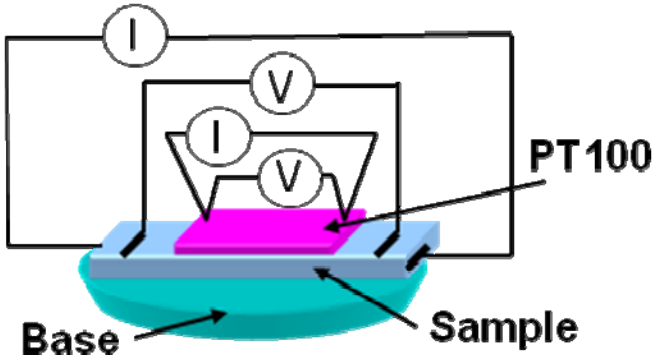

Fig. 2. 2: Schematic of the colossal electroresistance (CER) measurement set up. The PT100 thermometer is attached on to the top surface of the sample and measures the "surface temperature T_S". The cernox sensor situated beneath the sample measures the "base temperature T", recorded by the cryostat.

To monitor the temperature of the sample (T_S) in the electroresistance measurements, a Pt-thermometer (PT100) of size 3x2x1.2 mm^3 was glued to the top surface of the sample with a good thermal conductive grease (Apiezon-N grease) and a small quantity of GE-7031 varnish. The Pt resistor was positioned between two voltage probes. The four probe resistance of the Pt thermometer was monitored by measuring the voltage across the Pt-resistor using a Keithley 2182A nanovoltmeter while supplying a constant current of 10 μA with Keithley 6221 dc and ac current source. The cernox sensor attached to the sample puck measured the base temperature and is recorded by PPMS, which is denoted by T in the thesis, unless otherwise stated. It is to be pointed out that the base temperature recorded by the PPMS did not show any variation (remains at the stable value of 300 K) with current/voltage sweep and this leads to the general misconception of a trivial role played by joule heating in the sample. On the contrary, since the top surface of the sample is in very good thermal contact with the PT100 thermometer in our experimental set up, we could measure a significant change in the

temperature of the sample during the current/voltage sweeps. Although a small temperature difference between thermometer and the sample is possible, the difference will be one tenth of kelvin and hence negligible.

All the pulsed measurements were performed using a Yokogawa GS610 source-measure unit. The details about the pulse parameters and the protocols adopted are discussed with the experimental results in the following chapters. All the instruments were interfaced to a computer via GPIB, auto-controlled and readings recorded automatically by self-written programs, using National Instruments LabView 8.2 software.

2. 2. 4 Magnetoimpedance measurements

We have measured the four probe *ac* impedance $(Z(\omega,H) = R(\omega,H) + jX(\omega,H))$ of polycrystalline rectangular bar samples with an Agilent 4285A LCR meter for frequency range (f = 75 kHz to 30 MHz) with 3 mA *ac* excitation current. For room temperature measurements, an electromagnet provided a variable *dc* magnetic field ($\mu_0 H$) from -100 mT to +100 mT and the field was applied parallel to the long axis of the sample, i.e., along the direction of the *ac* current. The temperature dependence of impedance in the samples was studied using an external multifunctional probe connected to the PPMS, which had BNC adapters that could be connected to the LCR meter.

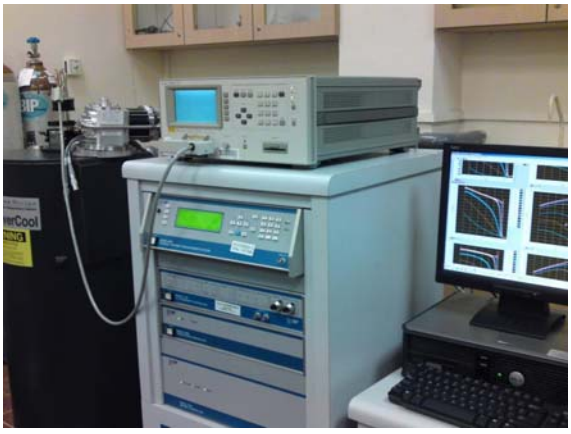

Fig. 2. 3: Photograph of the impedance measurement setup.

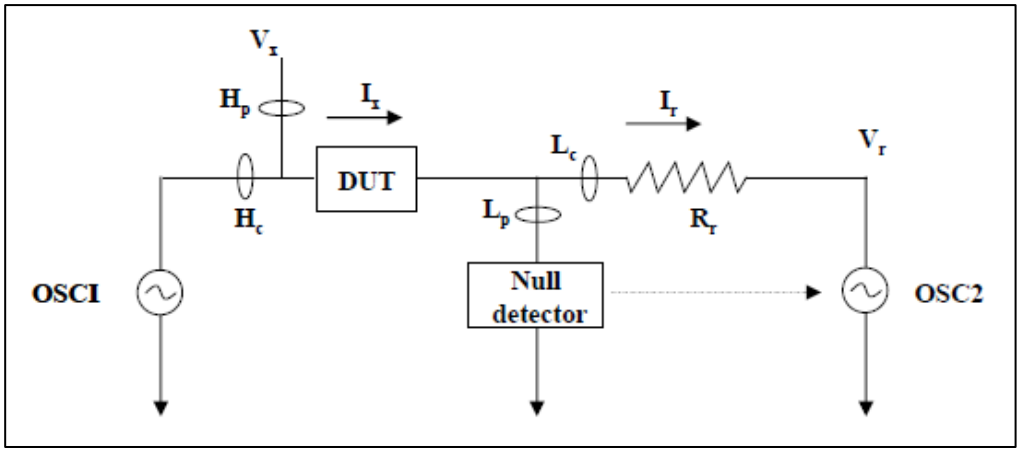

Fig. 2. 4: Operation image of the auto-balancing bridge.

To measure impedance of device under test (DUT), the 4285A LCR meter employs the auto balancing bridge method [71], which can cover frequencies from 100 kHz to 30 MHz. The schematic of the operation of the auto-balancing bridge is shown in Fig. 2. 4. For frequencies below 100 kHz, an I-V converter operational amplifier acts as a null detector and maintains the potential at Low point L to be zero (Virtual ground). The current I_x balances with the current I_r which flows through the range resistor R. Due to the performance limit of op-Amps at high frequencies, it is replaced by a sophisticated null detector, a phase detector, an integrator and a modulator. Making use of the known resistance value R, the impedance Z is computed from the voltages across the DUT (V_x) and the range resistor (V_r) in the following manner:

$$Z = \frac{V_x}{V_r} R$$

For the Agilent LCR meter, a standard Agilent 16048D test fixture with the cable length compensation was used for the impedance measurements in the samples. Open/short correction was performed to eliminate the measurement errors due to stray parasitic impedance in the test fixture and in order to improve the measurement accuracy, load correction was performed by using a calibrated device as a reference.

2. 2. 5 Magnetocaloric measurements

In the magnetocaloric measurements, we study the change in the magnetic entropy, ΔS_M, as a function of temperature. The magnetization of the sample as a function of magnetic field at close temperature intervals are performed using the Vibrating sample magnetometer. From the magnetization isotherms (*M-H*) measured at discrete temperatures, ΔS_m, can be approximated as $\Delta S_M = \frac{1}{\Delta T}\left[\int_0^H M(T+\Delta T, H)\,dH - \int_0^H M(T,H)\,dH\right]$. In order to evaluate the magnetic entropy from our isothermal *M-H* curves, a numerical approximation to the above integral has to be taken. The method is to use the isothermal magnetization measurements at small discrete field intervals, $\left|\Delta S_m\right| = \sum_i \frac{M_i - M_{i+1}}{T_{i+1} - T_i}\Delta H_i$ where, M_i and M_{i+1} are the experimental values of the magnetization at temperatures, T_i and T_{i+1}, respectively, under an applied magnetic field H_i. Using the above equation, the entropy change associated with the magnetic field variation can be calculated from the *M-H* curve at various fixed temperatures.

Chapter 3

Colossal electroresistance in $Nd_{0.5}Ca_{0.5}Mn_{1-x}Ni_xO_3$ (x = 0, 0.05, 0.07)

3. 1 Introduction

Although perovskite manganese oxides (manganites) shot into fame because of the discovery of colossal negative magnetoresistance in them in early 90's [3], it is now clear that the resistivity of these materials is sensitive not only to the external magnetic field but to other external stimuli such as pressure, X-ray radiation, and electric field [33]. In particular, the current or electric field-induced collapse of the insulating charge ordered (CO) state into the conducting ferromagnetic metallic (FM) state has been extensively investigated since its first discovery in $Pr_{0.7}Ca_{0.3}MnO_3$ [37]. It was reported that a large voltage ($V \sim 700$ V) could switch the insulating charge ordered state to a metallic ferromagnetic state due to the subtle competition between the CO and FM, and consequently, caused a huge decrease in resistance. Since the resistivity ratio $\rho(0)/\rho(V)$ was several orders of magnitude (10^2-10^8 for the voltage amplitude 100-700 V), the effect was aptly called colossal electroresistance (CER). Later, Guha *et al*. [38] found a strong non-linear voltage-current characteristic at lower current regimes ($I < 20$ mA) and negative differential resistance behavior, which generated a lot of interest in the non linear electrical transport in manganites.

While many issues pertaining to the existence of CER in these oxides have been reported, its science has many puzzles and challenges. At present, there is no consensus about the unique origin of the electroresistance. The electroresistance observed in $Pr_{0.7}Ca_{0.3}MnO_3$ was initially attributed to electric-field induced melting of charge ordering similar to the effect of magnetic field [37]. Subsequent research efforts led to various other explanations such as modification of Schottky barrier height at the interface [72], trap controlled space-charge limited current [73], excitation of charge density waves [74], small-polaron-hopping [75], phonon-assisted electron delocalization [76], formation of conductive filamentary paths

[38], Mott transition at the interface [45], creation of defects and migration of oxygen ions [43]. It might be possible that different mechanisms are operative in these systems which possess a wide range of electronic ground states, however a coherent picture is yet to emerge. Though a few researchers [77, 78] suggested that self Joule heating is important and could lead to a current induced electroresistance in manganites, majority of researchers ignore its relevance. The currents necessary for nonlinear effects are always on the limit of Joule heating and in this regard, distinguishing intrinsic mechanisms of the CER effect from those originating from thermal effects remains challenging and intriguing. Hence there is an urgent need to identify various key factors that influence CER in manganites.

In this chapter, we emphasize on the *dc* and pulsed current induced electroresistance in $Nd_{0.5}Ca_{0.5}Mn_{1-x}Ni_xO_3$ (x= 0, 0.05, 0.07). We present results on the temperature dependence of the resistivity under various current amplitudes and voltage-current (*V-I*) characteristics at different temperatures for the parent compound (x= 0), 5% (x=0.05) and 7 % (x= 0.07) Ni doped samples. The un-doped and doped compounds, which are of different electronic and magnetic ground states show distinct electroresistance behavior. The simultaneous measurements of electroresistance behavior and surface temperature of the sample reveal that the current induced electroresistance and strong nonlinear characteristics observed in these manganites at higher current density are caused by Joule heating. The effect of various external magnetic fields and pulsed current on the non linear *V-I* characteristics is also discussed. We show that the resistance can be reversibly switched between high and low resistance states by controlling the pulse width of the voltage excitation even if the current amplitude is fixed in the current regime of negligible Joule heating. Plausible mechanisms have been suggested for the observed effects.

3. 2 Experimental Section

Polycrystalline samples of $Nd_{0.5}Ca_{0.5}Mn_{1-x}Ni_xO_3$ (x= 0, 0.05, 0.07) were prepared by standard solid state route and characterized by XRD and magnetic measurements. The temperature dependence of the resistivity (ρ) and the *dc* and pulsed *V–I* characteristics were

performed on polycrystalline samples of rectangular shape of dimensions 8x3x3 mm^3. The description of experimental set-up used for the CER measurements are provided in chapter 2. The PT100 thermometer attached to the top surface of the sample measured the surface temperature of the sample (T_S) during the electroresistance measurements. Unless otherwise stated, T refers to the base temperature recorded by the cryostat, which is measured by a cernox sensor attached beneath the sample puck.

3. 3 Results and Discussion

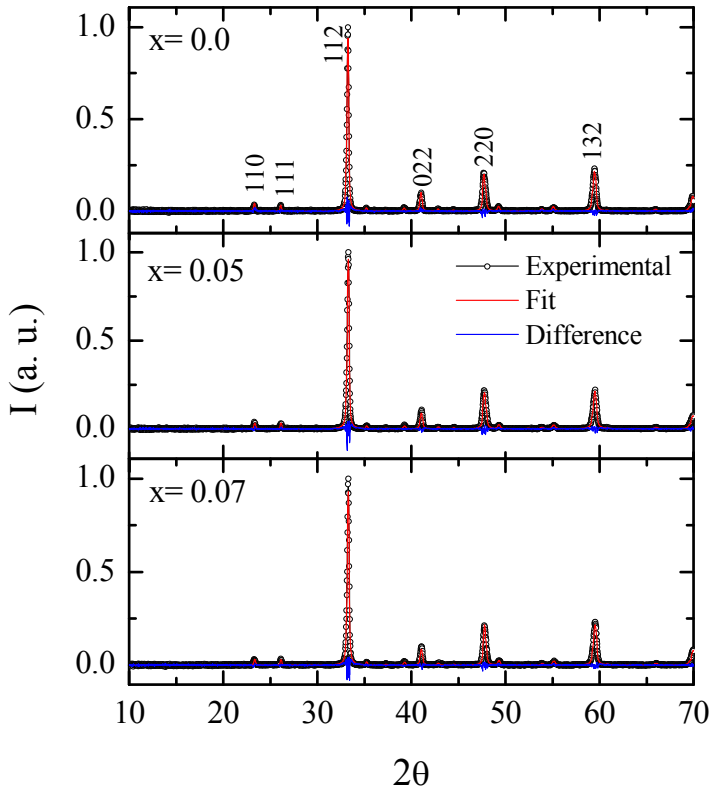

Fig. 3. 1: XRD pattern of $Nd_{0.5}Ca_{0.5}Mn_{1-x}Ni_xO_3$ (x = 0, 0.05 and 0.07) samples.

The XRD pattern of the $Nd_{0.5}Ca_{0.5}Mn_{1-x}Ni_xO_3$ (x= 0, 0.05, 0.07) compounds is shown in Fig. 3. 1. The samples are found to be of pure phase, and the peaks are indexed to orthorhombic Pbnm structure in accordance with Ref. [79], whose lattice parameters are nearly independent of the Ni content. We show the magnetization (M) versus temperature (T) curve for the parent compound $Nd_{0.5}Ca_{0.5}MnO_3$ (NCMO) in Fig. 3. 2. A peak occurs in the M-

T curve around the charge ordering temperature T_{CO}= 245 K, which is due to the structural transition caused by the e_g orbital and charge ordering. The NCMO sample undergoes antiferromagnetic transition around 160 K [80]. A weak anomaly due to antiferromagnetic ordering is seen in *M*-*T* curve around 160 K while cooling, however, the anomaly is masked in the hysteresis behavior while warming. The hysteresis is due to the strain developed, which is related to the e_g orbital ordering and disordering while cooling and warming, respectively. The $\rho(T)$ of the sample shows a semiconducting behavior ($d\rho/dT < 0$) in the temperature range, T = 300 to 75 K, but a clear increase in $\rho(T)$ occurs around T_{CO}, as evident in the inset of Fig. 3. 2.

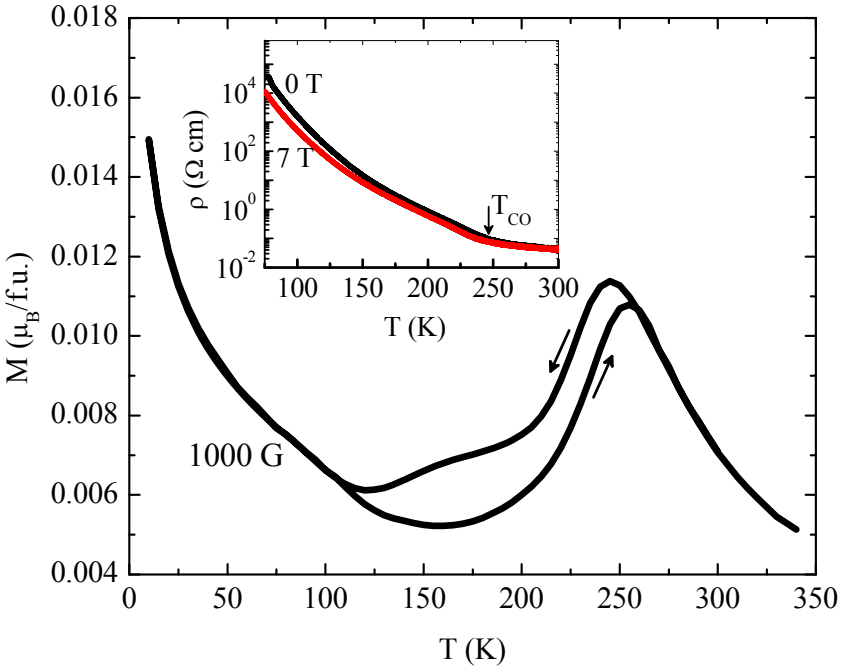

Fig. 3. 2: Temperature (*T*) dependence of Magnetization (*M*) of NCMO sample. The inset shows the $\rho(T)$ under $\mu_0 H$ = 0 and 7 T.

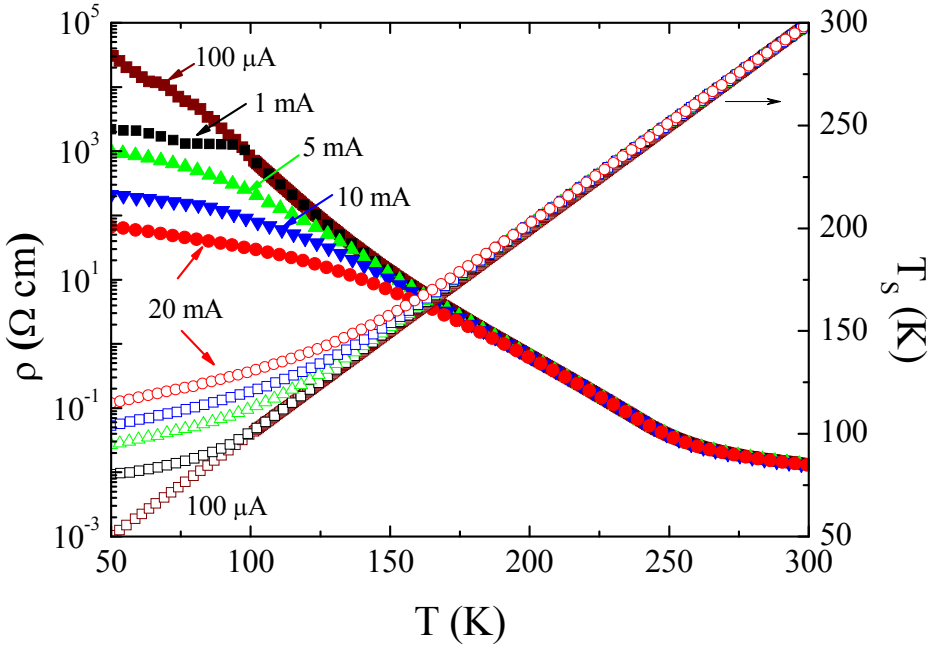

Fig. 3. 3: Temperature dependence of the resistivity of NCMO for *dc* current values *I* = 100 µA, 1, 5, 10 and 20 mA. The *x*-axis shows the base temperature (*T*) of the sample measured by the cernox sensor installed in the cryostat beneath the sample holder. The *y*-axis on the right scale shows the temperature (T_S) measured by the Pt-sensor glued on the top surface of the sample.

Fig. 3. 3 shows the temperature (*T*) dependence of resistivity (ρ) of the NCMO sample for different *dc* current strengths, *I* = 100 µA, 1, 5, 10 and 20 mA on the left scale. The x-axis shows the temperature (*T*) of the sample recorded by the PPMS which we call as the "base temperature" and the right scale shows "surface temperature" of the sample (T_S) measured by the platinum resistance sensor attached to the top surface of the sample. While the resistivity versus temperature curves for all current values matches above 160 K, they clearly bifurcate below 160 K. The $\rho(T)$ curves for all current values increases with decrease in temperature. However, the values of resistivity for different current strengths show a significant difference at low temperatures. Remarkably, ρ decreases as much as 99 % at 50 K as the current increases from 100 µA to 20 mA. This current-induced electroresistance is accompanied by a large increase in the surface temperature of the sample. The difference between the surface temperature of the sample and base temperature increases with increasing current and decreasing temperature. When the base temperature of the sample measured by

the cryostat is 50 K, the surface temperature of the sample is as high as 120 K for 20 mA, shown on the right scale, thus suggesting a significant Joule heating of the sample at low temperatures and high current strengths. Since the sample is semiconducting, Joule heating can contribute to the lowering of resistance in addition to the non-thermal mechanisms. This type of current–induced electroresistance was reported earlier in $Nd_{1-x}Ca_xMnO_3$ (x = 0.3, 0.5) but possible Joule heating was not considered by the authors [81].

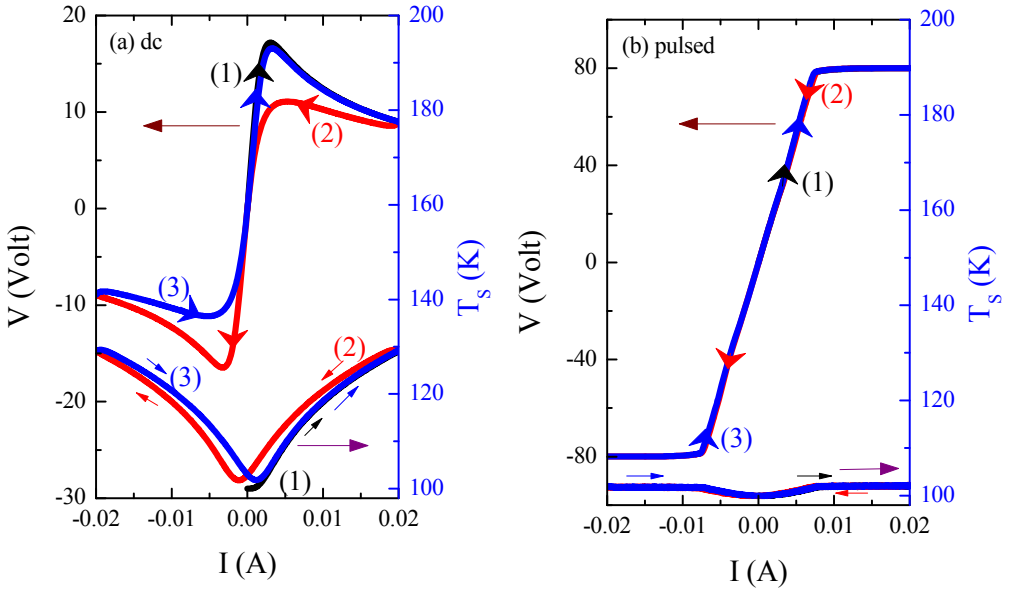

Fig. 3. 4: Voltage versus current (*V-I*) characteristics (left scale) of NCMO at *T* = 100 K in the (a) dc and (b) pulsed current mode. The right scale shows the corresponding behavior of T_S.

Fig. 3. 4(a) and Fig. 3. 4(b), on the left scale, shows the Voltage (*V*) versus current (*I*) behavior of the NCMO sample at *T*= 100 K while sweeping the current in both *dc* and pulsed current modes, respectively. For pulsed current sweep, we used pulses of a long period (P_D = 1 s) and short pulse width (P_W = 25 ms), increasing the amplitude of the pulse current in step of 0.02 mA. The response of the surface temperature of the sample (T_S) during the *dc* and pulsed current sweep is shown on the respective right scale. A complete *V-I* cycle consists of three consecutive current sweeps: (1) virgin (*I* = 0→20 mA), (2) downward (*I* = 20→–20 mA), and (3) upward (*I* = –20→20 mA) sweeps. The sample shows a strong nonlinear and hysteresis behavior in the complete dc current cycle [Fig. 3. 4(a)]. In the dc mode, the voltage initially increases with increasing current in the virgin sweep (1), exhibits a peak in voltage at

I = +3.2 mA and then decreases with further increase in the current, thus leading to the well known negative differential resistance behavior (NDR) [38]. In the down-ward current sweep (2), a peak in voltage occurs at I = 2.9 mA in the first quadrant and at I = -3.1 mA in third quadrant. The upward current sweep (3) reproduces the behavior of the downward current sweep (2), with peaks in voltage occurring around I = -2.9 mA and +3.1 mA. While the dc *V-I* curve is strongly nonlinear, the pulsed *V-I* curve [Fig. 3. 4(b)] is almost linear up to a certain current, above which the voltage shows an apparent saturation because the voltage exceeds the compliance limit. Note that the voltage developed in the pulsed mode is higher than in the dc mode. The surface temperature of the sample (T_S) shows a large increase with increase in current in both the directions in the dc current sweep mode [Fig. 3. 4(a), right scale]. However, T_S in the pulsed mode [Fig. 3. 4(b), right scale] shows a negligible increase compared to the *dc* mode. In the dc current sweep, the sample voltage initially increases linearly with current. Above a threshold current, the sample temperature significantly increases and results in the decrease of the voltage/resistance because of the semiconducting behavior ($d\rho/dT < 0$). Since the increase in the temperature of the sample is negligible in the pulsed mode, the nonlinear behavior is absent, and hence V is also high (ρ is high). The Joule-heating assisted enhancement in the *dc* electroresistance was also reported in metallic $La_{0.8}Ca_{0.2}MnO_3$ film and also in the phase separated Cr- doped $Nd_{0.5}Ca_{0.5}MnO_3$ though the effect of pulsed current was not investigated in those studies [77]. Tokunaga *et al*. [78] observed much sharper *dc* voltage jump at a threshold *dc* current in the phase separated manganite La-Pr-$CaMnO_3$ and attributed it to the local Joule heating effect. Interestingly, an anomalous behavior of oscillation in the current was also found if the voltage was maintained at a constant value and this was attributed to the closing and opening of metallic conducting channels.

The striking differences between the *dc* and pulsed *V-I* characteristics (Fig. 3. 4) motivated us to investigate the response of electrical resistivity of the NCMO sample to a sequence of pulse trains with varying pulse period (P_D) but with fixed current amplitude. We

have chosen, I = 2 mA to avoid excessive Joule heating. Fig. 3. 5(a) shows the change in ρ (left scale) and T_S (right scale) in response to pulse trains of 2 mA amplitude with a fixed pulse width (P_W = 25 ms) but two different pulse periods. Each pulse train consists of 400 pulses and the consecutive pulse trains differ in pulse period (P_D = 100 and 50 ms). The start of a pulse train is marked by arrows in the figure. After the initial drop of resistance at the beginning of the pulse train, the resistance abruptly jumps up by 37 % when the P_D is changed from 50 ms to 100 ms and remains nearly unchanged until the next pulse train of a shorter pulse period (P_D = 50 ms) sets it to a low resistance state. The resistance can be set to a higher value again by the application of the longer pulse period (P_D = 100 ms). In accordance with the resistivity switching, temperature of the sample (Fig. 3. 5(a), right scale) also changes periodically though only by ~ 1 K. We have calculated the change in ρ as T increases from 100 K to 101 K from ρ(T) curve (Fig. 3. 2) and it turns out that ρ decreases by about 18 % which is smaller than found with the pulse period–induced switching. This suggests that electroresistance can occur partially due to the Joule heating but other non-thermal mechanisms may also play a significant role. Materials that show switching between high ("OFF") and low ("ON") resistance states upon the change in current/voltage amplitude are currently attracting attention due to their potential applications as resistive random access memory (ReRAM) elements in next generation nonvolatile memories (NVM) [82]. The electrical resistivity switching induced by pulsed voltage and current received more attraction following the initial report of polarity dependent resistance change in $Pr_{0.7}Ca_{0.3}MnO_3$ sandwiched between two metal electrodes, high resistance state for positive voltage pulses and low resistance for negative voltage pulses at room temperature [83]. The magnitude of electroresistance depends not only on the polarity but also on the amplitude and number of pulses. However, the influence of pulse width\period on the electroresistance effect has been studied in less detail. Odagawa *et al*. [73] found that the electroresistance is independent of pulse width from *dc* to 150 ns in $Pr_{0.7}Ca_{0.3}MnO_3$ film.

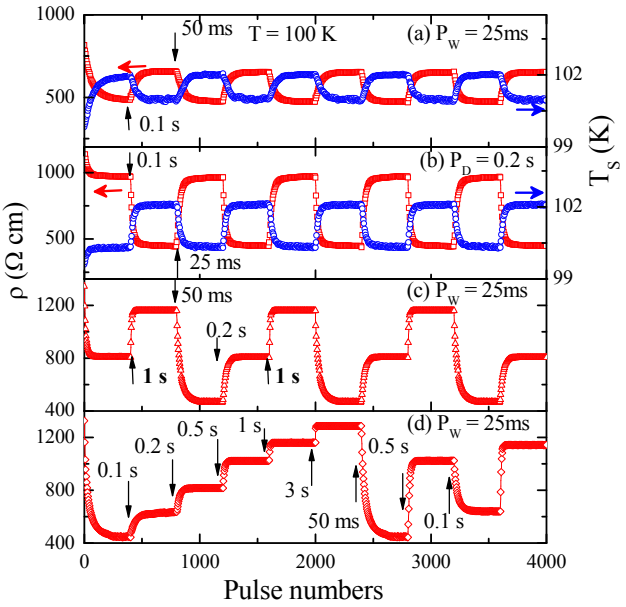

Fig. 3. 5 (a) Bi-level resistivity switching in NCMO at T = 100 K triggered by varying (a) Pulse period (b) Pulse width. (c) Tri-level and (d) random resistivity switching for varying pulse periods. The numbers indicate the varying quantity.

The sample also shows a resistive switching when the consecutive pulse trains consists of pulses with different pulse width (P_W), but with fixed pulse period (P_D= 200 ms), as shown in Fig. 3. 5(b). Here, the resistivity abruptly decreases by 53 % when P_W is changed from 25 ms to 100 ms. The observed resistivity switching with varying P_D or P_W may offer advantage in certain cases over the conventional method of resistance switching with varying magnitude of the current. We can also obtain resistivity switching between three levels by employing three different pulse periods as shown in Fig. 3. 5(c). It is observed that a pulse train of P_D = 1 s increases ρ by 44 %, another pulse train of P_D = 25 ms decreases ρ by 60 %, and a third pulse train of P_D = 0.2 s increases ρ by 70 % with respect to their previous resistivity states. The repetition of pulse sequences drives the sample to the respective resistive states and is completely reproducible. Fig. 3. 5(d) shows the effect of random switching of resistivity by different P_Ds for a fixed P_W = 25 ms. It is found that each P_D drives the system into a specific resistive state, whatsoever is the sequence. The resistivity of the sample changes from ~ 450 Ω cm to ~ 1286 Ω cm when the P_D of the pulse train is sequentially changed from 25 ms to 3 s with intermediate resistance states attained for P_D =

0.1, 0.2, 0.5, and 1 s. When the pulse period is changed randomly after 3s pulse train, the resistivity retrieve their respective states, as can be seen in Fig. 3. 5(d).

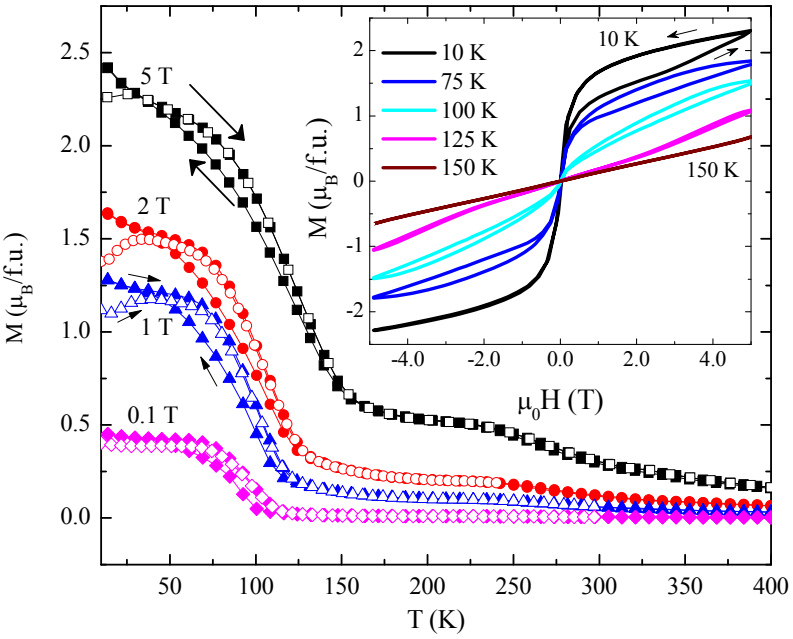

Fig. 3. 6: (a) Temperature (*T*) dependence of the magnetization (*M*) of NCMONi05 at $\mu_0 H$ = 0, 1, 2 and 5 T. Note that the field cooled (FC, closed symbols) curves bifurcate from the zero field cooled (ZFC, open symbols) curves at low temperatures under high magnetic fields. The inset shows the *M* vs. *H* curves at different temperatures.

Next, we discuss the magnetic behavior of 5 % Ni- doped NCMO sample at the Mn site, i.e., $Nd_{0.5}Ca_{0.5}Mn_{0.95}Ni_{0.05}O_3$ (NCMONi05). The main panel of Fig. 3. 6 shows the magnetization (*M*) versus temperature (*T*) curves of NCMONi05 at $\mu_0 H$ = 0.1, 1, 2 and 5 T measured while cooling and warming under field cooled (FC, closed symbols) and on warming after sample was zero field cooled (ZFC, open symbols). While cooling from 300 K, the sample undergoes a paramagnetic to ferromagnetic transition around the Curie temperature T_C = 85 K, as indicated by the inflection point in the derivative of the *M*-*T* curve for $\mu_0 H$ = 0.1 T. The T_C is shifted to a higher temperature (T_C = 115 K) at $\mu_0 H$ = 5 T. The ZFC *M*-*T* clearly bifurcates from the FC *M*-*T* below a particular low temperature T_g, and T_g shifts downward in temperature with increasing strength of the magnetic field. In the inset of Fig. 3. 6, we show the isothermal magnetization (*M*) versus field (*H*) curves at selected temperatures.

While the *M-H* curve shows a linear paramagnetic behavior at T = 150 K, the *M-H* curve at T = 10 K shows a ferromagnetic behavior. The *M-H* curve is linear at 150 K but shows an upturn above 4 T, which indicates a metamagnetic transition at higher fields. Although the low field magnetization shows a rapid increase for temperatures $T \leq$ 100 K, the *M-H* curves shows an open hysteresis loop while the field is swept from +5 T→ –5 T→+5 T. When T= 10 K, the open hysteresis is observed only in the first quadrant, i.e., for field sweep 0→+5 T→ –5 T. Further field sweep (0→ –5 T→+5 T) results in ferromagnetic behavior. These characteristics indicate phase separation in the compound, i.e., the long range ferromagnetic phases coexisting with the charge ordered phases. This is also evident in the $M(T)$ curve at $\mu_0 H$ = 5 T (see the hump around 240 K).

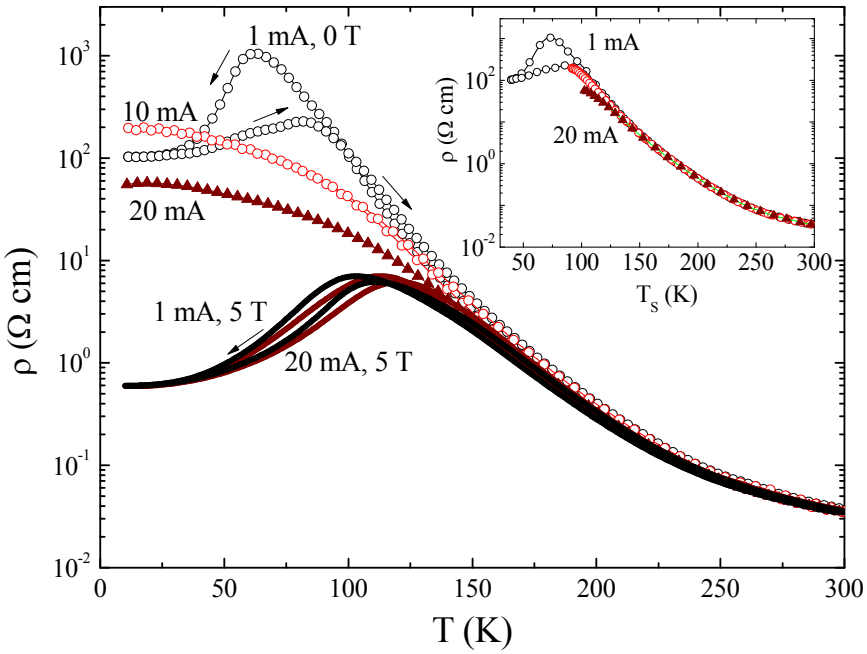

Fig. 3. 7: ρ-T curves for different current strengths in NCMONi05. The inset shows the ρ for different current strengths as a function of surface temperature T_S.

Now, let us see the electroresistance behavior in the 5 % Ni- doped sample. It is discussed earlier that the parent half doped compounds like $Ln_{0.5}Ca_{0.5}MnO_3$ (Ln= La, Nd, Pr etc.) are AFM insulators at low temperatures and shows an insulating behavior over the temperature 400-10 K. Interestingly, it has been reported that light chromium doping induces a metal to insulator transition in the otherwise insulating $Ln_{0.5}Ca_{0.5}MnO_3$ [84]. Trivalent Cr^{3+}

ion is isoelectronic to Mn^{4+} (t^3_{2g}) ion, its substitution reduces the number of Jahn-Teller active Mn^{3+} ions, leading to weakening of CO/OO state. Also Cr^{3+} suppresses C-IC (commensurate-incommensurate) structural transition, leading to short range of CO state with incommensurate charge ordering [85]. Further, it is suggested that an antiferromagnetic coupling exists between Cr^{3+} ion and its nearest neighbors [84]. The spins of Mn^{3+} and Mn^{4+} in the FM zigzag chain will be reversed while the spins in the nearest chains remain unchanged, since the coupling was already antiferromagnetic. The three chains will thus be ferromagnetically coupled around the Cr^{3+} ions, leading to the creation of an elliptic FM microregion around the Cr^{3+} ions in the CO phase. Light Ni doping also results in similar features. We show the temperature variation of the resistivity of the NCMONi05 sample at three different current amplitudes (I = 1 mA, 10 mA, and 20 mA) in the main panel of Fig. 3. 7. At a low current magnitude of 1 mA, the resistivity shows an insulator-metal transition around 60 K while cooling. The resistivity while warming is lower than while cooling in the temperature range from T = 30 K- 95 K and then it crosses over the cooling curve over a certain temperature range before merging again at higher temperatures T > 200 K. This insulator-metal transition is driven by the percolation of ferromagnetic clusters in the charge ordered insulating matrix similar to earlier observation in $Pr_{0.5}Ca_{0.5}Mn_{1-x}Cr_xO_3$ (x = 0.015-0.05) [86]. At higher current amplitudes $I \approx$ 10 mA and 20 mA, the resistivity above 150 K matches with I = 1 mA data but they differ below 150 K. The insulator-metal transition and hysteresis seen in the ρ-T curve at I = 1 mA disappear in the ρ-T curves at I = 10 mA and 20 mA. Although ρ for I = 20 mA is lower than the corresponding resistivity for I = 1 mA down to the lowest temperature from 150 K, the resistivity for I = 10 mA exceeds the resistivity at I = 1 mA below 50 K. Upon the application of a magnetic field $\mu_0 H$ = 5 T, the insulator-metal transition is recovered and it occurs around T = 100 K for I = 1 mA and T = 110 K for I = 20 mA while cooling. The differences between the resistivity for I = 1 mA and 20 mA at 10 K under $\mu_0 H$ = 5 T is almost negligible compared to the $\mu_0 H$ = 0 T data. The inset shows the resistivity plotted against the surface temperature (T_S) of the sample recorded by the Pt

resistance thermometer thermally anchored to the sample surface. It is seen that the surface temperature of the sample does not go below 75(100) K when I = 10(20) mA even though the base temperature recorded by the PPMS is 10 K. This suggests a strong evidence for Joule heating in the sample at higher current magnitudes.

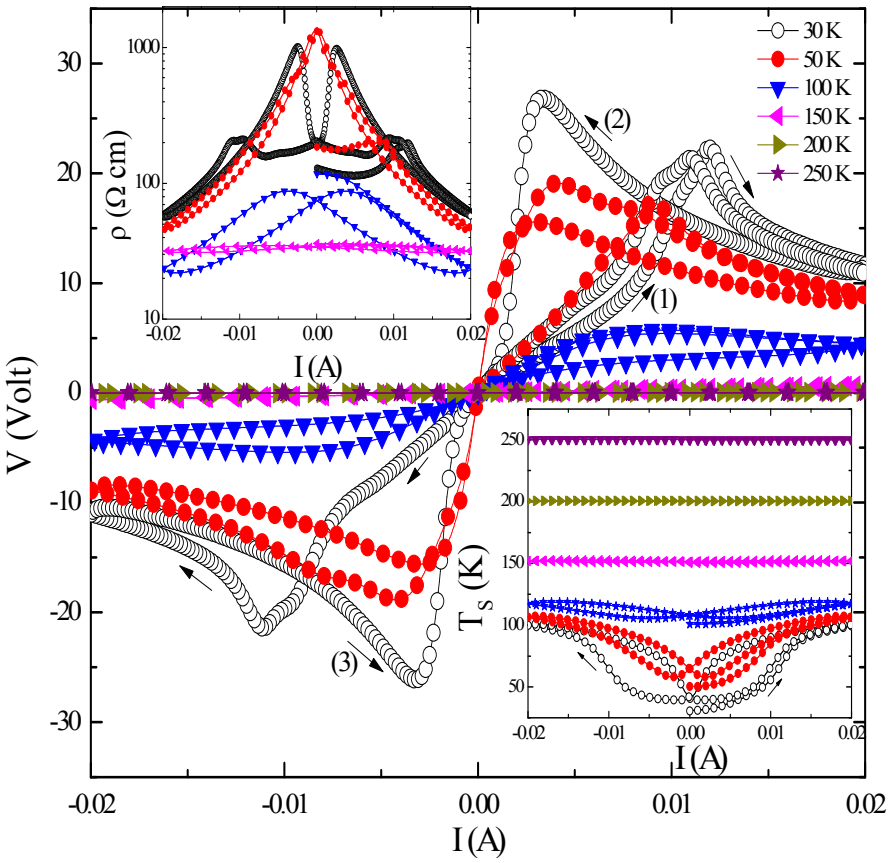

Fig. 3. 8: *V-I* characteristics of the NCMONi05 sample at different temperatures.

The main panel of Fig. 3. 8 shows the *dc* voltage-current (*V-I)* characteristics of the sample at selected stabilized PPMS base temperatures. Three consecutive current sweeps were performed in a complete *V-I* cycle: first sweep from 0 to +20 mA, second sweep from +20 mA to −20 mA and third sweep from −20 mA to +20 mA. The whole measurements were taken with a fixed current sweep rate of 0.5 mA/s and the initial surface temperature (T_S) was ensured to be the same as the stable PPMS base temperature. For this we cooled the sample from 250 K to the respective base temperature before the start of each current cycle at different temperatures. While slower sweep rates than mentioned here has no impact on the *I-V* curves discussed in our results, faster sweep rates give rise to open and irreversible

hysteresis loops. When the current is swept up from 0 to 20 mA at T = 30 K, the voltage shows a sharp increase at lower currents followed by a peak around 10 mA before decreasing at higher currents, thus exhibiting the well known negative differential resistance (NDR) behavior. In the second down sweep from 20 mA to –20 mA and third up sweep from –20 mA to 20 mA, the voltage-current curve traces different paths. Subsequent sweeps trace these curves except the initial one (0 to 20 mA). After a full cycle, a clear hysteresis is observed in the *V-I* characteristics. The peak in the second down sweep is higher in magnitude compared to the peak in the first sweep in the first quadrant in NCMONi05 sample. However, in the parent NCMO compound, the peak in the second down sweep is lower in magnitude compared to the peak in the first sweep in the first quadrant (Fig. 3. 4). The dc *V-I* characteristics in NCMONi05 at other temperatures also exhibit NDR as well as hysteresis, but the hysteresis and strong NDR behavior disappears at higher temperatures as can be seen Fig. 3. 8. The *V-I* characteristics is almost linear at 250 K and above. The top inset shows the resistivity as a function of current at the above selected temperatures. The resistivity change is negative and it often exhibits a butterfly-shape hysteresis with current. The inset at the bottom shows the change in the surface temperature (T_S) of the sample while sweeping the *dc* current. It is found that the observed non-linearity in *V-I* characteristics below 150 K is accompanied by a significant increase in the temperature of the sample. For instance, when the base temperature is 50 K, the surface temperature of the sample increases to as much as 110 K at the highest current I = 20 mA. At higher base temperatures, the voltage-current characteristics become almost linear and a negligible change is observed in the corresponding surface temperature of the sample.

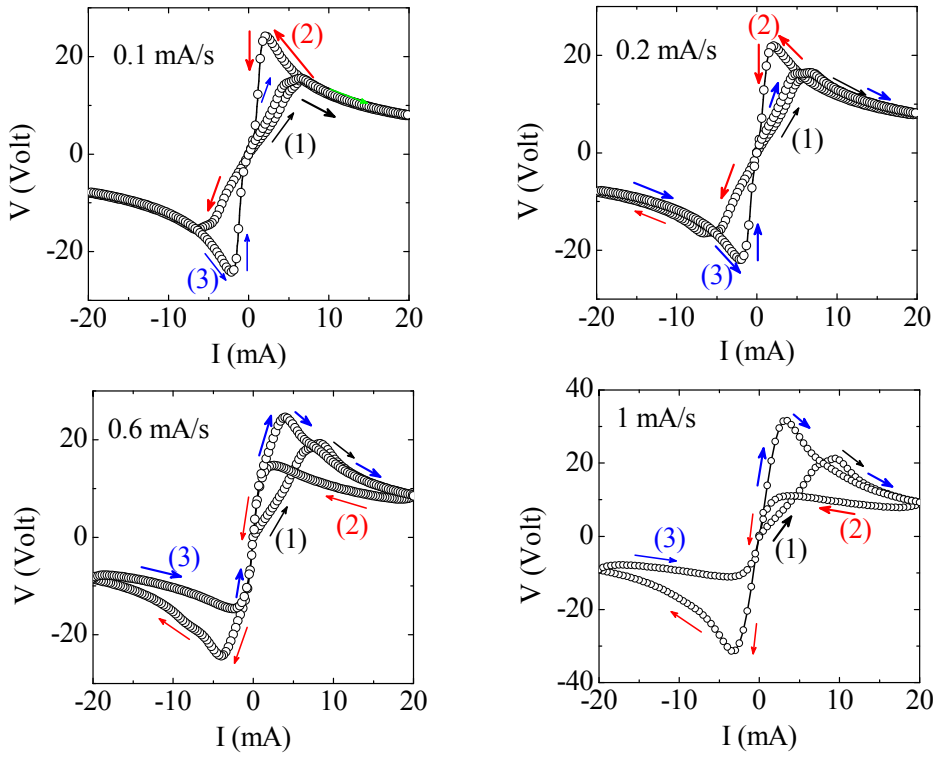

Fig. 3. 9: *V-I* characteristics of the NCMONi05 sample for different sweep rates at *T* = 40 K.

The *V-I* characteristics were later repeated for different current sweep rates at $T = 40$ K (Fig. 3. 9). The arrows in the figure show the direction of the current sweep. The memory effect after the completion of a current cycle with a particular sweep rate is removed by warming the sample to 250 K and then cooling the sample to the 40 K. This protocol is followed for all sweep rates before the start of the current cycle. Though the virgin curve in *V-I* lies outside the subsequent curves for current sweep rate 0.1 mA/s, it can also cross the loops traced in subsequent current cycles (Fig. 3. 9) for higher sweep rates. However, the virgin curve in the $T_S(I)$ lies outside the envelope of subsequent current sweeps for higher sweep rates. The variation of the surface temperature of the sample during the current sweep for different current sweep rates is shown in Fig. 3. 10. The virgin (T_S-*I*) curve deviates from the curves for subsequent current sweeps and shows a difference in the temperature near the origin for sweep rate ≥ 0.2 mA/sec. Also, note the opening of the virgin loop with increasing field sweep rate. For a higher sweep rate (≥ 0.2 mA/sec), the thermal equilibrium is not reached when the current is reduced to zero and hence the sample surface temperature is

higher than the base temperature when current is reduced to zero. As a result, we observe the deviation of the virgin (T_S-I) curve from the curves of subsequent current sweep for higher sweep rates, as illustrated in Fig. 3. 10. Roy *et al*. [87] investigated several charge-ordered manganites with quenched disorder and found that the high temperature charge ordered insulating phase is kinetically arrested with lowering temperature and coexists with low temperature ferromagnetic metallic phase [88]. Such a phase coexistence gives rise to unusual hysteresis loops (virgin curve being outside the envelope curve) in magnetization and magnetoresistance and can show a relaxor ferromagnetic behavior. The magnitude of magnetization and magnetoresistance depends up on the different protocols used in the experiment, for instance field cool warm (FCW), zero field cool (ZFC), etc [87, 88]. Since the temperature of the sample changes by several tens of kelvin during the current sweep in our samples, it is possible that the phase fraction of co-existing phases changes, which in turn changes the resistivity.

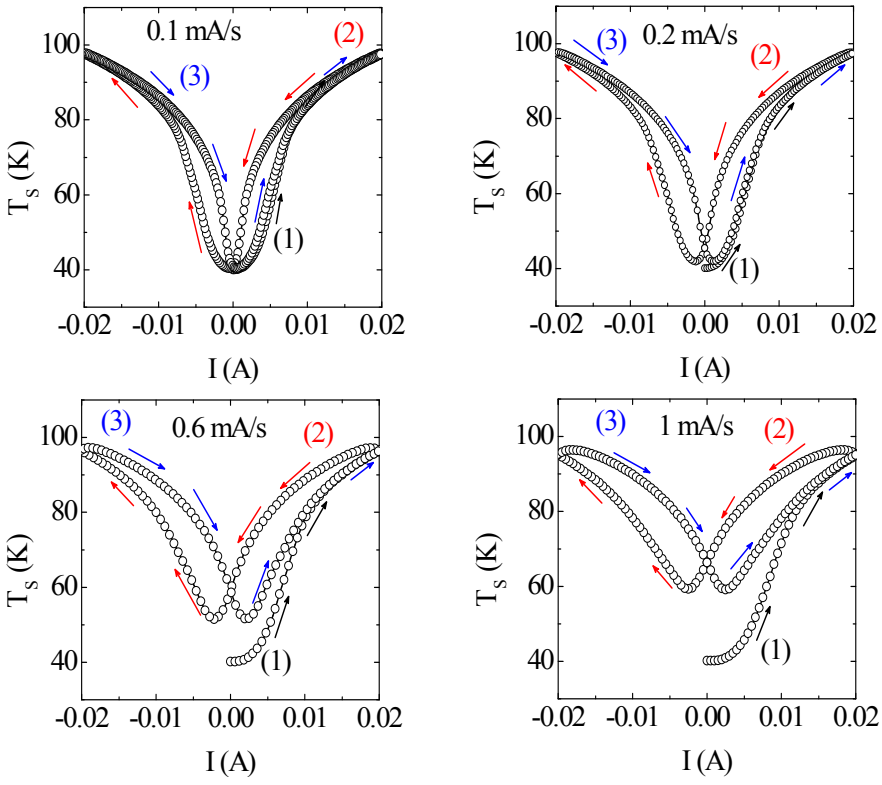

Fig. 3. 10: T_S-I characteristics of the NCMONi05 sample for different sweep rates at T = 40 K.

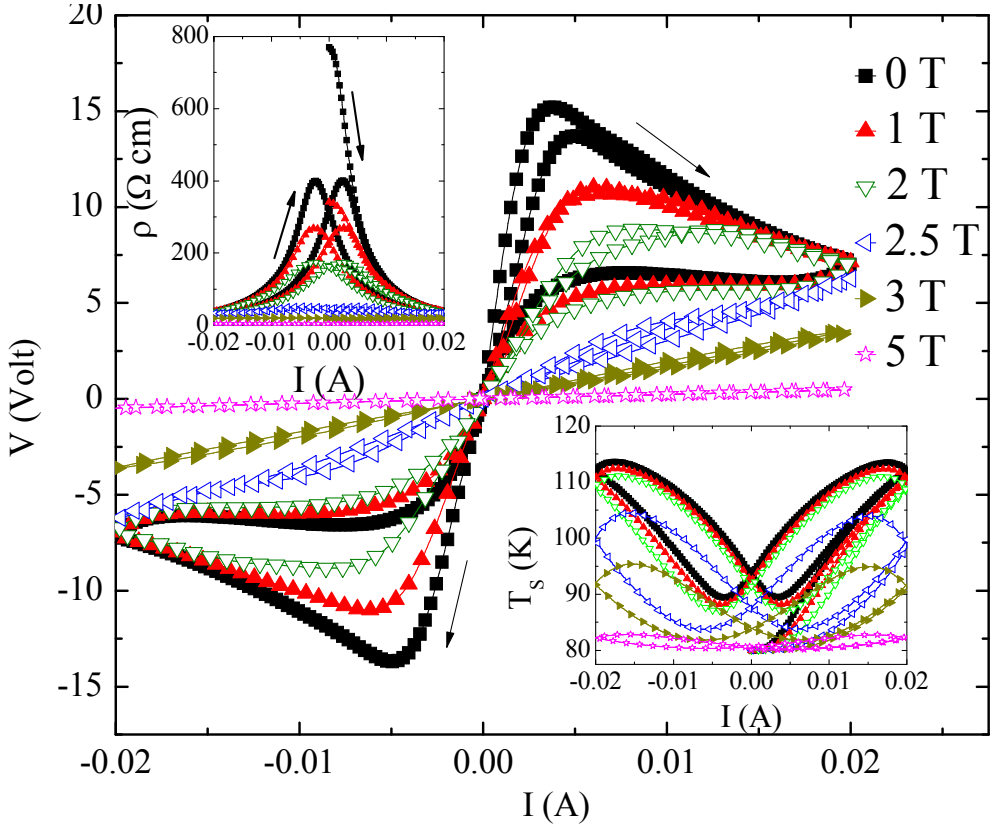

Fig. 3. 11: Main panel: Variation of the *dc V-I* characteristics of NCMONi05 sample under different magnetic fields at *T* = 80 K. The top inset shows the resistivity and the bottom inset shows the variation of the temperature of the sample during the current sweep.

Next we show how the *V-I* characteristics are affected by an external magnetic field. The main panel of Fig. 3. 11 shows the *dc V-I* characteristics of the NCMONi05 sample at *T* = 80 K for $\mu_0 H$ = 0, 1, 2, 2.5, 3 and 5 T. To ensure the initial surface temperature (T_S) same as the stable PPMS base temperature, we cooled the sample from 250 K to the respective base temperature before the start of each current cycle in different magnetic field. When $\mu_0 H$ = 0 T, the voltage shows a peak around *I* = 3 mA during the initial current sweep (0 to +20 mA). A large reversible hysteresis occurs upon subsequent current sweep. The voltage peak decreases in magnitude and shifts to a higher current value with increasing *H*. The hysteresis also decreases with increasing *H*. The peak is no more visible within the measured current range for $\mu_0 H \geq 2.5$ T. The top inset shows the resistivity and the bottom inset shows the corresponding change in the top surface temperature of the sample in different magnetic

fields. The temperature of the sample increases as much as 35 K above the base temperature during the current sweep in zero magnetic field but the change becomes smaller (ΔT ~3 K) when $\mu_0 H$ = 2 T and almost negligible for $\mu_0 H$ > 3 T. These results indicate a close competition between Joule heating and magnetic field to determine the threshold current in the NDR behavior. As the applied magnetic field decreases the resistance (R), the power dissipation in the material ($P = I^2R$) decreases and hence more current is required to induce NDR. So the voltage peak shifts towards higher value of current under higher magnetic fields. However, the position of the peak in the V-I characteristics at T = 80 K in the parent NCMO sample under $\mu_0 H$= 0 and 7 T does not show a large difference compared to the Ni doped sample, though the magnitude of the peak is decreased under $\mu_0 H$ = 7 T, as exemplified in Fig. 3. 12. The inset shows the variation of the temperature of the sample during the current sweep in NCMO sample.

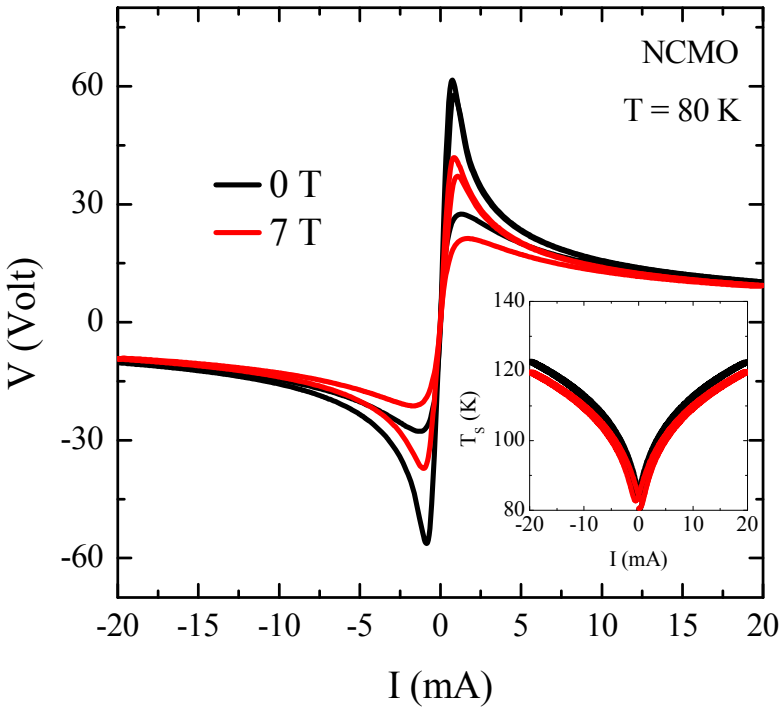

Fig. 3. 12: The V-I characteristics of parent NCMO sample under $\mu_0 H$= 0 and 7 T at T = 80 K. The inset shows the variation of the temperature of the sample during the current sweep.

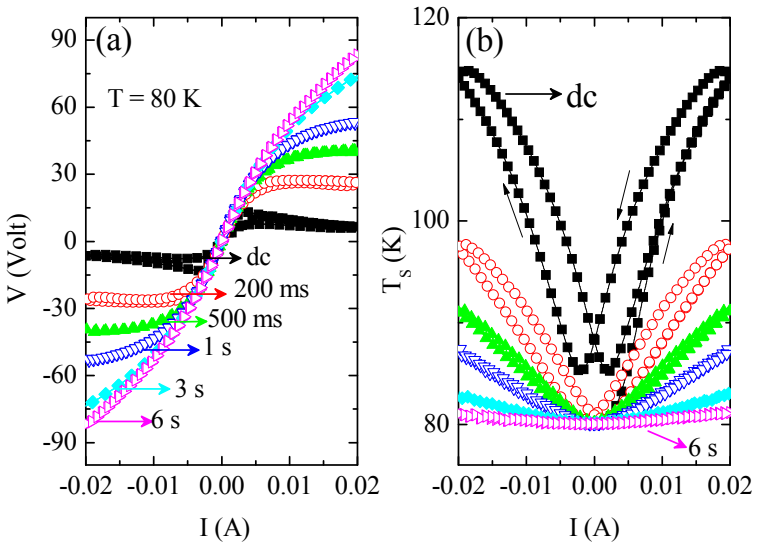

Fig. 3. 13: (a) *V-I* characteristics NCMONi05 sample at *T* = 80 K for different periods (P_D) of the pulsed current. The pulse width (P_W) is fixed to 200 ms. The *dc* data is also shown. (b) The change in the sample surface temperature during the current sweep.

Fig. 3. 13(a) compares the *dc* and pulsed *V-I* sweep of NCMONi05 sample at T = 80 K. The pulsed *V-I* sweeps were done with pulses of width, P_W = 100 ms and five different pulse periods, P_D = 200 ms, 500 ms, 1 s, 3 s and 6 s. It can be seen that the peak in voltage and NDR at higher currents observed in the *dc* current sweep disappear progressively with increasing pulse period. The magnitude of the voltage at the highest current keeps increasing with the pulse period (i.e., towards a high resistive state). The non-linearity in the *V-I* persists even for the longest period (P_D = 6s). Fig. 3. 13(b) shows that the *dc V-I* sweep is accompanied by a significant increase in the surface temperature of the sample (~35 K), while the change in temperature decreases with increasing pulse period. The temperature change is only about 1 K for the pulsed sweep with P_D = 6 s. The above difference in the voltage-current sweeps for the pulsed and direct current behavior suggests that caution should be taken while attributing the negative differential resistance to unpinning of charge density waves alone [89]. We believe that at a pulsed current of shorter pulse width or longer pulse period, intrinsic mechanisms possibly dominate over the thermal effects. Since the sample is phase segregated, the observed non linearity for the longer pulse period could also arise from the tunneling between ferromagnetic clusters embedded in charge ordered matrix.

All the above results indicate that Joule heating is significant in the *dc* current sweep, nevertheless it can be systematically controlled by manipulating the period of the current pulse and provide information about the contribution of other mechanisms in electroresistance. Hence we investigated the resistivity switching in NCMONi05 sample at T = 80 K. Fig. 3. 14(a) shows the response of the resistivity (left scale) in response to six pulse trains with a fixed pulse period (P_D = 0.5 s) and pulse width (P_W = 25 ms) but with two different current amplitudes, I = 2 and 10 mA. Consecutive pulse trains consist of 400 pulses of I = 2 mA and 400 pulses of I = 10 mA. Arrows in the figure indicate the start of a new pulse train. The resistance shows an abrupt increase by 50 % when the amplitude of I is decreased from 10 mA to 2 mA and remains nearly unchanged until another pulse of a larger amplitude (I = 10 mA) sets it to a low resistance state. The resistance can be again set to the high value upon application of smaller current amplitude (I = 2 mA). The surface temperature of the sample, shown on the right scale, changes periodically from 87 K for I = 10 mA to 82 K for I = 2 mA.

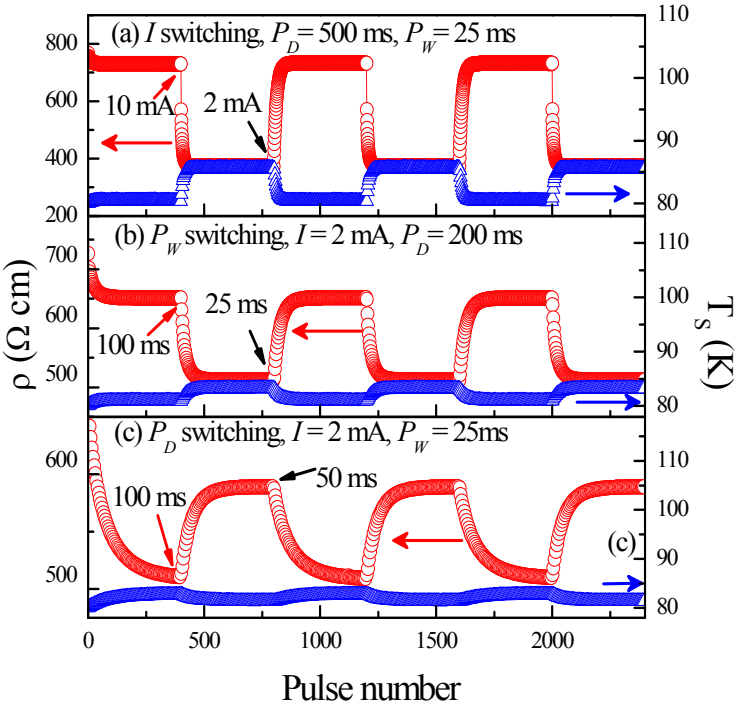

Fig. 3. 14: Resistivity switching in NCMONi05 sample at T = 80 K due to (a) change in the amplitude of the current (b) change in the pulse width (P_W = 100 ms to 25 ms) for I = 2 mA and P_D = 200 ms (c) change in the pulse period (P_D= 100 ms to 50 ms) for I = 2 mA and P_W = 25ms.

In Fig. 3. 14(b), we show a resistivity switching in response to six pulse trains with a fixed current of lower amplitude (I = 2 mA) and pulse period of 200 ms but for two different pulse widths P_W = 25 ms and 100 ms in NCMONi05 sample. Consecutive pulse trains consists of 400 pulses of P_W = 25 ms and 400 pulses of P_W = 100 ms. The resistance decreases by 25 % upon changing the P_W from 25 ms to 100 ms and the temperature also changes by 3 K. Similarly, a change of 16 % is obtained in a pulse period induced switching between P_Ds 50 ms and 100 ms pulses of fixed P_W 25 ms and amplitude 2 mA, as shown in Fig. 3. 14(c). In this case, the temperature changes by 1 K.

At present, the exact origin of the pulse width controlled resistance switching is not clearly understood. It is possible that longer is the pulse width, the continuous supply of energy ($W = I^2Rt_{pw}$ where t_{pw} is the pulse width) causes the self heating of the sample and thereby leads to a decrease in the resistance because $d\rho/dT<0$. So, increasing (decreasing) the pulse width of the pulses in one train to apply the second pulse train leads to heating (cooling) of the sample, which inturn leads to transition between low and high resistance states. Similarly, if the period of pulses in a pulse train is short, the sample does not have much time to dissipate the heat and hence the temperature of the sample is still high. Hence, shorter period leads to lower resistance state than the longer period pulse train with the same pulse width. However, the observed change in the temperature during switching [Fig. 3. 14(b) and Fig. 3. 14(c)] is only about 1-3 K, which is not uncommon in conventional transistor or diode based devices. While the minority carrier tunneling through the depletion region is the primary cause of the non linear conduction in the diodes and transistor, Joule heating is a side effect.

There are other non-thermal mechanisms which can also account for the observed effect. In electronically and magnetically inhomogeneous systems such as the NCMONi05, electrons are delocalized within ferromagnetic phase but localized in the charge ordered phase. While the electrical conduction primarily occurs through the percolating ferromagnetic phase below the semiconductor-metal transition, electron transfer between disconnected ferromagnetic domains in the semiconducting state occurs through tunneling into and out of

the charge ordered phase which acts like traps. In general, there will be distributions in the potential well (depth) of the traps and hence different life times. For a fixed pulse period, when pulse width is longer, charge carriers find enough time to tunnel through the well or get excited out of the well and contribute to electrical conduction leading to decrease in the resistance as observed in Fig. 3. 14(b). Hsu *et al*. [90] obtained qualitatively similar pulse width dependent results in metal-$Pr_{0.7}Ca_{0.3}MnO_3$-metal device (two probe configurations) though the authors did not measure the temperature change or the pulse parameter dependent *V-I* characteristics. It was suggested that the density of excessive nonequilibrium electrons near the cathode of the device caused the free valence electrons in the metal oxides to be localized. If the pulse width is larger than the relaxation time constant, the density of the nonequilibrium electron package injected from the cathode region is small. The high field intensity at the cathode region delocalizes the valence electrons. Recently, a charge trap model was proposed by Rozenberg and collaborators [43, 91]. According to Rozenberg *et al*. there is a variation of the concentration of oxygen vacancies near the interface ("interfacial domains"). Under the action of alternative pulsing, oxygen vacancies moves back and forth between central region ("bulk") and interfacial domains thus effectively doping the central region. Thus pulsed current switching modifies the carrier concentration and it can explain the pulsed current or voltage induced resistance behavior. Finally, even though our results suggest that the Joule heating is non-negligible in the compound investigated, thermally controllable electrical switching may find other applications such as current limiters [92].

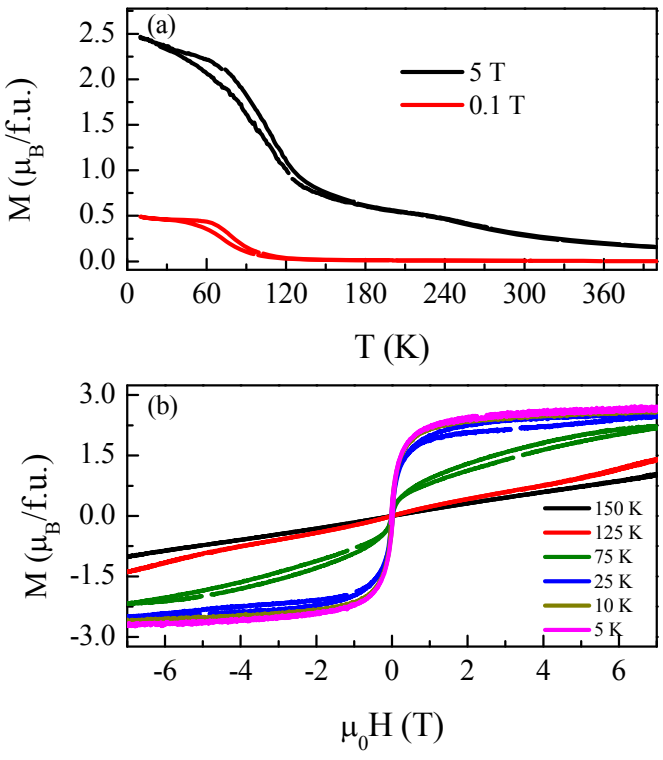

Fig. 3. 15: (a) Temperature dependence of the Magnetization (*M*) of NCMONi07 sample at $\mu_0 H$ = 0.1 and 5 T. (b) *M* vs. *H* curves at different temperatures.

The 7% Ni doped NCMO sample also shows qualitatively similar results to the 5% Ni doped sample discussed before. Fig. 3. 15(a) shows the magnetization (*M*) versus temperature (*T*) curves of $Nd_{0.5}Ca_{0.5}Mn_{0.93}Ni_{0.07}O_3$ (NCMONi07) at $\mu_0 H$ = 0.1 and 5 T. Upon cooling from 400-10 K, the sample undergoes a paramagnetic to ferromagnetic transition around the Curie temperature T_C = 63 K, inferred from the inflection point in the derivative of *M*-*T* curve under $\mu_0 H$ = 0.1 T. The T_C is shifted to a higher temperature (T_C = 95 K) at $\mu_0 H$ = 5 T. Fig. 3. 15 (b) shows the isothermal magnetization (*M*) versus field (*H*) curves at selected temperatures. These *M*-*H* curves are identical to the data for NCMONi05 sample (please see the inset of Fig. 3. 6 and its description), thus indicating that NCMONi07 also exhibits phase separation at low temperatures.

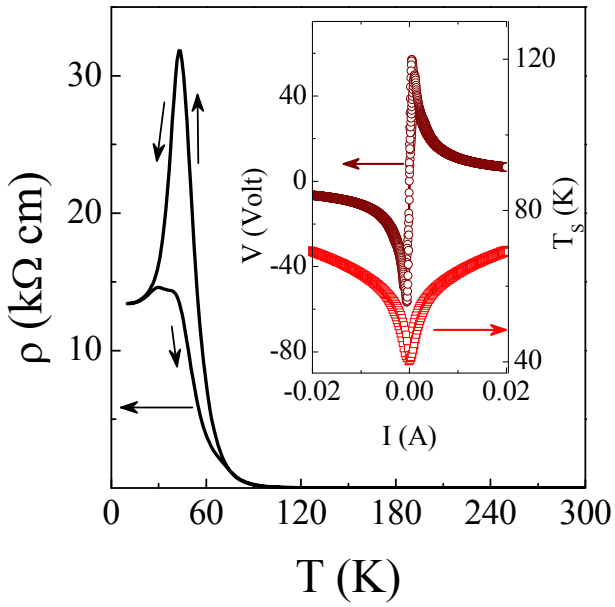

Fig. 3. 16: Main panel shows temperature dependence of the zero field *dc* resistivity (ρ) of the NCMONi07 sample. The inset shows the voltage-current (*V-I*) characteristics (on the left scale) at 40 K and the concomitant change in the surface temperature (T_s) (on the right scale).

Now let us look into the electroresistance behavior in NCMONi07 sample. The main panel of Fig. 3. 16 shows the temperature dependence of the zero field dc resistivity (ρ) of the NCMONi07 sample measured with I = 100 μA. The sample shows a temperature driven semiconductor to metal transition with a peak in the resistivity occurring around T_P = 44 K while cooling. The $\rho(T)$ while warming is lower than while cooling in the temperature range T = 25-70 K and both the curves merge above 80 K. The very high value of resistivity, ρ = 13.4 kΩ cm at 10 K suggests that the sample is electrically and magnetically inhomogeneous due to coexistence of the ferromagnetic metallic and short-range charge ordered antiferromagnetic insulating phases. The semiconductor to metal transition upon lowering the temperature is due to the percolation of ferromagnetic clusters in the short range charge-ordered paramagnetic matrix, similar to 5 % Ni doped $Nd_{0.5}Ca_{0.5}MnO_3$. The inset shows the voltage-current (*V-I*) characteristics at 40 K (on the left scale) which exhibits a negative differential resistance behavior. The non-linear electrical conduction is accompanied by a significant increase in the temperature of the sample from 40 K to 69 K as shown on the right scale.

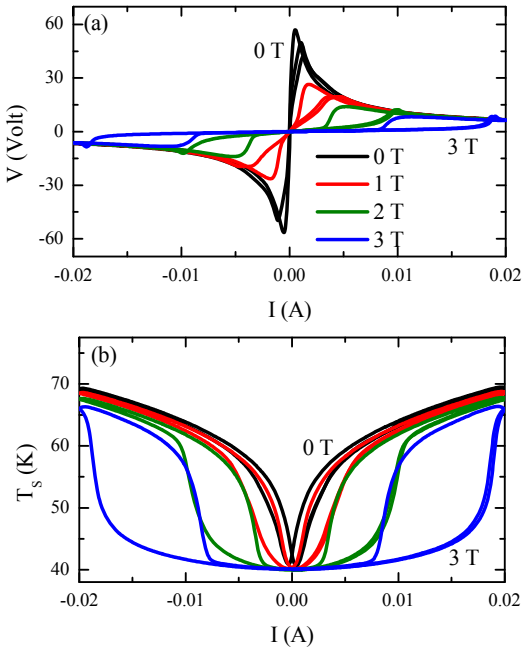

Fig. 3. 17: (a) The voltage-current (*V-I*) characteristics of NCMONi07 sample in different magnetic fields (*H*) at 40 K. (b) The concomitant changes in the surface temperature of the sample (T_S) as measured by the Pt-resistance sensor glued to the top of the sample during the current sweep.

Fig. 3. 17(a) displays the voltage versus current (*V-I*) characteristics of the NCMONi07 sample under different magnetic fields at T = 40 K. The whole measurements were taken with a fixed current sweep rate of 0.1 mA/s and the initial surface temperature (T_S) was ensured to be the same as the stable PPMS base temperature. The sample shows a strong nonlinear behavior at $\mu_0 H$ = 0 T. Apart from the strong negative differential resistance behavior, the *V-I* curve exhibits a hysteresis around the origin. While a sharp NDR peak is observed around I = 3 mA in the intial current sweep (0→20 mA) at $\mu_0 H$ = 0 T, a broad NDR peak is observed in the initial current sweep at $\mu_0 H$ = 1 T around I = 7 mA, along with a noticeably large hysteresis around the peak. At higher magnetic fields, the magnitude of the peak decreases, the peak position shifts to higher current and the hysteresis broadens. For instance, the position of the peak is shifted from $I \approx 3$ mA in $\mu_0 H$ = 0 T to $I \approx 18$ mA in $\mu_0 H$ = 3 T and the magnitude of the peak decreases from V = 55 V at 0 T to V = 5 V at 3 T. The corresponding behavior of the surface temperature of the sample during the above measurements is shown in Fig. 3. 17(b). Note that the direct response of the sample surface temperature is not explicitly

measured in the vast amount of literature reporting NDR behavior in manganites and similar systems. At $\mu_0 H$ = 0 T, the NDR behavior is accompanied by a noticeable change in the T_S, where the temperature increases from T_S = 40 K to 69 K as the current increases from I = 0 mA to 20 mA, along with a hysteresis close to the origin. The T_S at higher magnetic fields also shows large changes during the current sweep, i.e. a rapid increase above a certain current value and a huge hysteresis while reducing the current. The shape of the temperature profile changes with magnetic field. Interestingly, the T_S-I curve at $\mu_0 H$ = 3 T shows a large hysteresis away from the origin compared to the T_S -I curve at $\mu_0 H$ =0 T.

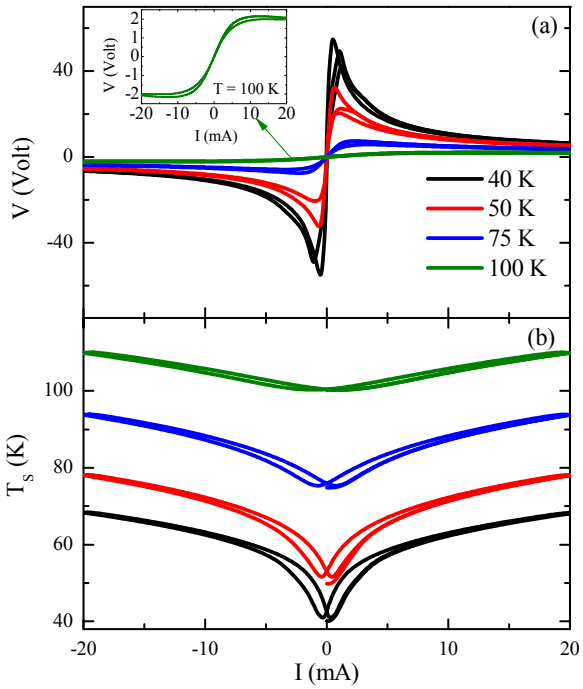

Fig. 3. 18: (a) The nonlinear *V-I* characteristics at different temperatures in NCMONi07. (b) The changes in the surface temperature T_S during the current sweep.

Next, we show the *V-I* characteristics of the NCMONi07 sample at different temperatures in zero magnetic fields in Fig. 3. 18(a). The inset of Fig. 3. 18(a) shows the *V-I* curve at T = 100 K for better clarity. We observe nonlinearity in the *V-I* characteristics at all the temperatures below 100 K. However, the sharp peak in the NDR behavior observed at low temperatures is absent in the *V-I* curve at T = 100 K, as can be seen in the inset. The

nonlinearity as well as the NDR behavior is not observed at higher temperatures (data not shown here). As the base temperature increases, the change in T_S decreases [Fig. 3. 18(b)].

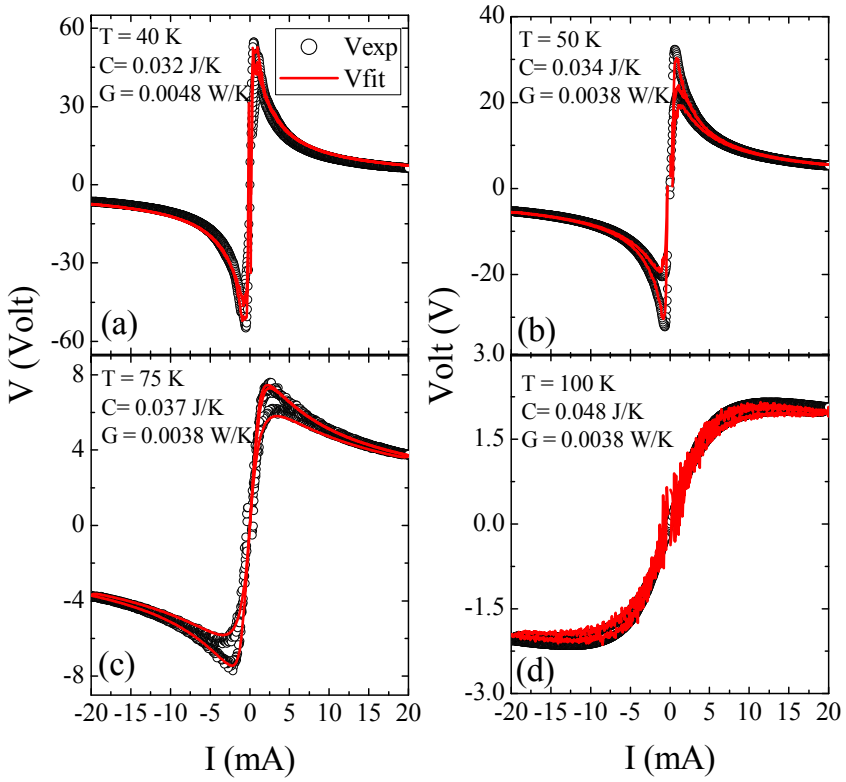

Fig. 3. 19: Simulation of the nonlinear *V-I* characteristics at T = 40, 50, 75 and 100 K (solid lines) and the experimental *V-I* curves (open symbols) of NCMONi07 samples. The numbers indicate the parameters used in the fit.

In spite of the various mechanisms attributing NDR to different plausible mechanisms (as mentioned in the introduction), the direct observation of concomitant changes in the T_S [for instance, see Fig. 3. 18(b)] during the current sweep points to the nontrivial influence of thermal mechanisms which strongly govern the nonlinear dynamics in the sample. Let us consider the bottom of our sample is maintained at a constant temperature T which is equivalent to the environmental temperature stabilized by the temperature controller. The power dissipated by the current passing through the sample, $P = RI^2$ will easily heat up the top surface of the sample, which in turn is measured as T_S in our experiments. The thermal processes depend on the thermal conductance and heat capacity of the bulk sample. In fact, the nonlinear transport observed in our experiments can be well described quantitatively by a

phenomenological electrothermal model [93] following the energy balance equation, $C\frac{dT_S}{dt} = P - G(T_S - T)$, where C is the heat capacity of the sample, t denotes the time and G stands for the effective thermal conductance or the energy transfer rate, which depends on the shape of the sample and surface area. The term $-G(T_S - T)$ represents the Newtonian cooling in the system. Chen *et al*. [94] has numerically solved the aforementioned energy balance equation for various sweep rates r of the current ramp in the *V-I* sweep, using experimentally measured $R(T)$ curve of the LCMO film as a numerical input. In the present study, we use a different approach to reproduce the nonlinear conductivity observed in our sample by directly measuring the rate of change of T_S without any approximations. Surprisingly, an excellent agreement between the theoretical fit and the experimental data is observed for the complete current sweep. Fig. 3. 19 shows the experimental and theoretical fit nonlinear *V-I* curves at T = 40, 50, 75 and 100 K. Nonlinear transport studies in high field are also interpreted in the literature in terms of the hot electron phenomena [95] where the energy balance equation transforms to $C\frac{dT_e}{dt} = P - G(T_e - T)$, where T_e is a hypothetical electron temperature characterizing the population of the excited states, elevated from the lattice temperature T. It is assumed in those models that the lattice temperature or the phonon temperature is identical to the environmental T due to a strong coupling between the lattice and the thermal bath, but is decoupled from T_e. However, the lattice temperature was not explicitly measured by those authors and therefore the possibility of hot electron effects in our sample requires an elaborate investigation. It is likely that the nucleation and growth of such hot spots can affect the dynamical nature of the nonlinear conductivity observed in the present study.

3. 4 Conclusions

In summary, we have shown that *dc* current-induced colossal electroresistance at high current strength in $Nd_{0.5}Ca_{0.5}MnO_3$ and phase separated Ni-doped $Nd_{0.5}Ca_{0.5}MnO_3$ samples are related to the self-heating of the sample. However, non linearity in *V-I* characteristics does not vanish even with a pulsed current of a long (6 s) pulse-period in $Nd_{0.5}Ca_{0.5}Mn_{0.95}Ni_{0.05}O_3$ which suggests that intrinsic mechanism of non-thermal origin is operative. It is shown that resistance can be switched not only with the amplitude of the current but also by changing the period and width of pulses. Though possible origins of the observed effects were suggested, a more detailed investigation in future will be helpful.

Chapter 4

Current induced magnetoresistance avalanches in Ni-doped $Nd_{0.5}Ca_{0.5}MnO_3$

4. 1 Introduction

In chapter 3, we discussed electroresistance properties in the phase separated Ni doped $Nd_{0.5}Ca_{0.5}MnO_3$ compounds, both in dc as well as pulsed- current modes. The role of phase separation on the non linear electrical conduction in 5(7) % Ni doped samples was discussed in detail. The purpose of this chapter is to investigate the effect of dc current strength on the magnetic field dependence of magnetoresistance in these samples. We show that the magnetoresistance in these compounds decreases smoothly with increasing magnetic field at lower current strengths (I < 5 mA), but it changes into an avalanche type (a step-like decrease) at a critical value of the magnetic field for higher current strengths (I > 5 mA). Surprisingly, the avalanche in magnetoresistance is accompanied by an abrupt change in the temperature of the sample ($\Delta T \approx$ 47 K). The memory effect, observed in the magnetoresistance upon field cycling, is dramatically affected under increasing magnitude of the dc current.

4. 2 Experimental Section

We have measured the four probe resistance of bar shaped polycrystalline $Nd_{0.5}Ca_{0.5}Mn_{0.95}Ni_{0.05}O_3$(NCMONi05) and $Nd_{0.5}Ca_{0.5}Mn_{0.93}Ni_{0.07}O_3$(NCMONi07) samples of dimensions 6×3×2 mm^3, as a function of the magnetic field (H) at different values of the dc current and at selected base temperatures. During the magnetic field sweep, the surface temperature of the sample (T_S) was also measured simultaneously, with a Pt-100 sensor attached to the top surface of the sample between voltage probes. The base temperature of the sample, as recorded by the cryostat is denoted by T in this chapter, unless otherwise stated. The dc current in the sample is perpendicular to applied magnetic field. The details of the experimental set up are discussed in chapter 2.

4. 3 Results

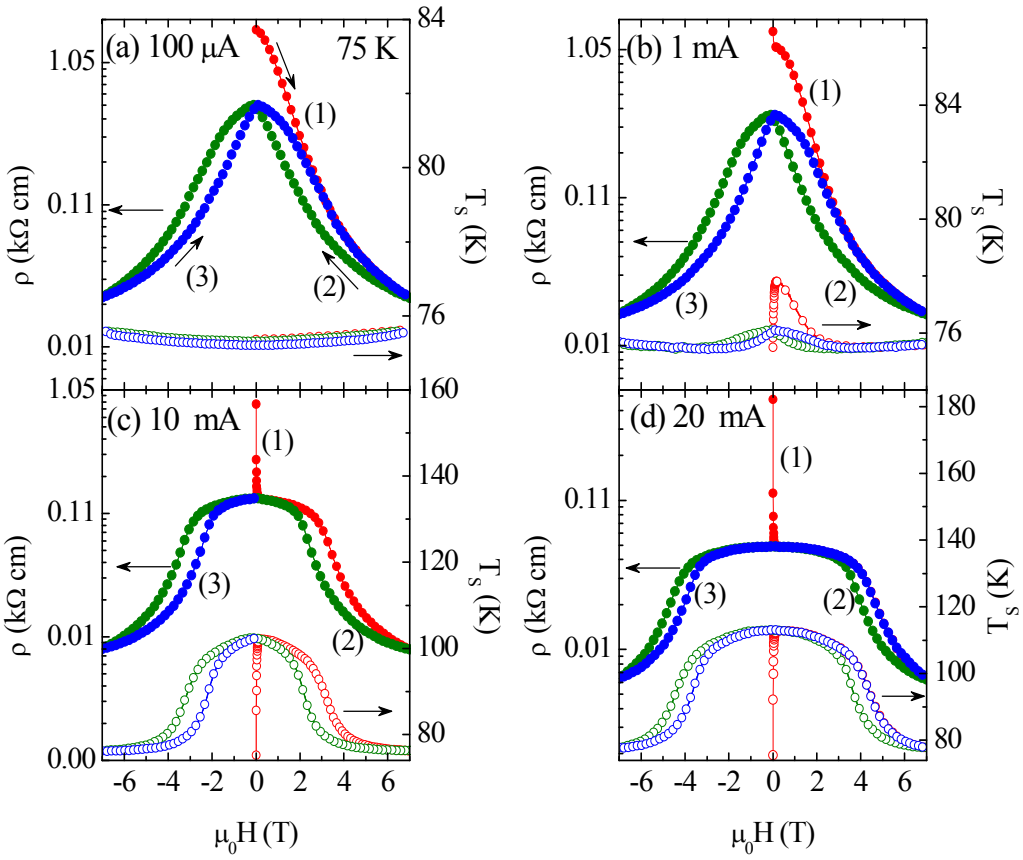

Fig. 4. 1: The magnetic field (*H*) dependence of resistivity (ρ) (on the left scale) and surface temperature (T_s) (on the right scale) of NCMONi05 sample at T = 75 K for different current strengths, I = (a) 100 μA, (b) 1 mA, (c) 10 mA, and (d) 20 mA.

As already seen in the previous chapter, magnetic field has a dramatic influence on the electroresistance and electrical transport in phase separated Ni doped NCMO compounds. Since these phase separated samples show a remarkable magnetoresistance (MR) at low temperatures [96], we have investigated the influence of various current strengths on the magnetic field dependence of resistivity (ρ). In Fig. 4. 1, we show the influence of current amplitude on the *H*- field dependence of the resistivity of NCMONi05 sample at T = 75 K. Fig. 4. 1(a)-(d) show the field dependence of ρ on the left scale and T_S on the right scale for a few selected current strengths, I = 100 μA, 1, 10 and 20 mA. As soon as the current was applied to the sample, the magnetic field sweep was started with a constant sweep rate of 80 Oe/sec. To erase the memory effect, I was reduced to zero after each field cycle and the

sample was warmed up to 150 K, then cooled to 75 K without applying any current. The complete *H*-field cycle consists of three consecutive sweeps: the first (0 → +7 T), second (+7 T → 0 → –7 T) and the third (–7 T → 0 → +7 T) sweeps are indicated by (1), (2) and (3), respectively. When I = 100 μA, during the first sweep (Fig. 4. 1(a)), ρ decreases gradually with increasing H. Then, ρ traces a different, low resistive path upon sweeping the field from $\mu_0 H$ = +7 T to $\mu_0 H$ = – 7 T in the second sweep. In the third sweep (H = -7 T to +7 T), ρ remains still in the low resistive state, but shows a small hysteresis. This type of irreversibility in the first and second field sweep and a persistent memory effect in magnetoresistance and magnetization are found in other phase separated manganites also [96, 97]. The temperature of the sample, T_s increases gradually ($\Delta T \approx 0.3$ K) with magnetic field in both the directions of the magnetic field, as can be seen in the right scale of Fig. 4. 1(a). This apparent increase in the temperature of the sample is an artifact coming from a small positive magnetoresistance (about 0.7 % at $\mu_0 H$ = 7 T) of the PT100 resistor at T = 75 K (Fig. 4. 2), which corresponds to a temperature increase of ≈0.3 K according to the callibration.

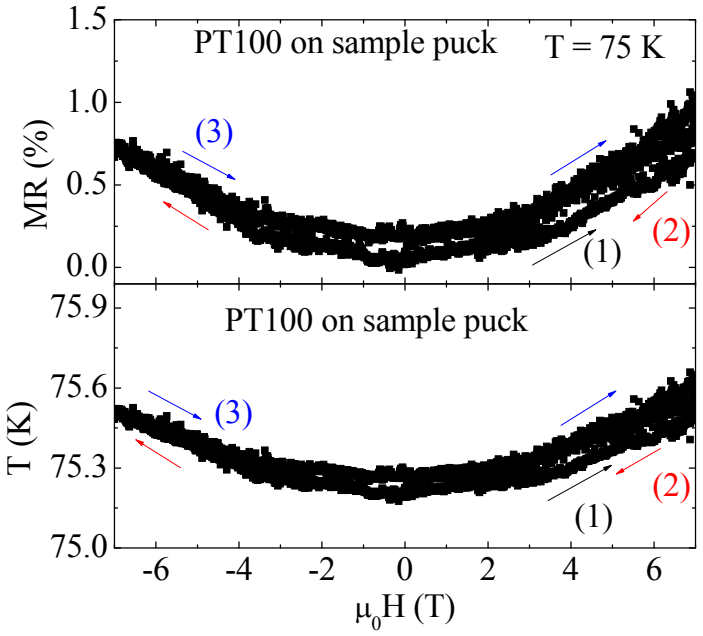

Fig. 4. 2: Four probe magnetoresistance (MR) of PT100 resistor and associated temperature change (artifact) at 75 K (right panel).

The ρ-H curve for I = 1 mA (Fig. 4. 1(b)) shows a similar behavior like for I = 100 μA, but with a sharp initial decrease in the beginning of the field sweep, which is accompanied by a sharp initial rise in T_S. At higher current amplitudes I = 10 and 20 mA, ρ shows a plateau up to a certain field strength and then shows a steep decrease, as shown in Fig. 4. 1(c) & Fig. 4. 1(d), respectively.

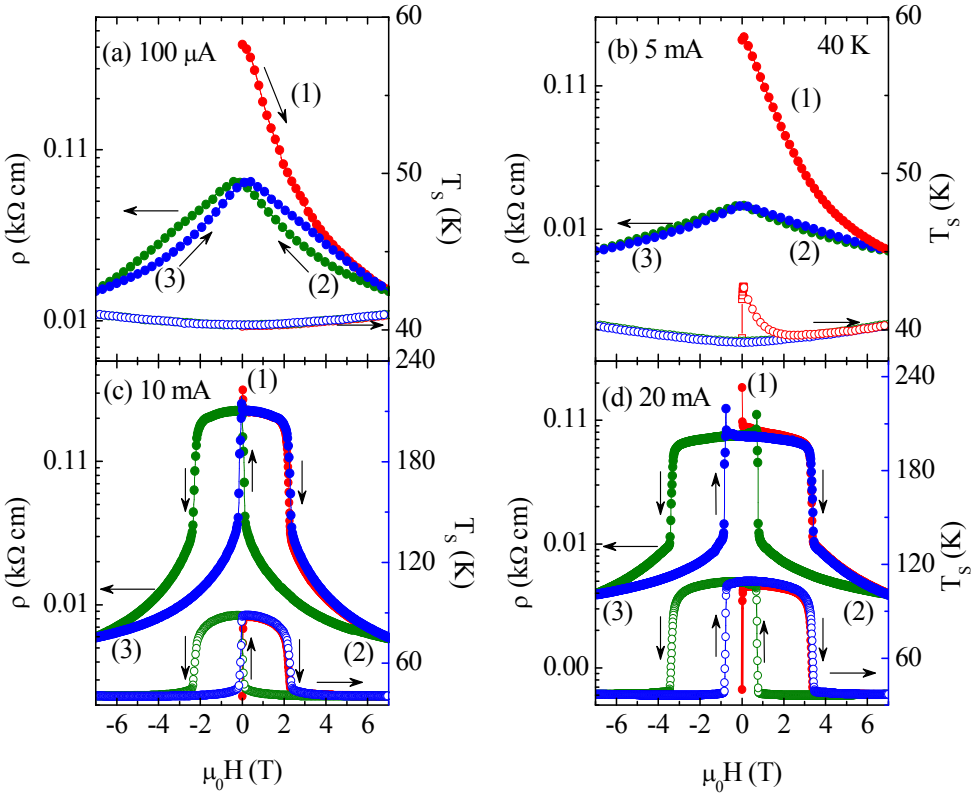

Fig. 4. 3: The magnetic field dependence of resistivity (ρ) (on the left scale) and surface temperature (T_s) (on the right scale) of NCMONi05 sample at T = 40 K for different current strengths, I = (a) 100 μA, (b) 5 mA, (c) 10 mA, and (d) 20 mA.

In Fig. 4. 3, we show influence of current strength on the H-field dependence of the resistivity at T = 40 K. The left scale shows the ρ-H isotherms and the right scale shows the corresponding T_S-H curves measured for selected current strengths, (a) I = 100 μA, (b) 5 mA, (c) 10 mA, and (d) 20 mA. The ρ-H curves during the complete field cycle at T = 40 K for I = 100 μA [Fig. 4. 3(a)] resembles the ρ-H curves at T = 75 K for I = 100 μA [Fig. 4. 1(a)]. Note that the first curve is well separated from the second and third curve (low resistive states) at T = 40 K, compared to that at T = 75 K. The ρ-H curves for I = 5 mA also shows a similar

behavior [Fig. 4. 3(b)]. When I = 10 mA is applied [see Fig. 4. 3(c)], ρ initially decreases sharply near the zero field and then decreases gradually as H increases. Surprisingly, an avalanche (a step- like decrease) in ρ occurs at $\mu_0 H$ = 2.1 T instead of a smooth decrease observed earlier. The sharp decrease in the resistivity near $\mu_0 H$ = 0 T is accompanied by a sharp increase in the temperature of the sample from T_s = 40 K to 88 K as can be seen in the right scale of Fig. 4. 3(c). The temperature remains nearly constant at 88 K as the field increases, until $\mu_0 H$ = 2.1 T. Then, T_s also shows an avalanche effect, wherein the temperature of the sample abruptly drops to $T_S \approx$ 41 K at $\mu_0 H$ = 2.1 T, thus coinciding with the avalanche in the resistivity. When H is further increased from 2.1 T to 7 T, the T_s shows an increase of less than 1 K. When H is reduced from 7 to 0 T, ρ does not remain at the low resistive persistent state unlike what was observed for I = 100 μA and 1 mA. Instead, it shows the avalanche effect, but this time, a step-like increase at $\mu_0 H$ = 0.1 T. Upon reversing the field, $\rho(H)$ shows the avalanche effect again (high resistance to low resistance transition) at $\mu_0 H$ = -2.1 T. A similar behavior of ρ is observed in the third sweep with an abrupt increase from a low to a high resistive state at $\mu_0 H$ = –0.1 T followed by an abrupt decrease to a low resistive state again at $\mu_0 H$ = 2.1 T. This, eventually results in a huge hysteresis close to the origin ($\mu_0 H$ = 0 T). The temperature T_s, follows a similar trend. The T_s decreases abruptly from 88 K to 41 K when the resistivity abruptly decreases at $\mu_0 H$ = 2.1 T during first field sweep and then increases abruptly at $\mu_0 H$ = 0.1 T when the field is reduced to 0 T [right scale, Fig. 4. 3(c)].The ρ-H curves for I = 20 mA [Fig. 4. 3(d)] exhibits similar behavior as the ρ-H curves for I = 10 mA, except that the hysteresis in the field dependence occurs far from $\mu_0 H$ = 0 T and the avalanche becomes sharper .

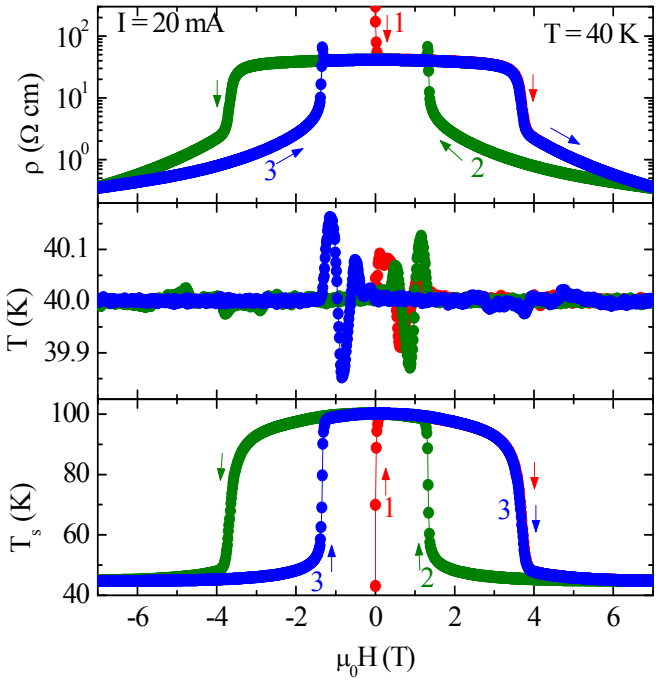

Fig. 4. 4: Field dependence of resistivity of NCMONi05 sample at 40 K for *I* = 20 mA (top panel), temperature recorded by the cryostat (middle panel) and temperature measured by the Pt –sensor glued to the top surface of the sample (bottom panel).

It is quite reasonable at this point to be curious about the actual behavior of the cryostat temperature during the field sweep. In Fig. 4. 4, we compare the temperature of the NCMONi05 sample recorded by the Pt –resistor (bottom graph) with the base temperature recorded by the PPMS (middle graph) and the resistivity (top graph) for I = 20 mA during the magnetic field sweep in NCMONi05 sample. It is to be noted that the base temperature fluctuates while reducing the magnetic field sweep from ± 7 T, but the fluctuation does not exceed more than ±0.3 K. The temperature variation recorded by the cernox sensor in the cryostat is negligible compared to the temperature recorded by the temperature sensor attached directly to the top surface of the sample. Hence, the change in temperature of the sample is not so apparent if we rely on the temperature recorded by the PPMS alone.

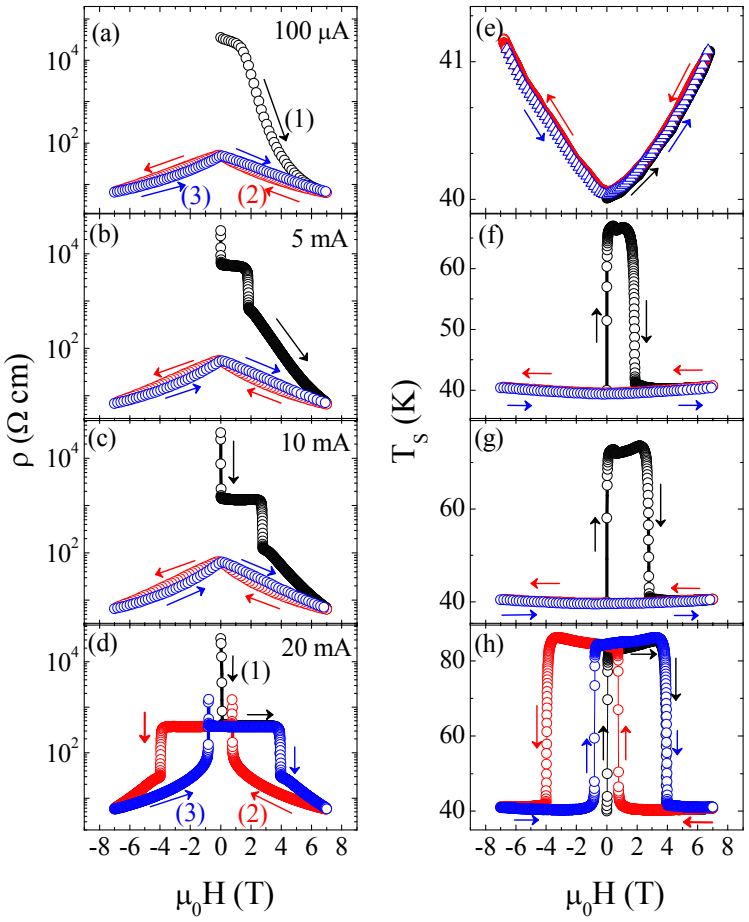

Fig. 4. 5: Left column shows the field dependence of resistance at T = 40 K for different current strengths and the right column shows the corresponding changes in the sample temperature (T_s) in NCMONi07 sample.

Next, we show the influence of current amplitude on the magnetic field (H) dependence of resistivity (ρ) of NCMONi07 sample at T = 40 K in Fig. 4. 5. The left column shows the ρ-H isotherms measured for selected current strengths, (a) I = 100 μA, (b), 5 mA (c), 10 mA and (d) 20 mA and the figures in the right column show the corresponding change in the surface temperature of the sample(T_s). To erase the memory effect, I was reduced to zero after each field sweep and the sample was warmed up to 200 K, then cooled to 40 K without applying any current. When I = 100 μA [Fig. 4. 5(a)], during the first field sweep (0 → +7 T), $\rho(H)$ decreases gradually until $\mu_0 H$ = 2.2 T and then it decreases more rapidly with further increasing H. Then, ρ traces a different, low resistive path upon changing the field from $\mu_0 H$ = +7 T to $\mu_0 H$ = – 7 T in the second sweep. In the third sweep (μ_0H = -7 T to +7 T),

$\rho(H)$ still remains in the low resistive state, and a small hysteresis is observed. Any further field cycling retraces the same closed paths. Note that this type of a large irreversibility in the first and second field sweep and a persistent memory effect were earlier discussed in NCMONi05. The temperature of the sample, T_s increases gradually ($\Delta T \approx 1$ K) with magnetic field in both the directions of the magnetic field, which is an artifact coming from the magnetoresistance of PT100 sensor [Fig. 4. 5(e)]. The T_s does not show any irreversibility and hysteresis unlike the resistivity. Hence, the observed hysteresis is intrinsic, and is possibly related to the changes in the magnetic domain structure or domain wall nucleation upon reducing the field.

When $I = 5$ mA is applied, [see Fig. 4. 5(b)], $\rho(H)$ initially shows a sharp decrease near the origin followed by gradual decrease with further increase in H up to 1.65 T. At a critical field $\mu_0 H_C = 1.7$ T, ρ shows an avalanche behavior (a step- like decrease). The ρ-H curves in the second and third sweeps trace a low resistive path without any avalanche behavior. The sharp decrease in the resistivity near $\mu_0 H = 0$ T is accompanied by a sharp increase in the temperature of the sample from $T_s = 40$ K to 67 K as can be seen in Fig. 4. 5(f). The temperature remains nearly constant at 67 K as the field increases, until 1.65 T. Then, T_s also shows an avalanche effect, wherein the temperature of the sample abruptly drops to $T_S \approx 41$ K at $\mu_0 H = 1.7$ T, which coincides with the avalanche in the resistivity at the same field. When H is further increased from 2 T to 7 T, the T_s shows an increase of less than 1 K. The temperature does not recover to a high value but remains low and shows a memory effect similar to the $\rho(H)$ in the second and third sweeps. The field dependences of ρ (see Fig. 4. 5(c)) and T_S [see Fig. 4. 5(g)] at 10 mA are similar to 5 mA data except that the avalanche now occurs at a higher field, $\mu_0 H_C = 2.6$ T. A more spectacular effect appears in the magnetoresistance when $I = 20$ mA [Fig. 4. 5(d)]. In the first field sweep ($0 \rightarrow +7$ T) at $I = 20$ mA, ρ shows the avalanche at $\mu_0 H = 3.8$ T followed by a gradual decrease at higher fields. When H is reduced to zero, the resistivity does not remain at the low resistive persistent state unlike what was observed for $I = 10$ mA and 5 mA. Instead, it shows the avalanche effect, but

this time, a step-like increase at $\mu_0 H$ = 0.8 T. Upon reversing the field, $\rho(H)$ shows the avalanche effect again (high resistance to low resistance transition) at $\mu_0 H_C$ = -3.8 T. A similar behavior of ρ is observed in the third sweep with an abrupt increase from a low to a high resistive state at $\mu_0 H$ = –0.8 T, followed by an abrupt decrease to a low resistive state again at $\mu_0 H_C$ = 3.8 T. This, eventually results in a huge hysteresis far from the origin ($\mu_0 H$ = 0 T). The sample temperature T_s follows a similar trend. Note that the T_s decreases abruptly from 86 K to 41 K when the resistivity abruptly decreases at $\mu_0 H_C$ = 3.8 T during first field sweep [Fig. 4. 5(h)].

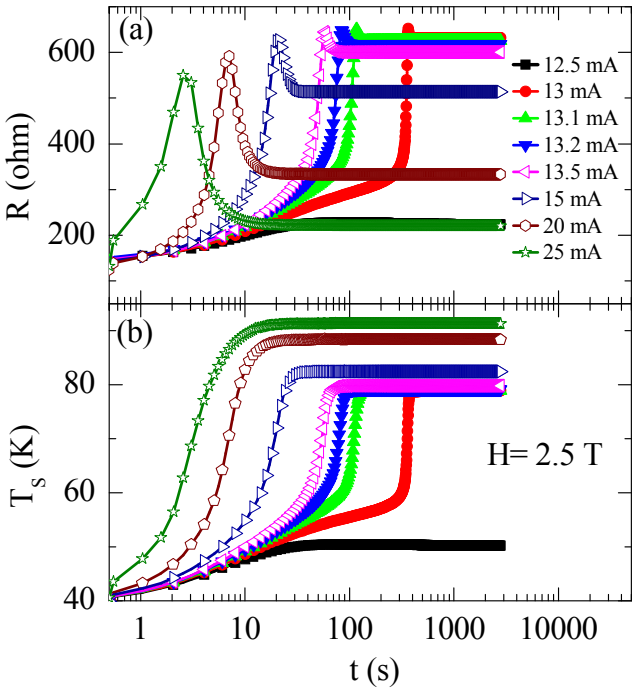

Fig. 4. 6: Time dependence of (a) resistance, *R* and (b) temperature, T_S at $\mu_0 H$ = 2.5 T and *T* = 40 K in NCMONi07 sample.

In order to confirm or rule out the possibility that the observed effect is caused by the relaxation of resistance, we have carried out the temporal dependence of the resistance and surface temperature of the sample. Fig. 4. 6(a) shows the evolution of resistance with time (t) at T = 40 K in a magnetic field, $\mu_0 H$ = 2.5 T at different current strengths. When I = 12.5 mA or lower, the R initially shows a small linear increase with the time and then becomes stable at $t \geq$ 30 s. Surprisingly, when the current is increases by a small increment of 0.5 mA, i.e.,

when I =13 mA, R increases linearly with the time up to t = 200 sec, but shows an abrupt increase around $t = t_{th}$ = 300 sec. The R shows a small peak at the end of the abrupt rise and then it quickly stabilizes. When the magnitude of the fixed current is further increased, the threshold time (t_{th}), where the abrupt increase in the resistance occurs, shifts towards a lower value of time. Note that the peak in the resistance become more prominent and it decreases in magnitude with increasing strength of the current. The temperature of the sample also undergoes an abrupt increase at a threshold time similar to the resistance as can be seen in Fig. 4. 6(b). However, after the abrupt increase above t_{th}, T_S remains constant unlike the resistance which shows a peak behavior. This study rules out the possibility that the step-like decrease in the resistance observed in the field sweep is caused by the relaxation of resistivity. An abrupt increase in the resistance with time was also noted earlier by Tokunaga *et al*. [98] in the Cr-doped $Nd_{0.5}Ca_{0.5}MnO_3$ although the temperature of the sample was not directly measured in that work.

4. 4 Discussion

The sudden increase in T_s, at the start of the field sweep ($\mu_0 H$ = 0 T) at higher current strengths is obviously caused by the Joule heating but the step- like decrease in $\rho(H)$ accompanied by an abrupt decrease in T_s in the Ni-doped compounds is unlikely due to the Joule heating effect alone. A possible explanation is that it is a manifestation of the "magnetoresistive cooling", i.e., the abrupt negative magnetoresistance at a critical value of external field causes a sudden decrease in the temperature of the sample because of the reduction in the input electric power, $P = I^2R(T,H)$ where the resistance of the sample (R) is a function of the temperature and magnetic field and I is the constant current applied to the sample. If the applied current is mainly used in heating the sample, a change in R causes the temperature of the sample to change by $\Delta T = I^2 \Delta R(T,H)/mC$, where C is the specific heat and m is the mass of the sample. First, consider the case when the Joule heating is negligible (i.e., for I < 1 mA). As the applied magnetic field increases at T = 40 K, ferromagnetic clusters initially tend to align along the field direction. However, short-range charge ordered clusters

are also progressively being converted into ferromagnetic phase which makes it difficult to identify a single critical field for the field-induced metamagnetic transition. This results in a large but smooth decrease of the resistance with increasing magnetic field. Upon decreasing *H* from the maximum value, the $\rho(H)$ traces a different path having lower resistivity values. Hence, the virgin ρ-*H* curve lies outside the envelope traced by subsequent field cycles. We have also observed a similar behavior in *M*-*H* data of NCMONi07 sample at *T* = 40 K, as exemplified in Fig. 4. 7.

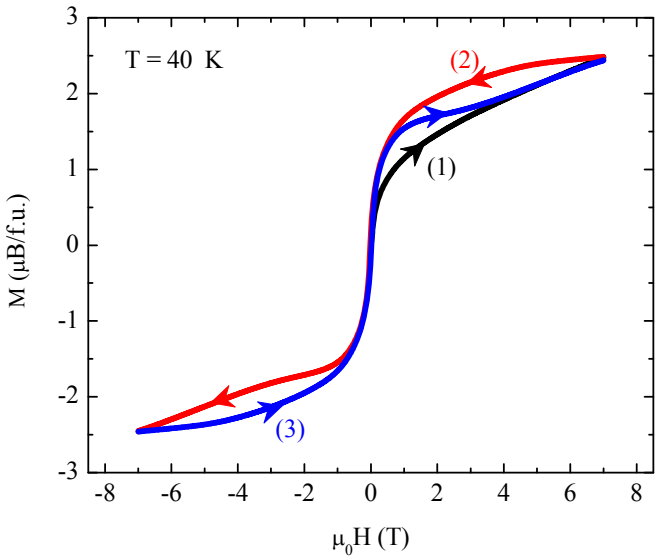

Fig. 4. 7: Magnetization (*M*) versus field (*H*) behavior of NCMONi07 sample at *T* = 40 K. Note that the virgin curve (1) lies outside the envelope traced by subsequent field cycles (2) and (3).

P. Chaddah and collaborators [87, 88, 99] have shown that this is a general phenomenon observed in materials exhibiting first-order magnetic transition such as $Nd_{0.5}Sr_{0.5}MnO_3$, Co-doped Mn_2Sb and Gd_5Si_2 although the magnetic ground states of those materials were different. In all these compounds, high temperature phase coexists with low temperature phase as a supercooled phase. In our compound, the short-range charge ordered phase (super cooled phase) is converted into ferromagnetic phase with increasing magnetic field in the initial field sweep (forward sweep) whereas the reverse conversion from ferromagnetic to charge ordered phase is sluggish (ferromagnetic phase is "kinetically arrested") during decreasing field. This results in a higher volume fraction of the

ferromagnetic phase while the field is reduced to zero and hence the magnetization is high and resistivity is low when the field is reduced to zero. Therefore the virgin loop lies outside the envelope in ρ-H and M-H measurements. While kinetic arrest of the high field phase is a dominant mechanism at temperature well below the Curie temperature, metastability of the supercooled phase can also cause similar trend (isolation of virgin curve from curves obtained in subsequent field sweep) in the temperature regime around T_C as observed in Co-doped Mn_2Sb [88]. We believe that in our sample, the kinetic arrest of the ferromagnetic phase plays an important role in the irreversibility between the virgin and subsequent field cycles in ρ-H measurements at T = 40 K. When I = 20 mA, the sample is Joule heated non-uniformly, thus leading to a partial conversion of the low-temperature ferromagnetic phase into the high temperature short-range charge ordered phase. Hence, phase fraction of the short-range charge ordered phase is increased relative to the ferromagnetic phase. As the magnetic field strength increases, the dc resistivity of the ferromagnetic phase decreases at a faster rate than the charge ordered phase. The lowering of the resistivity due to magnetic field leads to nucleation of cold spots in the ferromagnetic phase which have lower temperatures than the surrounding charge ordered matrix ("hot matrix"). The size of cold spots grows with increasing strength of the magnetic field and for a critical value of H- field, they will engulf the hot matrix, thus leading to an avalanche like decrease in the resistance and temperature. Chen *et al*. [77] also reported a qualitatively similar step-like decrease of the resistance in thin film of $La_{0.8}Ca_{0.2}MnO_3$, though the step was not as sharp as in our compound. They have used high current (I = 20 -70 mA) to drive the sample into paramagnetic phase while the measurements were done below but close to the Curie temperature. On the other hand, Yamato *et al*. [100] reported that step in magnetoresistance at T = 5 K becomes broader with increasing current strength in a single crystalline bilayered manganite whereas the magnetoresistance step in our sample becomes sharper with increasing current strength. They estimated that the temperature of the sample would not have increased more than 1.8 K at 5mA.

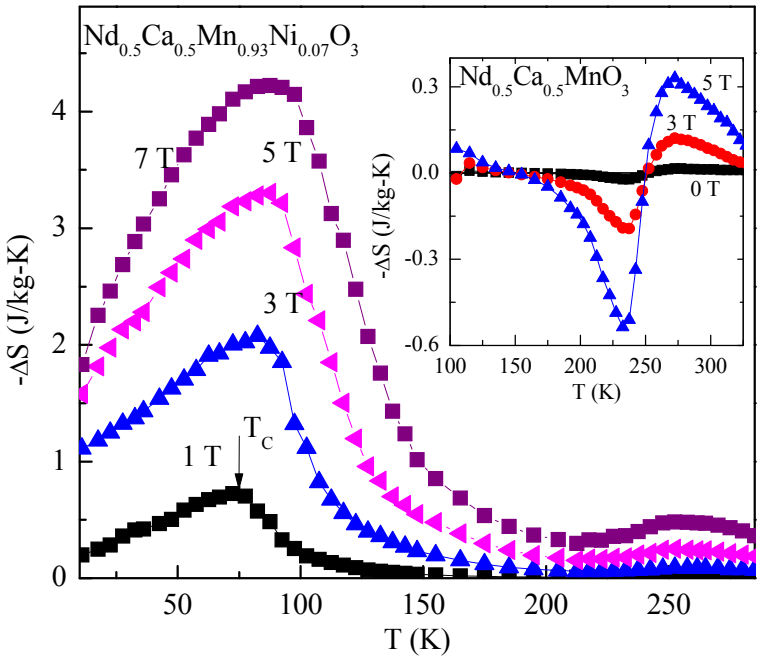

Fig. 4. 8: The main panel shows temperature dependence of the magnetic entropy change ($-\Delta S_m$) for different magnetic field intervals (ΔH = 1, 3, 5 and 7 T) for $Nd_{0.5}Ca_{0.5}Mn_{0.93}Ni_{0.07}O_3$. The inset shows $-\Delta S_m$ versus T for $Nd_{0.5}Ca_{0.5}MnO_3$.

In Fig. 4. 8, we have plotted the magnetic entropy (ΔS_m) of the 7 % Ni-doped compound, as calculated from magnetization isotherms taken at 5 K intervals from 300 K to 10 K (please see chapter 2 for details on calculation). The magnitude of ΔS_m is negative over the entire temperature range and shows a prominent maximum (ΔS_m = 4.2 J/kgK) for ΔH = 7 T around T_C (77 K) followed by a broad maximum of smaller magnitude (ΔS_m = 0.5 J/kgK) around the short-range charge ordering temperature (T_{CO} = 252 K). The magnitude of ΔS_m decreases with decreasing strength of the field. On the other hand, the parent compound $Nd_{0.5}Ca_{0.5}MnO_3$, shows a negative peak in ΔS_m at a few K above T_{CO}, but changes into a positive peak at a few K below T_{CO} (see the inset). A similar change in the sign of ΔS_m with temperature for a few charge ordered compositions in the $Pr_{1-x}Ca_xMnO_3$ series was also reported earlier by Reis *et al.* [101]. The negative ΔS_m observed over the entire temperature range in the present Ni-doped compound indicates that the lattice temperature of the sample will increase (decrease) upon adiabatic application (removal) of an external magnetic field similar to a normal ferromagnetic material. However, it alone will not account for the step-

like decrease in the temperature observed at a critical value of the magnetic field in our compound.

The observed abrupt decrease in temperature is opposite to the intrinsic magnetocaloric effect found in other phase separated manganites. Ghivelder *et al*. [102] showed that magnetoresistance avalanche in the phase separated $La_{0.225}Pr_{0.40}Ca_{0.375}MnO_3$ was accompanied by a sudden increase in temperature of the sample from 2.5 K to about 30 K at a critical value of the magnetic field. The temperature quickly relaxed to the initial temperature within a few milli seconds. The abrupt increase in the temperature of the sample was attributed to intrinsic magnetocaloric effect, i.e., heat released in the conversion of charge ordered antiferromagnetic phase into ferromagnetic phase at a critical value of the external magnetic field. The heat released $\delta q = \int_{T_0}^{T_f} c_p dT = u_{CO}(T_0) - u_{FM}(T_0, H)$ depends on the differences in the internal energy per unit volume of the charge ordered phase ($u_{CO}(T_0)$) initially at temperature T_0 and the ferromagnetic phase ($u_{FM}(T_0,H)$). The heat released by the charge ordered clusters during the conversion into ferromagnetic clusters ignites instability of the neighboring charge ordered clusters. In what follows as a chain reaction, heat wave propagates through the sample volume and the sample temperature rises rapidly. Roy *et al*. [103] also reported that the magnetic field induced destruction of charge ordered antiferromagnetic state in $Pr_{0.7}Ca_{0.3}MnO_3$ leads to release of the heat and hence increase in temperature of the sample due to the intrinsic magnetocaloric effect. However, we find that temperature of the sample decreases abruptly in our compound, which suggests that the observed effect is not necessarily caused by the magnetocaloric effect.

The magnetoresistance avalanche accompanied by large changes in the surface temperature can be due to the current induced phase separation in the sample. At higher current strengths, for instance at I = 20 mA, sufficient Joule heating of the sample partially transforms the low-temperature FMM phases into the high temperature COI phase. The growing presence of the COI domains results in an increase in the resistivity of the sample

and therefore $\rho(H)$ shows a high resistance plateau at low magnetic fields. As the field reaches H_C, melting of the charge ordered state in the phase separated system leads to a rapid decrease in resistivity and inturn leads to abrupt changes in T_S because of the reduction in the input electric power. The temperature of the sample changes by $\Delta T = I^2 \Delta R(T,H)/mC$, where C is the specific heat and m is the mass of the sample. Due to the competing large presence of COI domains at higher current strengths, larger magnetic fields are required for the collapse of the charge ordered domains and therefore, H_C gets shifted upward in H with increasing I [Fig. 4.5]. The hysteresis observed in $\rho(H)$ indicates the first order nature of the field induced transition between different phase fractions. On the other hand, the flow of a high dc current in the sample transverse to the magnetic field can also create temperature gradient transverse to the direction of current (Ettingshausen effect [104]) or along the direction of current (magneto-Peltier effect [105]). A systematic study is urgently needed to address the exact origin of the observed avalanche effects in resistance and temperature.

4. 5 Conclusions

In summary, we have discussed the magnetic field dependence of magnetoresistance, in the phase separated Ni doped (5 % and 7 %) NCMO samples, which exhibit an avalanche with increasing magnitude of the dc current. A temperature change of $\Delta T \approx 47$ K was found to accompany the avalanche in the magnetoresistance. Our results show that the effect of the dc current on the magnetoresistance is more intriguing than what is anticipated. Though our results indicate a strong interplay between magnetoresistance and thermal behavior, the mechanism of the coupling is not clear at present and further work is in progress to understand the observed effects.

Chapter 5

Magnetocaloric effect in $Sm_{1-x}Sr_xMnO_3$ (x= 0.3-0.5)

5. 1 Introduction

Manganites exhibit a wide variety of properties owing to a strong coupling between spin, charge and lattice degrees of freedom. Besides large resistive responses under different external stimuli, manganites also join the race for a large magnetocaloric effect (MCE) following the reports of large MCE in $La_{0.75}Sr_{0.25-y}Ca_yMnO_3$ (y= 0.1) [106] and related compounds [107, 108]. The MCE is expected to be much larger in compounds that show a temperature driven first-order paramagnetic to ferromagnetic transition in which M changes discontinuously at T_C [109]. In these compounds, an external magnetic field can trigger metamagnetic transition in the paramagnetic state ($T \geq T_C$) which leads to a giant MCE as reported recently in $Gd_5Si_2Ge_2$ [110], $MnFeP_{0.45}As_{0.55}$ [111], and Ni_2MnGa [112].

In this chapter, we demonstrate an alternative approach to achieve a large MCE by exploiting the nanoscale phase separation found in some narrow band width manganites. We have investigated magnetocaloric effect in $Sm_{1-x}Sr_xMnO_3$ series (x= 0.3, 0.4, and 0.5) whose magnetic phase diagram has been studied in detail [113,114]. The low temperature ground state of $Sm_{1-x}Sr_xMnO_3$ is reported to change from a metallic ferromagnet ($0.35 \leq x < 0.5$) to a semiconducting A-type antiferromagnet ($x \geq 0.5$) [115]. In the critical composition x= 0.5 where $T_C = T_N$ (T_N-Neel temperature), a long-range charge-orbital ordering also develops below T_N. The paramagnetic phase of these Sm based manganites is unusual as suggested by the early work of Borges *et al*. [116]. Those authors reported a field-induced metamagnetic transition, i.e., a rapid increase of the magnetization above a threshold magnetic field in the paramagnetic state and a large deviation of the inverse susceptibility much above T_C. Small Angle Neutron Scattering (SANS) study in $Sm_{0.55}Sr_{0.45}MnO_3$ by J.M. De Teresa *et al*. [117] supported the presence of ferromagnetic nano clusters of size ≈ 0.8 nm and stable longer than

~1 ps in zero field. A strong diffusive x-ray scattering below 300 K (> T_C= 118 K) in x= 0.45 was reported earlier and it was attributed to the short-range charge-orbital clusters [24, 118]. Thus, it seems that the paramagnetic state of x= 0.45 has a mixture of short-range charge ordered regions and nanometer size ferromagnetic clusters. However, MCE in these materials has not been studied in detail. In the course of our investigation of Sm based compounds, we came across the recent work by Sarkar *et al.* [119] who observed a huge change in magnetic entropy -ΔS_m= 7.9 J/kg-K in $\mu_0 H$= 1 T at T= 120 K in a single crystal of x = 0.52. According to the recently proposed phase diagram, x= 0.52 composition is A-type antiferromagnetic below T_N=120 K [115]. In this report, we focus on the magnetic and magnetocaloric effects in lower compositions, x= 0.3, 0.4, and 0.5.

5. 2 Experimental Section

Polycrystalline samples of $Sm_{1-x}Sr_xMnO_3$ (SSMO) series were synthesized using standard solid state route. The precursors Sm_2O_3, $SrCO_3$ and MnO_2 (each of purity better than 99.9%) were mixed in proper stoichiometric composition, ground and then preheated at 1273 K for 24 h. The mixture thus obtained was reground, pelletized and sintered at 1473K for 24 h. Single phase identification was performed by the powder X-ray diffraction (XRD) experiment. Magnetic measurements over a wide temperature (T= 10 - 400 K) and magnetic-field ($\mu_0 H$= 0 - 5 T) range were carried out on the samples using a vibrating sample magnetometer probe in a commercial superconducting PPMS cryostat. Magnetocaloric properties were investigated by calculating the magnetic entropy change from the experimental magnetization versus field isotherms, as explained in chapter 2.

5. 3 Results and Discussion

Fig. 5. 1 shows the XRD patterns of the $Sm_{1-x}Sr_xMnO_3$ (SSMO) compounds (x= 0.3, 0.4 and 0.5) at room temperature, which reveal single phase patterns. The observed XRD patterns were indexed to orthorhombic structure of SSMO with space group *Pbnm*. The prominent peaks in the XRD pattern are indexed by its crystallographic planes, as represented by the miller indices (*hkl*) in accordance with Ref. 120.

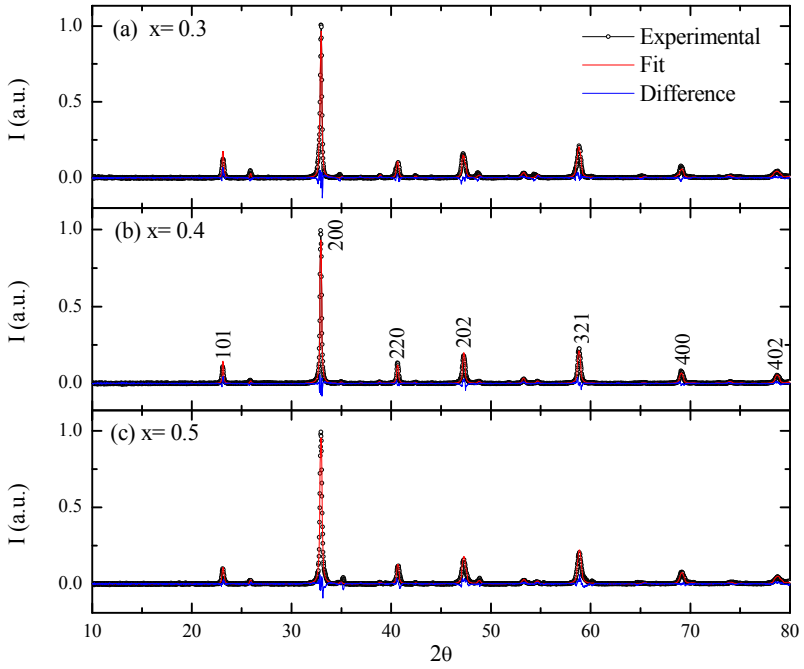

Fig. 5. 1: XRD pattern for $Sm_{1-x}Sr_xMnO_3$, x = 0.3, 0.4 and 0.5

Fig. 5. 2 shows the temperature dependence of the magnetization $M(T)$ at $\mu_0 H$ = 0.1 and 5 T, for (a) x= 0.3, (b) x= 0.4 and (c) x= 0.5 samples. The *M-T* data at $\mu_0 H$ = 0.1 T suggest that all these compounds undergo a paramagnetic to ferromagnetic transition upon cooling and exhibit a small hysteresis around the transition temperature while warming. The Curie temperature (T_C) identified from the inflection point of the derivatives of *M-T* curves while cooling are T_C= 87 K, 118 K and 99 K for x= 0.3, 0.4 and 0.5 respectively. The magnetic transition is rather sharp in the case of x= 0.4 compared to the other two compositions. The x= 0.4 also shows a clear peak around T= 30 K << T_C possibly related to increase in the coercivity [116,121]. From the indirect susceptibility measurements, we also

observed an increase in the anisotropic field H_A below 30 K, the data is not shown here. While the magnetic transition is more broadened under $\mu_0 H$= 5 T for x= 0.3, the x= 0.4 composition shows a clear upward shift of the T_C to 157 K. The temperature dependence of the inverse susceptibility ($1/\chi$) for all the composition are shown in the respective insets along with the Curie-Weiss fit ($1/\chi = C/(T-\theta_p)$) drawn in red line. The $1/\chi$ clearly deviates from the Curie-Weiss behavior several tens of kelvin above the T_C for all the compositions. The x= 0.4 shows the strongest deviation, which starts around 310 K, far above T_C= 118 K. The observed effective moments P_{eff} = 5.88, 5.8 and 5.22 μ_B are much larger than theoretically expected values (P_{th} = 4.61, 4.51, and 4.44 μ_B for x= 0.3, 0.4 and 0.5, respectively) assuming P_{eff} (Sm^{3+})= 0.71 μ_B. Borges *et al*. [116] found a much larger P_{eff}= 19 μ_B in x= 0.35 when $1/\chi$ vs. T data was extended up to 600 K.

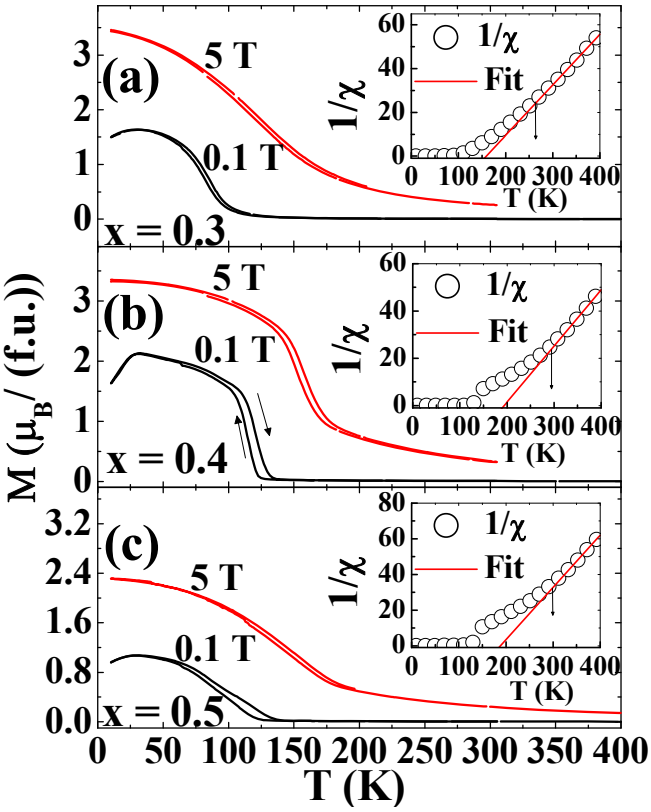

Fig. 5. 2: Temperature dependence of the magnetization of the $Sm_{1-x}Sr_xMnO_3$ (a) x= 0.3, (b) x= 0.4 and (c) x= 0.5 at magnetic field of $\mu_0 H$= 0.1 T (black line) and 5 T (red line).

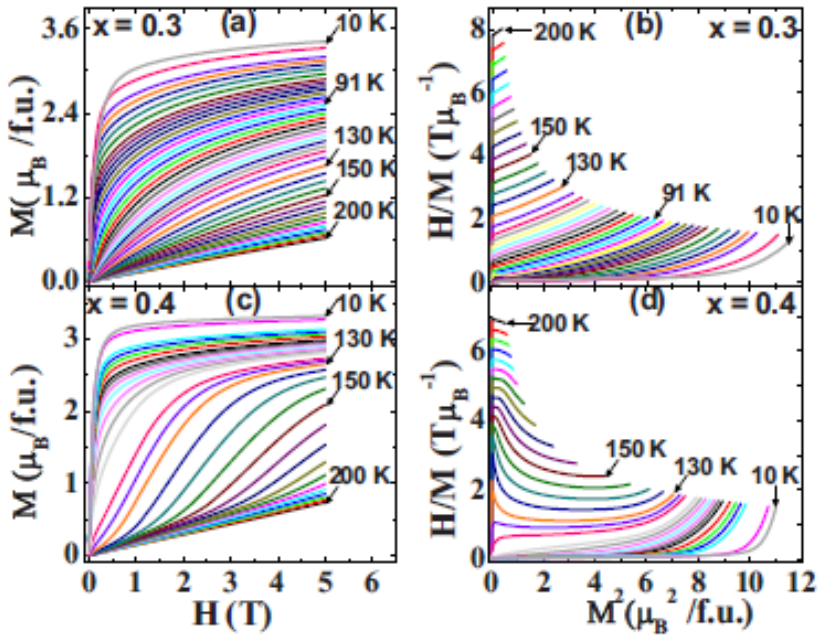

Fig. 5. 3: (a) *M-H* isotherms and (b) Arrott plot for the composition x = 0.3. The bottom panels show the respective plots for x = 0.4. *M-H* isotherms were taken at a temperature interval of ΔT = 3 K interval in between 130 K and 90 K, i.e. in the regime of magnetic phase transition and at ΔT = 5 K at other temperatures.

Fig. 5. 3(a) shows the magnetization (M) isotherms at different temperatures and Fig. 5. 3(b) shows H/M versus M^2 (Arrott plot) for x= 0.3. We have taken magnetization isotherms at temperature interval of ΔT = 3 K between 130 K and 60 K and at ΔT= 5 K in other temperature ranges. The M varies linearly with H above 180 K in the paramagnetic state but shows a Langevin- type superparamagnetic behavior (gradual reorientation of superparamagnetic moment towards the field direction with increasing field strength) between 180 K and 100 K. Below 80 K, the sample is a soft ferromagnet with a rapid increase at fields less than 0.1 T followed by a slow approach to saturation at high fields. The saturation magnetization obtained from the extrapolation of the high field magnetization to the origin ($\mu_0 H$= 0 T) is M_{sat}= 3.5 μ_B which is closer to the theoretical value of 3.7 μ_B. The Arrott plot shows a positive slope near the Curie temperature suggesting that the transition is second-order according to the Banarjee's criteria [122]. In contrast to x= 0.3, $M(H)$ of x= 0.4 [Fig. 5. 3 (c)] shows a metamagnetic behavior– a rapid increase above a critical field (H_c) in the paramagnetic state between 170 K and 125 K though it is linear above 180 K. The transition

from low- to high magnetic moment state is reversible upon decreasing the field with small hysteresis of width (0.01 T) at 135 K (not shown here). The critical field decreases with lowering temperature, from $\mu_0 H_c$= 3.9 T at 170 K to $\mu_0 H_c$= 0.4 T at 127 K. The saturation magnetization at 10 K reaches a value of 3.25 μ_B which is slightly lower than 3.6 μ_B expected theoretically. The Arrott plot [Fig. 5. 3 (d)] shows a negative slope at temperature above and near T_c which suggests that the field-induced para-ferromagnetic transition is first-order. This satisfies one of the criteria proposed for a material to be a good magnetocaloric material around the Curie temperature [123].

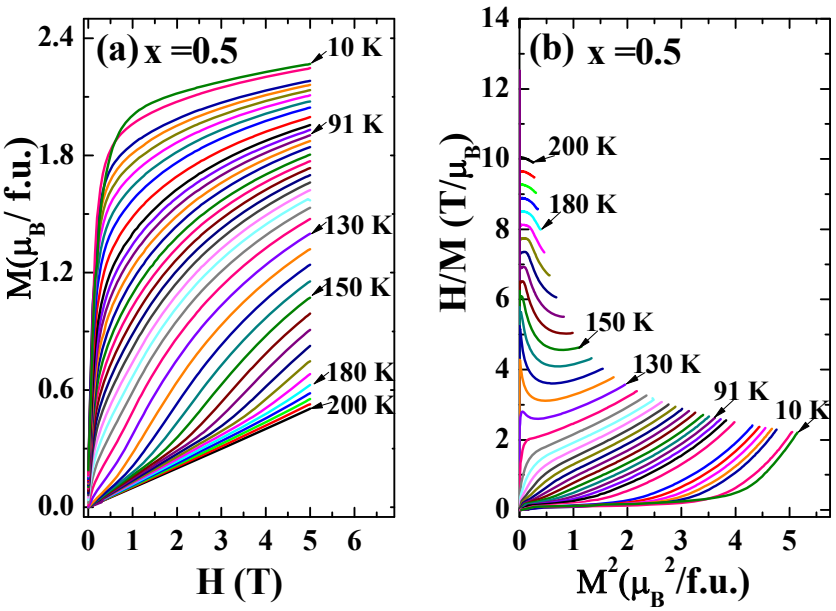

Fig. 5. 4: (a) *M-H* isotherms and (b) Arrott plot for the composition x = 0.5. The data were taken at ΔT = 3 K interval in between 130 K and 100 K and at ΔT = 5 K interval away from the phase transition.

The *M-H* curves and the Arrott plot for x= 0.5 is shown in Fig. 5. 4(a) and Fig. 5. 4(b), respectively. This sample also shows a metamagnetic behavior in the *M-H* curve between 180 K and 125 K but the transition is rather broad compared to x= 0.4. A ferromagnetic like *M-H* behavior is observed below 90 K. It is to be noted that the extrapolation of high-field data to the origin, gives M_s= 1.88 μ_B which is far below expected theoretical value, 3.5 μ_B (even at the highest field used). The Arrott plot exhibits a negative

slope for certain field range above 125 K which suggests the field-induced transition is first order in nature.

Since materials with low hysteresis loss is preferred for the application prospects, we compare the hysteresis in *M-H* during increasing and decreasing strength of the magnetic field for all three compositions at *T*= 135 K [Fig. 5. 5(b)]. It is seen that the x= 0.4 composition exhibits a small hysteresis but the other two compounds show negligible hysteresis. The width of the hysteresis in x= 0.4 is temperature dependent: it increases with lowering temperature below 160 K down to 120 K and then decreases as shown in Fig. 5. 5(a). The other two compositions did not show hysteresis at all temperatures. The variation in the critical field H_c which corresponds to the onset of metamagnetic transition (determined from the intersection point of the linear increase of *M* at low magnetic fields and the rapid increase at the intermediate fields) with temperature is plotted in inset of Fig. 5. 5(b).

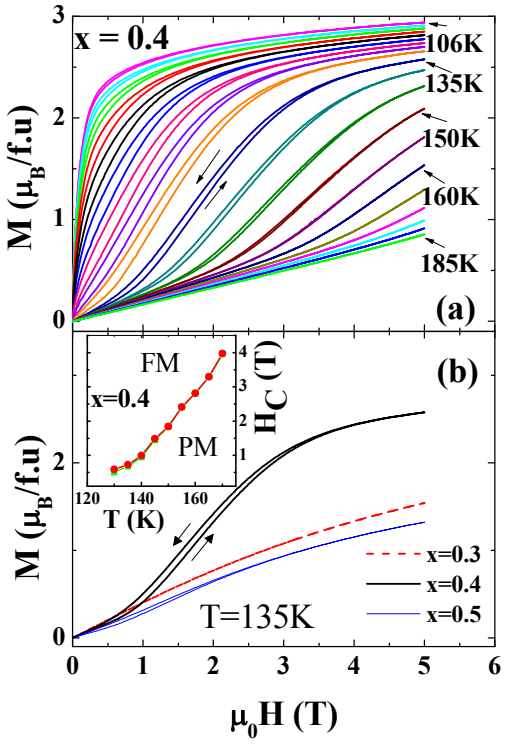

Fig. 5. 5: (a) *M-H* isotherms ($\mu_0 H$ = 0 T- 5 T- 0 T) for the composition x = 0.4 and (b) *M-H* curve ($\mu_0 H$ = 0 T- 5 T- 0 T) at 135 K for x = 0.3, 0.4 and 0.5. The inset shows the variation of H_c with temperature.

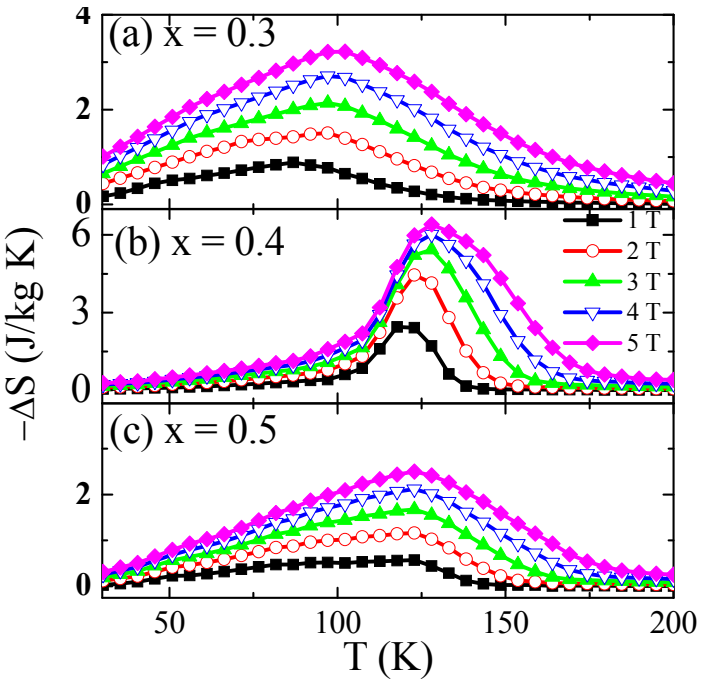

Fig. 5. 6: The temperature dependence of the change in the magnetic entropy ΔS_m at different magnetic fields for x = (a) 0.3, (b) 0.4, and (c) 0.5.

The entropy change associated with the magnetic field variation, calculated from the *M-H* curve at various fixed temperatures, is plotted in Fig. 5. 6(a), Fig. 5. 6(b) and Fig. 5. 6 (c) for the three compositions x= 0.3, 0.4 and 0.5 respectively. For x= 0.3, ΔS_m at $\mu_0 H$= 1 T shows a broad maximum around T_C= 87 K with a maximum value of $-\Delta S_m$= 0.85 J/kg K and the maximum shift to 97 K at 3 T. Though the magnitude of ΔS_m increases with H, the temperature corresponding to the maximum remains nearly the same at $\mu_0 H$ = 5 T. The ΔS_m of x= 0.4 [Fig. 5. 6 (b)] exhibits a rather prominent peak compared to other two compounds. The peak shifts from 117 K at $\mu_0 H$= 1 T to 127 K at $\mu_0 H$= 5 T. Interestingly, this composition shows the largest entropy change $-\Delta S_m$= 6.2 J/kg K at $\mu_0 H$= 5 T and T= 127 K followed by ΔS_m= 3.3 J/kg K at 97 K for x= 0.3 [Fig. 5. 6 (a)] and ΔS_m= 2.3 J/kg K at 125 K for x= 0.5 [Fig. 5. 6 (c)]. The ΔS_m of x= 0.4, unlike the other two compounds, exhibits a sharp drop just below the peak values for each magnetic field and it weakly depends on the field for T < 50 K. The x = 0.3 and 0.5 samples show a field dependent entropy over a wide temperature range below the maximum compared to x= 0.4. Based on the only heat capacity data available for x= 0.48(C_p ≈150 J/mol K at $\mu_0 H$= 0 T) [119], we estimate the lower limit for the adiabatic

temperature change to be $\Delta T_{ad} = T\Delta S/C_p \approx$ 1.2 K at T_c =127 K and $\mu_0 H$= 5 T for x= 0.4. Note that C_p can decrease under the magnetic field and hence ΔT_{ad} can increase. The relative cooling power (RCP), a measure of heat transferred by a magnetic refrigerant, is obtained by the product of the peak value of the entropy (ΔS_m^{peak}) and the full width at half maximum ($\delta T_{FWHM,}$), i.e., $RCP(T,\Delta H) = \Delta S_m\ (T,\Delta H)\ \delta T_{FWHM}$. The larger the δT_{FWHM}, the better is the cooling-capacity. The *RCP* of x= 0.3 (-326.3J/Kg) is higher than x= 0.4 (- 269.5 J/Kg) and x= 0.5 (-231 J/Kg) at 5 T.

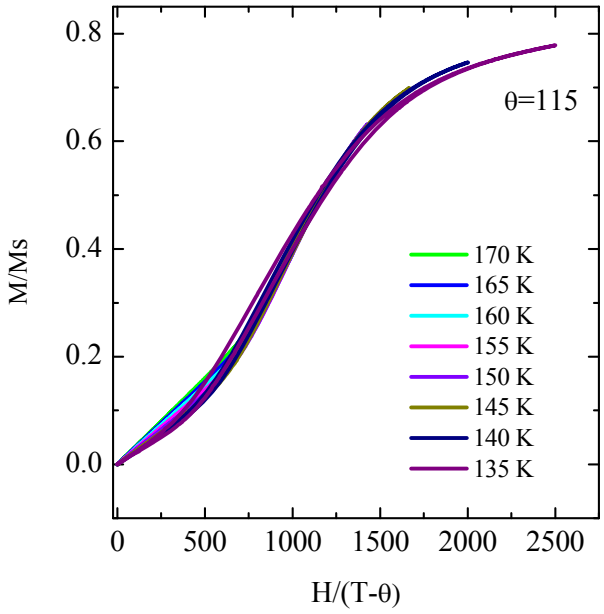

Fig. 5. 7: M/M_s vs. $H/(T-\theta)$ scaling in x= 0.4

The largest ΔS_m observed in x= 0.4 is clearly related to the field-driven metamagnetic transition occurring in the paramagnetic state. The large deviation of the inverse susceptibility $1/\chi$ much above T_C (= 118 K) found in this compound suggests existence of superparamagnetic clusters in the paramagnetic state. Jacobs and Bean [124] put forward an operational definition of superparamagnetism, which include at least two requirements. First the magnetization curves should have negligible hysteresis and second for a non-interacting and isotropic system, the magnetization curves must be temperature dependent on the extent that curves taken at different temperatures must superimpose when plotted against H/T. Our

analysis of *M-H* data at different temperatures above T_C does not scale to M/M_s vs. $\mu B/k_BT$ as expected for non-interacting superparamagnetic clusters but to M/M_s vs. $\mu B/k_B(T-\theta)$ where θ is measure of interaction between clusters, as illustrated in Fig. 5. 7. It is evident from the figure that magnetic behavior of $Sm_{0.6}Sr_{0.4}MnO_3$ at temperatures above 130 K, where a superposition is seen is indicative of a superparamagnetic behavior. If the size of the ferromagnetic particles is sufficiently small, the ordered state will have a single domain in which Mn^{3+} and Mn^{4+} spins are aligned in the same direction across the volume of the particle. The net magnetization of such an assembly of particles can be highly sensitive to temperature. As long as the thermal energy remains smaller than the magnetic anisotropic energy, the saturation magnetization will be same as that of the bulk sample. Above a critical temperature known as the blocking temperature, the thermal energy becomes sufficiently large to cause a Brownian rotation of the magnetization in the particles. The net moment of the sample in the presence of a field is then given by a Boltzmann distribution of individual moments in the field direction just as in the case of a paramagnet. The average fraction of magnetization or moment in the direction of field is given by the Langevin function following a simple classical mean free model [125]:

$$\frac{M}{M_S} = L(\alpha) \text{ with}$$

$$L(\alpha) = \coth(\alpha) - 1/\alpha \text{ and}$$

$$\alpha = \frac{\mu H}{k_B T} + 3\frac{T_C}{T}\frac{M}{M_S}.$$

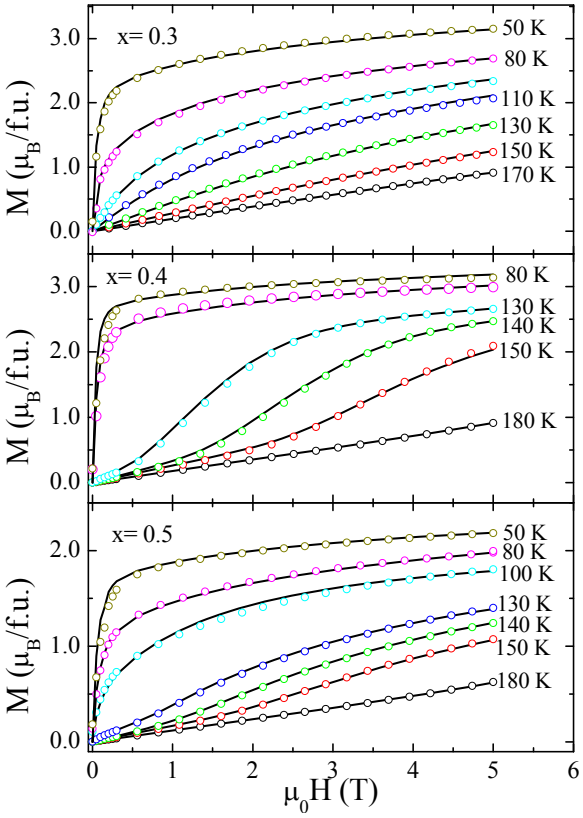

Fig. 5. 8: Experimental (symbols) *M-H* curves and theoretical Langevin fit (solid lines) for (a) x= 0.3, (b) x= 0.4, and (c) x= 0.5 at different temperatures.

In this model, three independent parameters used are: M_S, the mean-field saturation moment, T_C, the mean-field Curie temperature and μ/μ_B, the mean-field magnetic moment associated with the strength of individual magnetic cluster. The experimental and theoretical curves are shown in Fig. 5. 8 for the above discussed three compositions. Small angle neutron scattering study in x= 0.45 suggested ferromagnetic clusters of ≈ 0.8 nm size imbedded in short-range charge/orbital ordered paramagnetic matrix [117]. These nanometer size clusters are weakly interacting in low magnetic fields but as the applied magnetic field increases, interaction between ferromagnetic nano clusters increases. Above a critical field (H_C), the size of the clusters increases abruptly and eventually they coalesce at higher fields. Thus, microscopically inhomogeneous paramagnetic state transforms into homogeneous ferromagnetic phase at higher fields. This process leads to the rapid increase of the magnetization above H_C as observed in the M versus H data for x= 0.4 that results in the largest change in the magnetic entropy. However, the observed value of $-\Delta S_m$= 2 J/kg K at

$\mu_0 H$= 1 T is a factor of 2 smaller than the value reported in single crystalline [119] $Sm_{0.52}Sr_{0.48}MnO_3$ and it is possibly due to smearing of the metamagnetic transition by disorders such as grain boundaries in polycrystalline sample. The values of entropy change for some magnetic refrigeration materials are tabulated in Table 5. 1. The *M-H* curve in our polycrystalline compounds exhibits much smaller hysteresis which is preferred for magnetic refrigeration compared to single crystals that show a sharp metamagnetic transition but with pronounced hysteresis [115]. The magnetization of x= 0.5 even at 5 T is 2.5 μ_B is lower than the value (= 3.5 μ_B/f.u) expected for complete parallel alignment of Mn spins. It suggests the low temperature ground state of x= 0.5 is different from that of x= 0.4 and it is possibly an inhomogeneous mixture of ferromagnetic and antiferromagnetic clusters. Indeed, single crystalline study shows that the low temperature ground state changes from ferromagnetic to A-type antiferromagnetic at x= 0.5 and in this critical composition both T_C and T_N may coincide and long range charge-ordering also develops below 80 K [114]. The decrease in the field-induced magnetic entropy in this composition can be attributed to the existence of stronger charge-orbital correlation above T_C.

No	Composition	Curie temperature T_C (K)	Magnetic field $\mu_0 H_{max}$ (T)	Entropy change $\lvert\Delta S_M (T_C)\rvert$ (J/kg-K)	Ref.
1	$La_{0.67}Ca_{0.33}MnO_3$	250	5	2.1	126
2	$La_{0.67}Ba_{0.33}MnO_3$	295	5	1.3	126
3	$La_{0.67}Sr_{0.33}MnO_3$	345	5	1.7	126
4	$La_{0.67}Ca_{0.33}MnO_3$	258	3	2.6	127
5	$La_{0.6}Y_{0.07}Ca_{0.33}MnO_3$	230	3	1.5	127
6	$La_{2/3}Ca_{1/3}MnO_3$	267	3	6.4	128
7	$La_{0.6}Ca_{0.4}MnO_3$	263	3	5	107
8	$Gd_{0.73}Dy_{0.27}$	265	10	10	129
9	$Gd_5(Si_2Ge_2)$	300	5	7	130
10	$Gd_5(Si_2Ge_2)$ (~99.8 at% pure Gd)	276	2	14	110
11	$La_{0.67}Sr_{0.33}Mn_{0.9}Cr_{0.1}O_3$	328	5	5.1	131
12	$Sm_{0.6}Sr_{0.4}MnO_3$	118	5	6.2	This work
13	$Sm_{0.52}Sr_{0.48}MnO_3$	113	4	6.3	119
14	$La_{0.65}Bi_{0.05}Sr_{0.3}MnO_3$	353	5	5.02	132

Table 5. 1: Maximum entropy change ($-\Delta S_M$) occurring around T_C for several magnetic refrigerants.

5 . 4 Conclusions

In summary, we have studied magnetic and magnetocaloric properties in $Sm_{1-x}Sr_xMnO_3$ (x = 0.3, 0.4, and 0.5) and found the largest magnetocaloric effect in x = 0.4 among the three compositions. The largest MCE observed in x = 0.4 is related to the existence of ferromagnetic nano clusters in the paramagnetic state that grow and coalesce with increasing strength of the external magnetic field. Our results suggest that other manganites that show a field-induced metamagnetic transition in the paramagnetic state such as Cr or Ni doped $Pr_{0.5}Ca_{0.5}MnO_3$ [133] or lower band width manganites such as $Eu_{1-x}Sr_xMnO_3$ [134] may be attractive candidates to look for a large magnetocaloric effect.

Chapter 6

Colossal electroresistance in $Sm_{1-x}Sr_xMnO_3$ (x= 0.4 and 0.5)

6. 1 Introduction

In this chapter, we investigate the effect of dc current on the temperature dependence of electroresistance in $Sm_{1-x}Sr_xMnO_3$ (x= 0.4 and 0.5). The Sm based manganites are quite interesting because there are evidences for presence of short range charge ordering [118] as well as ferromagnetic clusters [117] above T_C. However, there is no earlier report on the effect of dc current on electrical resistivity in this series and it is the motivation of the present work. In chapter 3, it is discussed that the light Ni doping at the Mn site induces a insulator-metal transition (I-M) in an otherwise insulating parent compound $Nd_{0.5}Ca_{0.5}MnO_3$. Here we present the investigation of electroresistance in $Sm_{0.6}Sr_{0.4}MnO_3$ and $Sm_{0.5}Sr_{0.5}MnO_3$. The former compound shows a prominent I-M transition due to the collapse of charge ordering at T_C, even without Mn-site doping. It is shown that with increasing magnitude of current (I), I-M transition in $Sm_{0.6}Sr_{0.4}MnO_3$ becomes discontinuous and shifts down in temperature. An abrupt decrease in temperature of the sample was found to accompany the abrupt I-M transition.

6. 2 Experimental Section

We have simultaneously measured the four probe resistivity of rectangular $Sm_{0.6}Sr_{0.4}MnO_3$ sample of dimensions 10x3x3 mm^3 and surface temperature of the sample in the electroresistance studies. The samples were prepared using standard solid state route, as described in chapter 5. The details of the experimental set up are discussed in chapter 2. The temperature of the sample measured by the Pt-sensor is denoted as T_S and the temperature recorded by the cryostat is denoted as the base temperature T throughout this chapter.

6. 3 Results

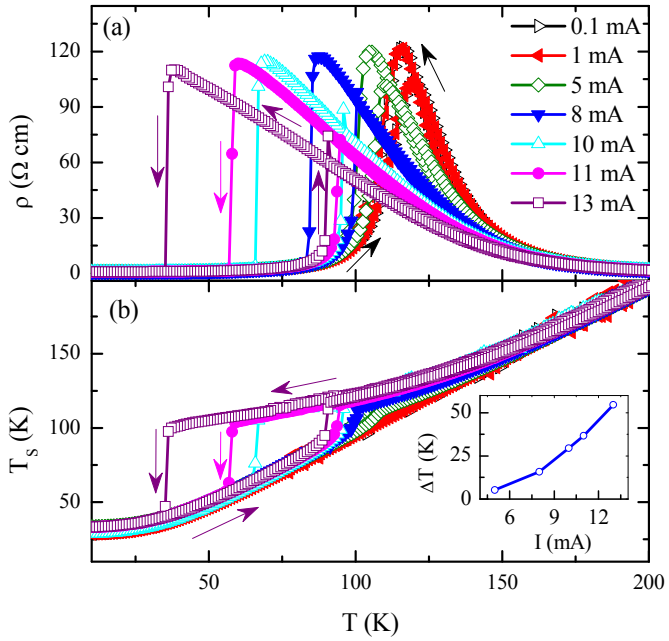

Fig. 6. 1: Temperature (*T*) dependence of the (a) resistivity (ρ) of SS40MO sample for different dc current strengths (*I*) in zero magnetic field and (b) corresponding sample temperature (T_S). The inset shows the difference $\Delta T = T_{IM}$-T_{MI} as a function of current.

Motivated by the electroresistance results in the phase separated Ni doped NCMO samples (please see chapter 3), we have carried out studies on current induced effects on the resistivity in $Sm_{0.6}Sr_{0.4}MnO_3$ (SS40MO) which also exhibits an I-M transition. Fig. 6. 1(a) shows the temperature (*T*) dependence of the dc resistivity (ρ), for different values of the dc current (*I* = 0.1 mA to 13 mA). The $\rho(T)$ for both *I* = 0.1 mA and 1 mA closely overlap on each other and show a smooth insulator-metal (I-M) transition with a peak in $\rho(T)$ occurring around T_{IM} = 115 K while cooling. The I-M transition for *I* = 0.1 and 1 mA is weakly hysteretic while cooling and warming. However, T_{IM} shifts to lower temperature and the transition to the metallic state becomes discontinuous upon increasing the amplitude of the current. The transition is first-order in nature as suggested by the hysteresis while cooling and warming. For example, $\rho(T)$ for *I* = 13 mA, upon cooling from 200 K, shows a discontinuous decrease at T_{IM} = 39 K and then continues to decrease gradually with further lowering temperature. Upon warming, a reverse transition from the metallic to the insulating behavior

(M-I) takes place discontinuously around T_{MI} =90 K. While the value of resistivity for $I > 5$ mA is lower than for $I < 1$ mA below 160 K, the peak value of the resistivity just before the discontinuous jump is not severely affected by the amplitude of the current except for $I = 13$ mA. Surprisingly, the discontinuous I-M transition is also accompanied by a discontinuous decrease in the temperature of the sample (T_S) as shown in Fig. 6. 1(b). Here, the surface temperature of the sample (T_S) is plotted against the base temperature of the sample puck (T) which is generally measured in the Physical Property Measuring System. It can be noted that $T_S > T$ before the discontinuous decrease takes place for higher current strengths. As the amplitude of I decreases, the discontinuity in the temperature also decreases and finally, both T_S and T closely match for $I = 0.1$ mA and 1 mA. The width of the hysteresis $\Delta T = T_{IM} - T_{MI}$ increases with increasing value of the current, as shown in the inset of Fig. 6. 1(b).

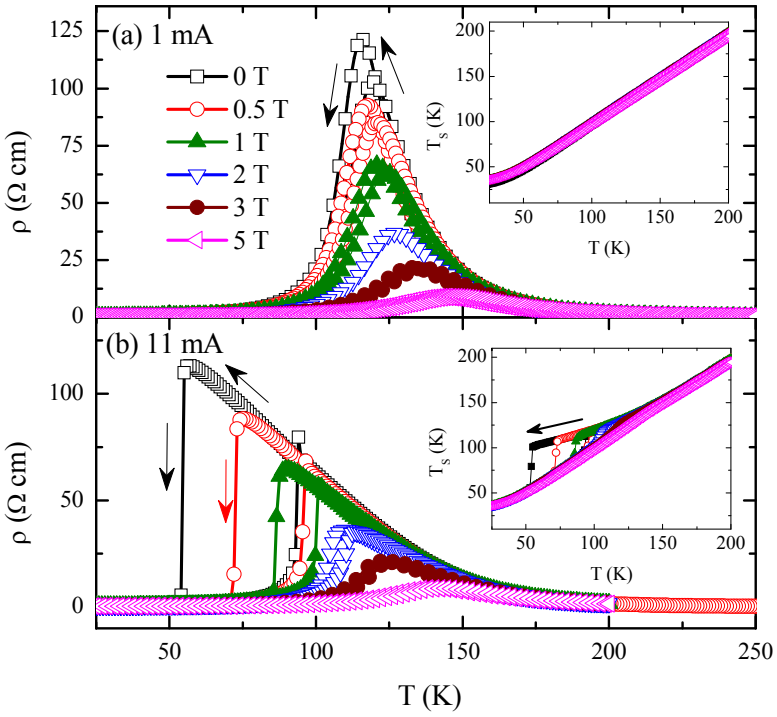

Fig. 6. 2: Temperature dependence of the resistivity, $\rho(T)$ of SS40MO sample under different external magnetic fields for (a) $I = 1$ mA and (b) $I = 11$ mA. The insets show the corresponding temperature of the sample, T_S.

We compare the effect of the magnetic field (H) on $\rho(T)$ for $I = 1$ mA and $I = 11$ mA in Fig. 6. 2(a) and Fig. 6. 2(b), respectively. The insets show T_S versus T in both cases. The application of H dramatically decreases the peak value of the resistivity for $I = 1$ mA and the

position of the peak shifts to high temperature as H increases above 2 T. The effect of magnetic field is more dramatic for I = 11 mA. A small magnetic field of $\mu_0 H$ = 0.5 T dramatically shifts the I-M transition from 52 K (under $\mu_0 H$ = 0 T) to 75 K, while cooling. As H increases further, the discontinuous I-M transition shifts upward in temperature and the width of the hysteresis decreases. Finally, the discontinuous I-M transition transforms into a smooth I-M transition for $\mu_0 H \geq 3$ T.

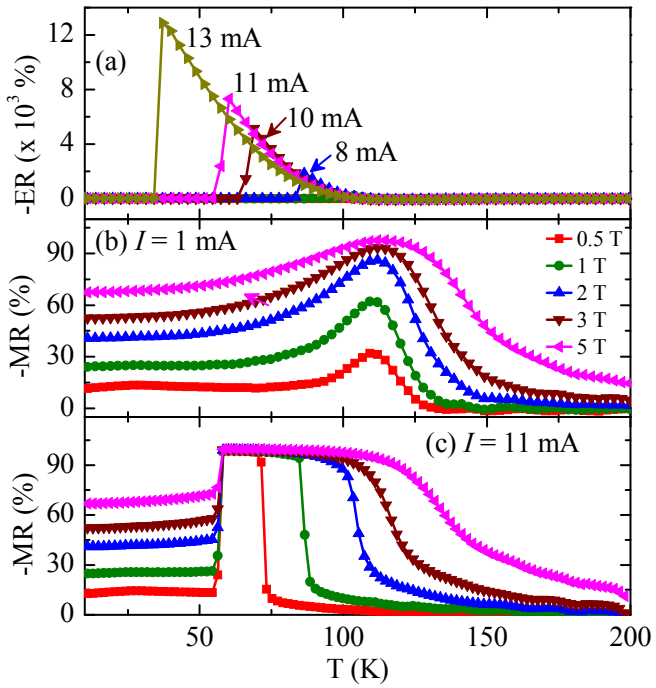

Fig. 6. 3: Temperature dependence of the (a) Electroresistance (ER) for different current strengths (*I*) in zero magnetic field. Magnetoresistance (MR) for (b) *I* = 1 mA and (c) 11 mA.

Fig. 6. 3(a) shows the electroresistance [ER (%) = [$\rho(I$ mA)–ρ(1 mA)]/ρ(1 mA)x100] as a function of temperature while cooling in zero magnetic field. The ER shows a sharp negative peak around 85 K for I = 8 mA. The magnitude of the peak increases and its position shifts to lower temperature with increasing amplitude of the current. A maximum ER of –13000 % occurs at 37 K for I = 13 mA. Fig. 6. 3(b) shows the magnetoresistance, MR(%) = [$\rho(H)$–$\rho(0)$]/$\rho(0)$x100 for I = 1 mA. The MR at $\mu_0 H$ = 0.5 T is negligible at high temperatures but it increases below 125 K upon cooling and exhibits a peak of magnitude 32 % around 100 K. The magnitude of MR increases with increasing H and reaches 98 % around T = 116 K for $\mu_0 H$ = 5 T. Fig. 6. 3(c) shows the temperature dependence of the MR for I = 11 mA. In

contrast to the behavior of MR for I = 1 mA, the temperature dependence of MR at $\mu_0 H$ = 0.5 T for I = 11 mA shows a step like increase around 74 K, followed by a plateau between 72 K and 58 K before decreasing abruptly around 56 K. The most spectacular observation is that the MR reaches nearly 100 % in the plateau region even for $\mu_0 H$ = 0.5 T compared to only 32 % MR for I = 1 mA. As H increases, the plateau extends over a wide temperature range on the high temperature side although the temperature at which MR decreases abruptly on the low temperature side is not affected. The wide temperature range over which the MR remains high is very interesting for practical applications.

Now, we compare the voltage versus current (V-I) characteristics of SS40MO sample at T = 50 and 120 K respectively under different external magnetic fields in Fig. 6. 4(a) and Fig. 6. 4(c). The current was swept from 0 → 60 mA → –60 mA → 60 mA at a stable base temperature T. The corresponding behavior of the sample surface temperature (T_S) is plotted in Fig. 6. 4(b) and Fig. 6. 4(d). Let us consider V-I characteristics at 50 K. While increasing I from 0 to 60 mA, the voltage shows a gradual and negligible increase (< 5 mV) until 30 mA. Then, a sharp spike occurs in V (i.e., the voltage shows a sharp increase at a threshold current and then after decreases as in a strong NDR behavior) around 33 mA followed by a gradual decrease with further increase in current. Upon reducing I from the maximum value, V gradually increases down to 6 mA. Then after, V decreases abruptly around 5 mA and remains small until current is reduced to zero. A symmetrical behavior is seen while reversing the current. The spike in V during the forward sweep (0→60 mA) is accompanied by an abrupt increase in T_S ($\Delta T \approx$ 70 K) and afterwards, the T_S increases gradually with further increase in current, as shown in Fig. 6. 4(b). While reducing I from 60 mA, T_S decreases gradually until 5 mA, and then shows a sharp decrease. The T_S is nearly the same as the base temperature close to the origin and shows a similar behavior in the reverse current sweep (0→–60 mA). After a final sweep (-60 → 60 mA) in the forward direction, the V-I characteristics and the T_S-I curve exhibits a prominent hysteresis. In the presence of an external magnetic field, the threshold current, at which the spike occurs, increases towards higher current values. No

abrupt jumps in the *V-I* is visible under $\mu_0 H$= 5 T. The NDR behavior is almost absent in the *V-I* characteristics under $\mu_0 H$ = 5 T. Though a NDR behavior is observed in the *V-I* characteristics at *T* = 120 K [Fig. 6. 4(c)], the peak is close to origin and broader and the hysteresis is negligible compared to the 50 K data [Fig. 6. 4(a)]. Note that the *V-I* characteristics under $\mu_0 H$ = 5 T at 120 K still exhibits a nonlinear behavior. The T_S-*I* curves show a similar trend [Fig. 6. 4(d)].

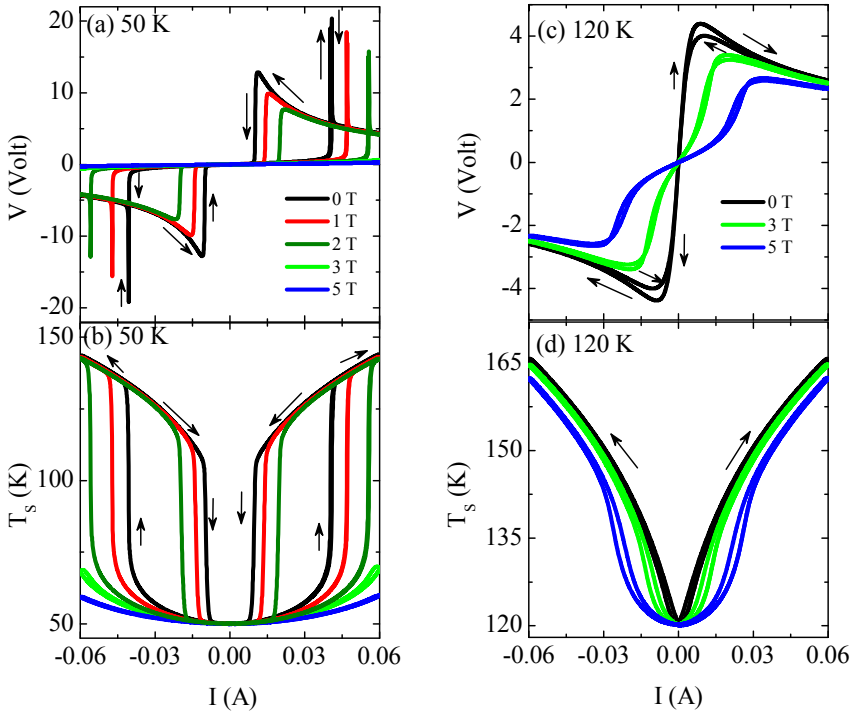

Fig. 6. 4: The voltage vs. current (*V-I*) characteristics in SS40MO sample at *T* = (a) 50 K and (c) = 120 K under $\mu_0 H$ = 0, 1, 2, 3 and 5 T. (b) and (d) show the corresponding change in the temperature of the sample (T_s)during the current sweep.

We have already seen that the nonlinear conductivity, accompanied by a large change in the surface temperature of the sample, arises from significant self-joule heating generated by the input power ($P=I^2R$). Below T_C, $d\rho/dT > 0$ and when the current is increased, the sample heats up, thereby increasing ρ till the sample temperature equals T_C. As the current increases above a threshold current, the temperature of the sample exceeds T_C ($d\rho/dT < 0$ above T_C), thus resulting in a decrease in ρ, eventually resulting in a sharp NDR behavior. In the *V-I* sweep at 120 K, initially the voltage increases linearly with current. When the current

increases and provides sufficient input power, the sample temperature increases, thus decreasing ρ to exhibit a different NDR behavior. Note that, at T= 50 K, the sharp increase in V is seen at a threshold current far away from the origin (I= 0 mA). At 50 K, due to the low resistivity, higher currents are required for a sufficient joule heating in the sample and thus an increase in the temperature of the sample. Therefore, the spike behavior occurs away from the origin. It is abrupt compared to the 120 K data since the resistivity changes across the MI region. The abruptness of the MI transition results in a sharp and peculiar nonlinear V-I curves compared to the other samples including the phase separated Ni- doped NCMO at low temperatures (please see chapter 3 for details).

At this conjecture, one may wonder about the actual behavior of the base temperature during such a large increase in the surface temperature of the sample. Therefore, we compare the change in T_S (measured by the PT100 thermometer) and the base temperature (recorded by the cryostat) during the current sweep in SS40MO sample at 50 K in Fig. 6. 5(b) and Fig. 6. 5(c), respectively. Though the T_S increases by ~ 70 K around ± 45 mA, the base temperature is surprisingly stable (± 0.3 K) throughout the sweep.

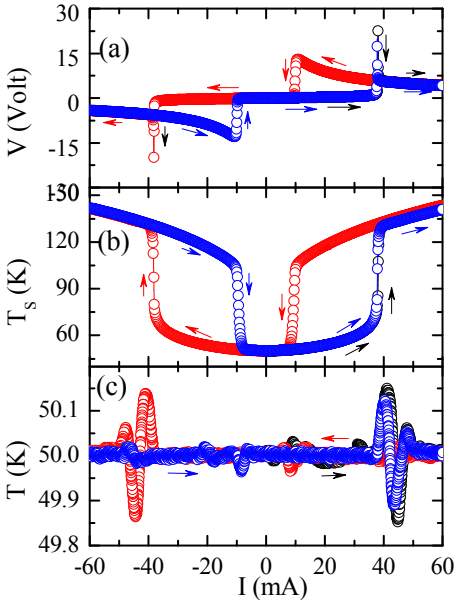

Fig. 6. 5: (a) Voltage (V), (b) Surface temperature (T_S) and (c) Base temperature (T) as a function of current. Note that the base temperature is stable throughout the current sweep except fluctuation of ±0.3 K around ±45 mA.

We have also studied the electroresistance behavior in $Sm_{0.5}Sr_{0.5}MnO_3$ (SS50MO) sample. The *V-I* characteristics at T = 50 K in SS50MO sample, as shown in the inset of Fig. 6. 6(a), is different from the SS40MO 50 K data [Fig. 6. 4(a)]. A high magnetic field of even 5 T does not have a strong effect on the peak position and behavior, as can be seen in the inset of Fig. 6. 6(a), unlike in the SS40MO compound. The NDR peaks in SS50MO occur close to the origin rather than away from the origin observed in SS40MO sample. The temperature dependence of the resistivity of SS50MO sample under different current strengths [main panel of Fig. 6. 6(a)] does not exhibit any insulator-metal transition. Note that the magnitude of the ρ(20 mA) below 50 K differs from ρ(100 μA) by a few orders of magnitude. The *V-I* characteristics at different temperatures in SS50MO sample is shown in Fig. 6. 7(a). Note that the magnitude of the NDR peak increases and the peak position shifts towards the origin with decreasing temperature. As the base temperature is decreased, the change in surface temperature induced by the current also increases, as can be seen in Fig. 6. 7(b).

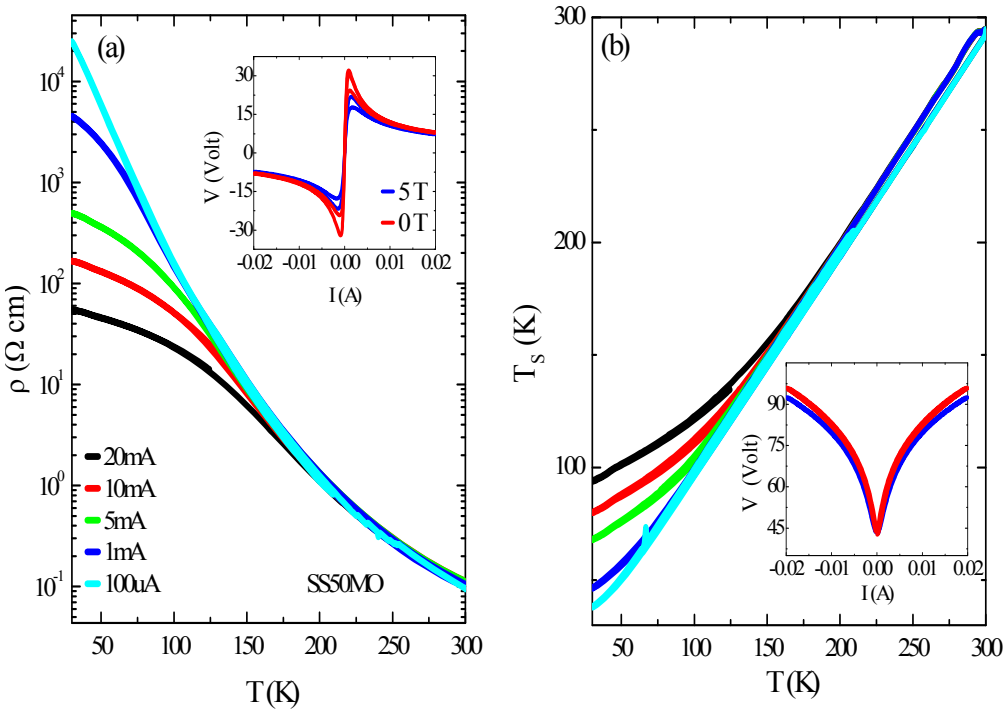

Fig. 6. 6: (a) Main panel shows the ρ-T behavior of SS50MO sample and (b) corresponding T_S-T behavior for different current strengths. The insets show (a) *V-I* and (b) corresponding T_S-I curves at 40 K under different magnetic fields.

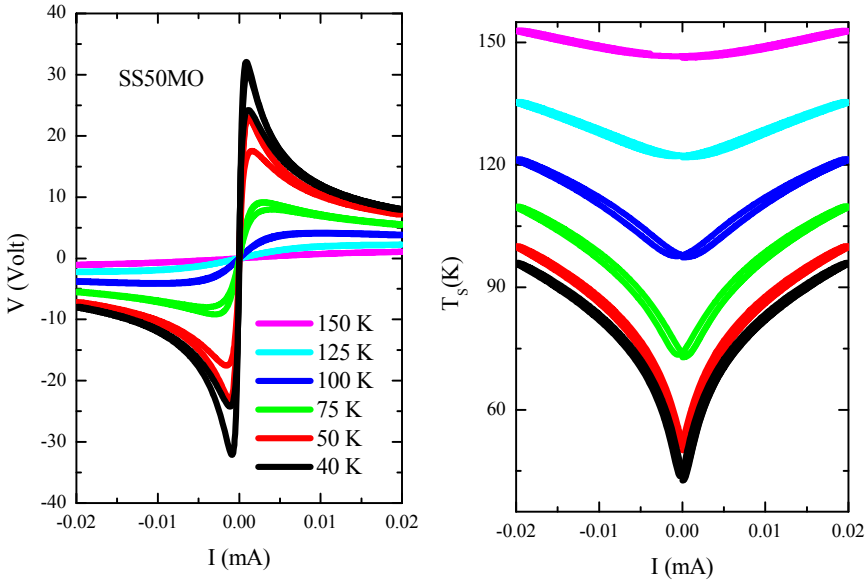

Fig. 6. 7: (a) *V-I* characteristics and (b) corresponding T_S-I curves in SS50MO sample at different temperatures.

6. 4 Discussion

There are reports of a large change in $\rho(T)$ of similar manganites with increasing current strength. A naïve explanation of this current-induced electroresistance is that forced motion of spin polarized e_g-electron under the influence of high current enhances the e_g-bandwidth, thereby reducing the scattering and hence the resistivity [76,135,136]. However, we observed large changes in the temperature of the sample during the current induced discontinuous insulator-metal behavior in $Sm_{0.6}Sr_{0.4}MnO_3$ (Fig. 6. 1-Fig. 6. 2). Therefore, the two central questions regarding these observations are: (1) What is the role of joule heating? (2) Why does $\rho(T)$ become discontinuous with increasing strength of the dc current? While cooling the sample from 300 K, the presence of a high current (for example, I = 13 mA) not only streamlines electron hopping in the direction of the electric field, but also leads to significant Joule heating. While the Joule heating is insignificant above $T \approx 180$ K, the Joule power dissipated [$P(T) = I^2R(T)$] increases for $T < 180$ K due to an increase in the resistance (R) of the sample. Since $d\rho/dT < 0$ in the paramagnetic state, the Joule heating lowers the resistivity. The Joule heating also causes the low temperature ferromagnetic phase to become

more inhomogeneous because it heats the low temperature ferromagnetic metallic phase which is partially transformed into the high temperature paramagnetic semiconducting phase. As a result, the temperature distribution within the sample is non uniform and the current flow is rather inhomogeneous. The volume fraction of the high temperature paramagnetic phase which coexists with the low temperature ferromagnetic phase increases with increasing strength of the dc current. Continuous cooling by the exchange gas in the cryostat and thermal diffusion within the sample leads to the collapse of the paramagnetic phase below the temperature T_{IM}, which results in the abrupt decrease of the resistivity and surface temperature of the sample (Fig. 6. 1). Since the paramagnetic phase has higher unit cell volume than the ferromagnetic phase [137], structural changes which accompany the collapse of the hot regions (paramagnetic phase) can aid to the sharpness of the transition. It is more likely that the similar current driven first-order transition reported at high current densities in single crystalline $La_{0.77}Ca_{0.23}MnO_3$ [138] is also caused by the Joule heating effect. When the sample is cooled under a magnetic field from room temperature, the decrease in the resistivity due to the negative magnetoresistance causes less Joule power dissipation in the sample. Hence, the volume fraction of the paramagnetic phase present at low temperature decreases with increasing strength of the magnetic field. As a result, the insulator to metal transition shifts rapidly towards high temperature in small magnetic fields $\mu_0 H < 1$ T (Fig. 6. 2). Since the resistivity decreases continuously with increasing H, the Joule heating becomes insignificant above a certain value of H. Hence, the magnitude of magnetoresistance at $\mu_0 H = 5$ T does not differ very much for $I = 1$ mA and 11 mA. The importance of inhomogeneous Joule heating was stressed by Tokunaga *et al*. [78, 98] using magneto-optical imaging techniques, and also found unusual current oscillations at a constant dc voltage bias in the phase separated Cr-doped $Nd_{0.5}Ca_{0.5}MnO_3$. It is to be noted that Gurevich *et al*. [139] predicted strange non linear current-voltage characteristics in normal metals and superconductors, arising from the Joule heating.

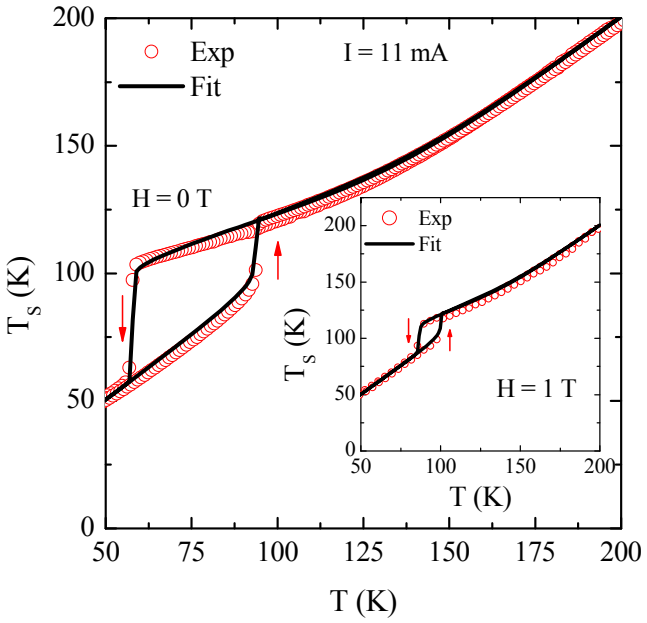

Fig. 6. 8: Experimental surface temperature of the sample (open symbols) for *I* = 11 mA and calculated surface temperature (thick line) from electrothermal model (see the text for details) as a function of the base temperature at $\mu_0 H$ = 0 T. The inset shows the data and fit at $\mu_0 H$ = 1 T.

While detail modeling of the data with inhomogeneous Joule heating is difficult, the electrical transport observed in our experiments (Fig. 6. 1-Fig. 6. 2) can be well described qualitatively by a phenomenological electrothermal model [22] following the energy balance equation, $C\frac{dT_S}{dt} = P - G(T_S - T)$. Here, C is the heat capacity of the sample, dT_S/dt denotes the rate of change of the temperature of the sample (T_S), T is the base temperature, $P = I^2R$ is the Joule power dissipated in the sample, and G stands for the effective thermal conductance which depends on the shape and surface area of the sample. The term $-G(T_S - T)$ represents the Newtonian cooling in the system. In the steady state, $C\frac{dT_S}{dt} = 0$ and hence, $T_S = \frac{I^2R}{G} + T$. Substituting the resistance value for each base temperature from Fig. 6. 1(a) and Fig. 6. 2(a) in this heat balance equation, we can calculate the surface temperature. We show the temperature dependence of calculated surface temperature (thick line) and measured surface temperature (open symbols) at $\mu_0 H$ = 0 T in the main panel of Fig. 6. 8 and at $\mu_0 H$ = 1 T in the inset for I = 11 mA. We could get a better fit for G= 3.35 mW/K which is not very

different from the value of 5.5 mW/K obtained for $La_{0.67}Ca_{0.33}MnO_3$ film by Chen and Ziese [94]. The close matching of the calculated and measured surface temperatures suggests that the observed electroresistance effect is mainly caused by the Joule heating, which leads to coexistence of the ferromagnetic and paramagnetic phases at low temperatures.

6. 5 Conclusions

In summary, we have shown that the current-driven discontinuous insulator-metal transition and colossal electroresistance in $Sm_{0.6}Sr_{0.4}MnO_3$ are primarily caused by the Joule heating, which leads to the coexistence of ferromagnetic metallic and paramagnetic semiconducting phases over a certain temperature range. Our results indicate that the input power to the sample, and hence the Joule heating can be fine tuned to enhance the low-field magnetoresistance. The present work also stresses the importance of directly measuring the actual temperature of the sample, instead of relying on the temperature recorded by a commercial instrument, in elucidating the origin of the colossal electroresistance and non linear electrical transport in manganites.

Chapter 7

Giant magnetoimpedance in $La_{0.7}Sr_{0.3}MnO_3$

7. 1 Introduction

Perovskite manganese oxides have been a topic of intense investigation for the past one decade due to the spectacular negative magnetoresistance effect shown by them [1, 140]. However, technological exploitation of the CMR effect at room temperature has been hampered by the need of magnetic field of $\mu_0 H > 1$ Tesla to induce more than -10 % magnetoresistance (MR). Extensive efforts are underway in different laboratories to enhance the magnitude of magnetoresistance at low fields, particularly in milli and micro tesla range using techniques such as artificial grain boundary in epitaxial films [141], trilayer tunnel junctions [142] and step edge junctions [143]. While the resistance studies published in the last decade were done with a direct current, high frequency electrical transport received less attention except for a few studies on microwave absorption (f = 9-40 GHz) using cavity perturbation method [144,145,146]. A substantial increase in *ac* magnetoresistance was reported in the radio frequency range (f = 1 – 10 MHz) by passing *rf* current directly though the sample [147] or through an inductance coil surrounding a manganite sample [148]. However, a detail investigation of magnetic field dependence of both the resistive and reactance components of the ac electrical impedance in manganites is rather rare.

In this chapter, we present results on the low magnetic field response of the *ac* electrical impedance in a canonical double exchange ferromagnet $La_{0.7}Sr_{0.3}MnO_3$ which does not suffer from the mesoscopic or microscopic phase segregation as often encountered in narrow band width manganites such as $Pr_{0.7}Ca_{0.3}MnO_3$ [27]. We show that *ac* magnetoresistance at room temperature in this compound is extremely high ($\Delta R/R$ % ≈ -51 % in $\mu_0 H$= 200 mT for f= 2 MHz) compared to a smaller *dc* magnetoresistance (<-2 % at $\mu_0 H$= 200 mT). We also show a distinct evolution of magnetoresistance and magnetoreactance with increasing frequency. While the field dependence of *ac* magnetoresistance is negative and

shows a single peak centered at the origin for all the frequencies, the magnetoreactance shows a transition from a single to double peak structure with increasing frequency and eventually a change of sign.

7. 2 Experimental Section

We have prepared polycrystalline $La_{0.7}Sr_{0.3}MnO_3$ (LSMO) sample by standard solid state route. The precursors La_2O_3, $SrCoO_3$ and MnO_2 (each of purity better than 99.9 %) were mixed in proper stoichiometric composition, ground and then preheated at 1373 K for 24 h. The mixture thus obtained was reground, pelletized (bar shaped), and sintered at 1473 K for 24 h. The sample was found to be single phase by X-ray and characterized further by dc magnetization, ac susceptibility and resistivity measurements. The four probe *ac* resistance (R) and inductive reactance (X) of the electrical impedance $(Z(\omega,H) = R(\omega,H) + j\, X(\omega,H))$ in polycrystalline LSMO rectangular bar shaped samples have been measured with an Agilent 4285A LCR meter. The details of the experimental set up are provided in chapter 2.

7. 3 Results and Discussion

Fig. 7. 1 shows the XRD pattern of the $La_{0.7}Sr_{0.3}MnO_3$ (LSMO) compound at room temperature, which reveals single phase pattern. The observed XRD pattern was indexed to rhombohedral structure of LSMO with space group $R\bar{3}c$. The prominent peaks in the XRD pattern are indexed by its crystallographic planes, as represented by the miller indices (*hkl*) in accordance with Ref. 149.

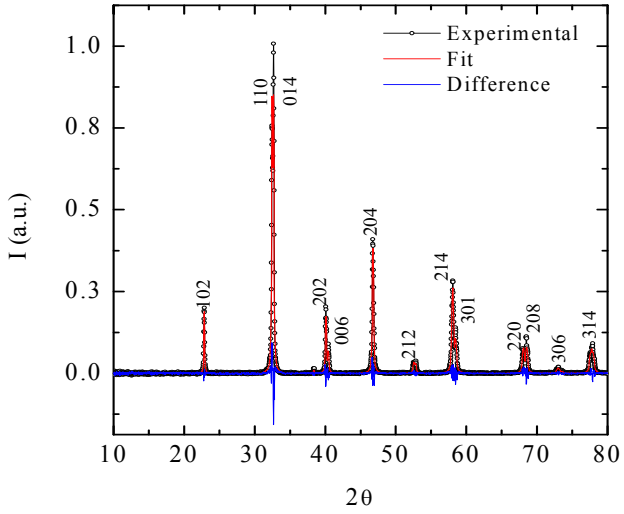

Fig. 7. 1: XRD pattern of $La_{0.7}Sr_{0.3}MnO_3$

The main panel of Fig. 7. 2 shows the magnetization versus field (*M-H*) curves of LSMO sample at different temperatures and the inset shows the temperature (*T*) dependence of *M* under $\mu_0 H$= 0.1 T. While cooling from 400 K, the magnetic moment shows an abrupt increase around T_C, then after increases gradually with further decreases in temperature and reaches a saturation value of M_S = 2.75 μ_B at low temperature, as can be seen in the inset.

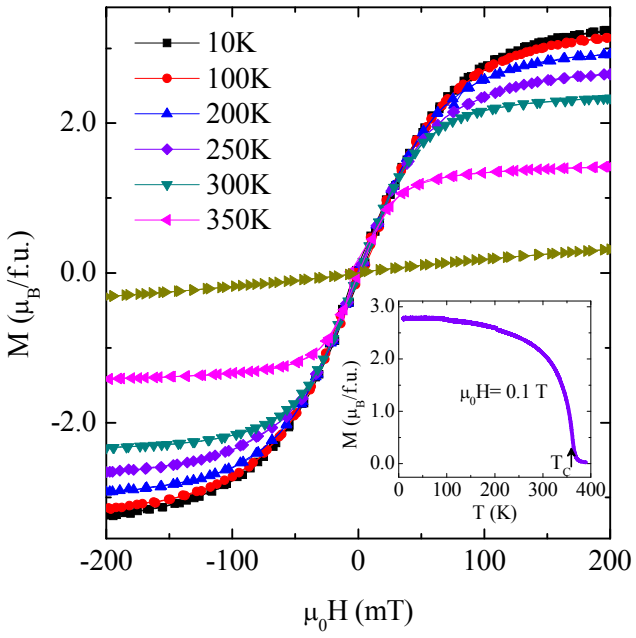

Fig. 7. 2: Magnetization (*M*) versus field (*H*) curves at different temperatures in LSMO sample. The inset shows the temperature (*T*) dependence of *M* under a magnetic field $\mu_0 H$ = 0.1 T.

The ferromagnetic Curie temperature of the sample determined from the inflection point of the *M-T* curve is T_C = 365±2 K. Above T_C, the *M-H* curve shows a linear paramagnetic behavior, while at low temperatures, the *M-H* curves show typical ferromagnetic behavior, as shown in the main panel of Fig. 7. 2.

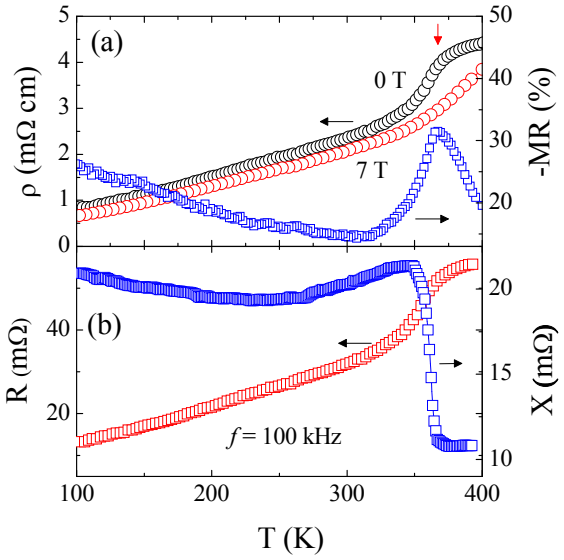

Fig. 7. 3: (a) Temperature dependence of the *dc* resistivity under $\mu_0 H$ = 0 T and 7 T (left scale) and magnetoresistance (right scale) of LSMO sample. The downward pointed arrows indicate the Curie temperature (T_c). (b) Temperature dependence of the *ac* resistance *R* (left scale) and reactance *X* (right scale) for *f* = 100 kHz at $\mu_0 H$= 0 T.

Fig. 7. 3(a) (left scale) shows the temperature dependence of the resistivity $\rho(T)$ of $La_{0.7}Sr_{0.3}MnO_3$ in $\mu_0 H$ = 0 and 7 T measured with direct current (*I*= 3 mA). The sample is metallic both in the paramagnetic and ferromagnetic states but a large decrease in the resistivity occurs just below the T_C. The paramagnetic to ferromagnetic transition is second-order in this compound. Under the application of 7 T magnetic field, the resistivity decreases in the entire temperature range and the ferromagnetic transition temperature shifts above 400 K. The magnetoresistance, MR(%) = [ρ(7 T)-ρ(0 T)]/ρ(0 T)x100 is plotted on the right scale. The MR shows a peak around the T_C and its value is -31 % under $\mu_0 H$ = 7 T. However, MR increases with lowering *T* and reaches ~ 26 % at 100 K. This trend in the *dc* MR behavior

suggests that spin-polarized tunneling across the grain boundary at low temperatures is dominant in LSMO at low temperatures [16]. Fig. 7. 3(b) shows the zero field temperature dependence of the four probe *ac* resistance (R) (on the left scale) and inductive reactance (X) (on the right scale) of an LSMO sample, of dimensions 10.1x3.6x2.2 mm^3 with 5.3 mm distance between the voltage probes, for f = 100 kHz. The behavior of R is similar to the dc resistivity. The smooth decrease in R around T_C is accompanied by a steep increase in the zero-field inductive reactance ($X = \omega L$) around $T = T_C = 365\pm2$ K. Thus, impedance measurements allow us to simultaneously probe the charge transport and magnetic behavior with R and X, respectively.

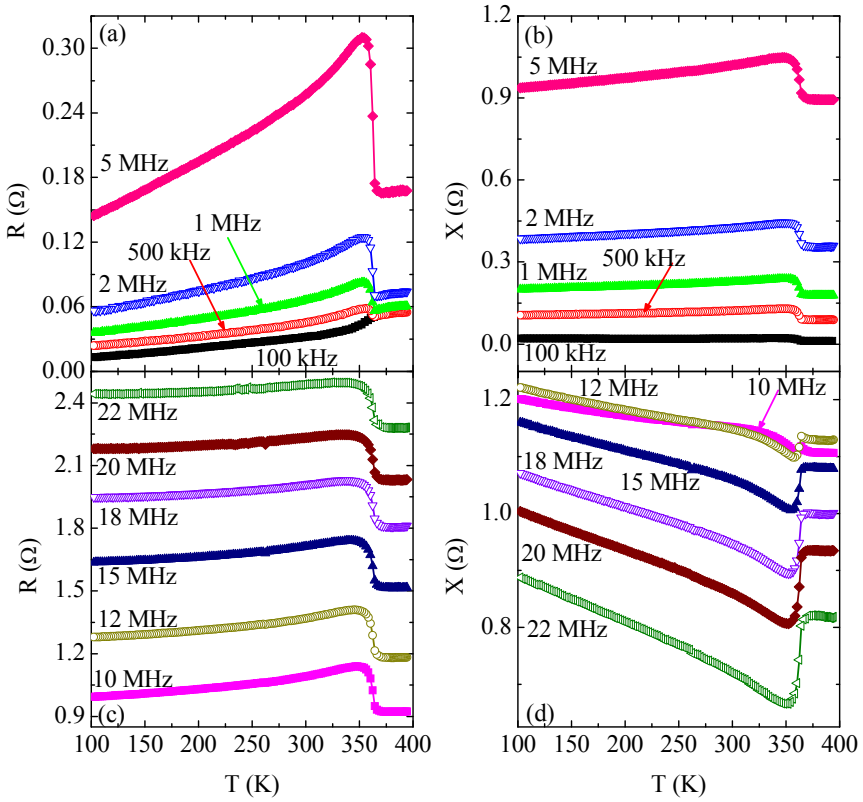

Fig. 7. 4. The left panel shows the temperature dependence of the ac resistance (R) for various frequencies, (a) $f \leq 5$ MHz, and (c) $f \geq 10$ MHz in zero external magnetic field. The respective reactance (X) vs. temperature curves are shown in the right panel. Note the cross over from abrupt increase to abrupt decrease in X around T_C with increasing frequency.

Fig. 7. 4(a) shows the temperature dependence of R for different frequencies, f = 100 kHz to 5 MHz in $\mu_0 H$ = 0 T. It can be seen that the smooth decrease of R around T_C for f =

100 kHz transforms into an abrupt increase followed by a peak for $f \geq 500$ kHz. Below the peak, R decreases monotonically with lowering temperature. The value of the ac resistance at $T = 400$ K increases rapidly with frequency for $f > 1$MHz. The abrupt increase in R at T_C is also seen at higher frequencies as shown in Fig. 7. 4 (c). Fig. 7. 4(b) and Fig. 7. 4(d) show the $X(T)$ for 100 kHz $\leq f \leq$ 5 MHz and 10 MHz $\leq f \leq$ 22 MHz, respectively. The notable observation is for $f >$ 10 MHz, wherein the abrupt increase of X at T_C for low frequencies is superseded by an abrupt decrease at T_C [see Fig. 7. 4(d)].

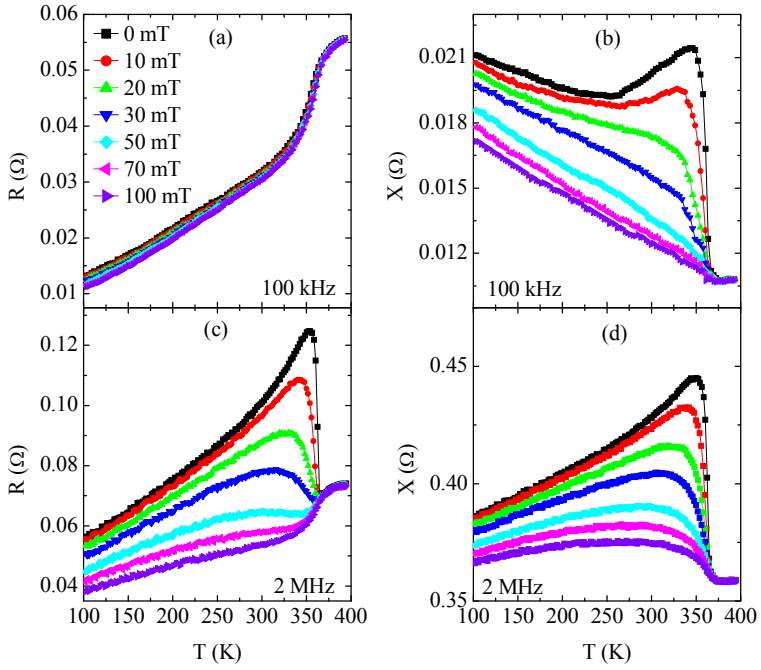

Fig. 7. 5: Temperature dependence of the *ac* resistance (*R*) and reactance (*X*) of $La_{0.7}Sr_{0.3}MnO_3$ for *f* = 100 kHz and 2 MHz under different *dc* bias magnetic fields (*H*).

Next, we discuss the temperature dependence of R for $f = 100$ kHz at different values of the dc magnetic field ($\mu_0 H$ = 0–100 mT) in Fig. 7. 5(a). The magnetic fields were applied parallel to the length of the sample and hence parallel to the direction of current. The magnitude and behavior of $R(T)$ do not show any significant difference under different low magnetic fields, as can be seen in Fig. 7. 5(a). In contrast to the zero field $R(T)$ for 100 kHz, $R(T)$ curve in zero field for f= 2 MHz [Fig. 7. 5(c)] shows a sharp increase at T_C followed by a

peak. The peak decreases in magnitude, broadens and shifts down in temperature with increasing strength of the dc magnetic field. For $\mu_0 H$ = 100 mT, the peak is completely suppressed and the behavior is restored to the temperature dependence of R at f = 100 kHz or *dc* resistivity in the zero field. Contrary to the behavior of $R(T)$ under different magnetic fields for 100 kHz [Fig. 7. 5(a)], the low external magnetic field has a dramatic influence on the $X(T)$ for f= 100 kHz, as exemplified in [Fig. 7. 5(b)]. The amplitude of the peak observed in the zero field $X(T)$ around T_C diminishes with increasing magnetic field. X shows a gradual increase with lowering temperature under $\mu_0 H$= 100 mT. The applied magnetic field has similar influence on the reactance for f= 2 MHz, as can be seen in Fig. 7. 5(d). Nevertheless, a notable difference is that while the peak in X is completely suppressed at H = 100 mT for f = 100 kHz, a broad maximum is still visible around 300 K under $\mu_0 H$ = 100 mT for f = 2 MHz.

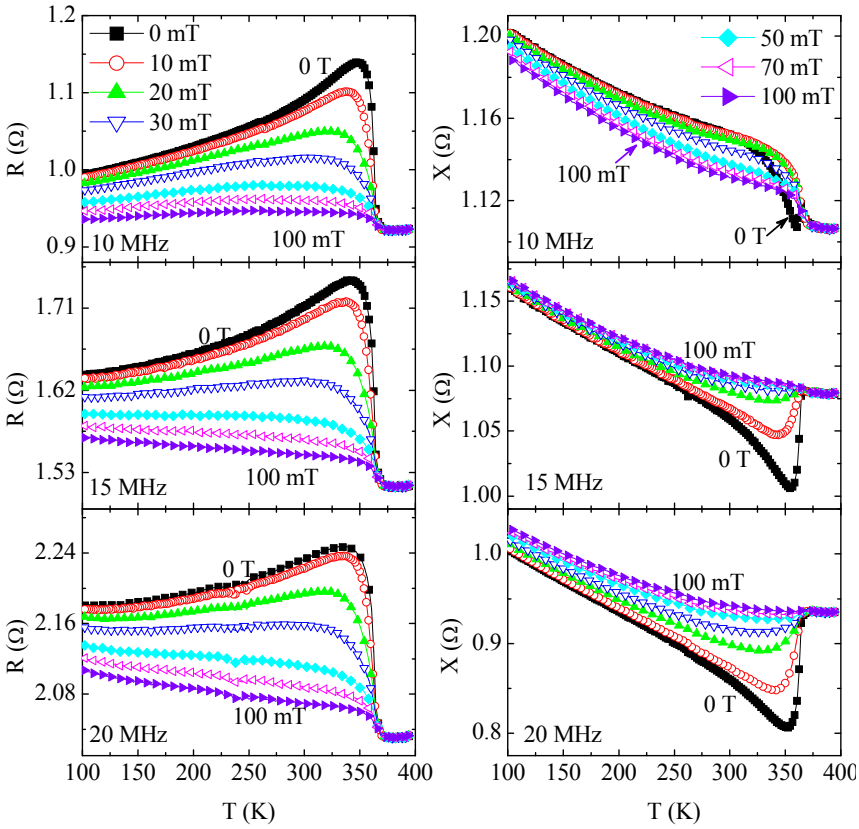

Fig. 7. 6: Left panel shows the temperature (*T*) dependence of the *ac* resistance *R* for *f* = 10 MHz (top), 15 MHz (middle) and 20 MHz (bottom) under different *dc* bias magnetic fields (*H*). The right panel shows the corresponding reactance (*X*) versus temperature curves.

The left panel of Fig. 7. 6 shows $R(T)$ at f = 10 MHz (top), 15 MHz (middle) and 20 MHz (bottom). The effect of the magnetic field on $R(T)$ at all these frequencies is nearly identical. Surprisingly, the effect of magnetic field on $X(T)$ differs for the three frequencies, as shown on the right panel. While X in $\mu_0 H$ = 0 T shows a rapid increase at T_C for f = 10 MHz (top), a sharp decrease followed by a minimum is seen for f = 15 and 20 MHz, as plotted in the middle and bottom panel, respectively. The applied magnetic field enhances the value of the X for f = 15 and 20 MHz and the minimum gets suppressed. In contrast to the low frequency $X(T)$, the magnetic field increases the reactance at higher frequencies over the whole temperature range.

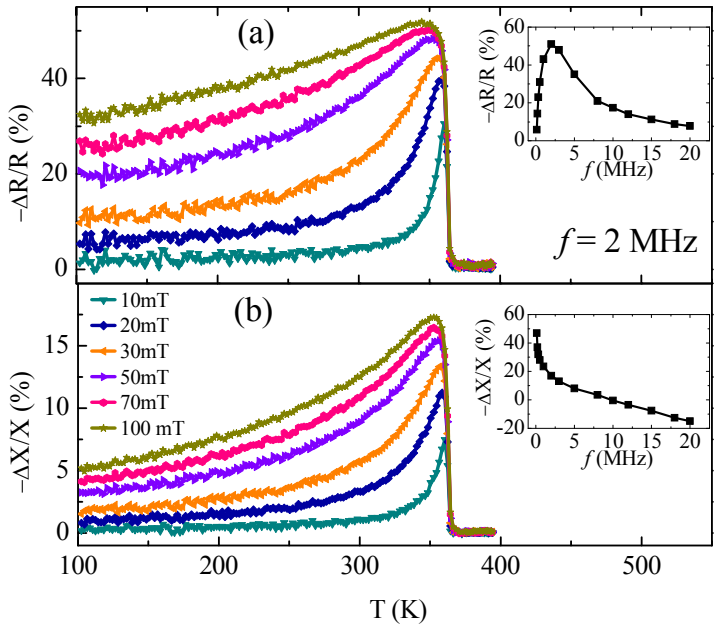

Fig. 7. 7: Temperature dependence of the (a) *ac* magnetoresistance $\Delta R/R$ (%), and (b) magnetoreactance $\Delta X/X$ (%) under different bias magnetic fields (H) at f = 2 MHz. The insets show the frequency dependence of the peak value of the respective quantities at $\mu_0 H$ = 100 mT.

Fig. 7. 7(a) shows the temperature dependence of the ac magnetoresistance, $-\Delta R/R$(%) =$[R(0)-R(H)]/R(0)$x100, for f= 2 MHz under different values of the magnetic field ($\mu_0 H$ = 10-100 mT). The magnitude of the magnetoresistance at the lowest field ($\mu_0 H$ = 10 mT) is negligible above T_C but increases sharply at T_C while cooling and exhibits a peak of value 29

%. The magnitude of the peak decreases with further lowering temperature and approaches a low value of 3 % at 100 K. As the strength of the applied magnetic field increases, the magnitude of the peak in $\Delta R/R$ increases and the peak broadens. At $\mu_0 H$ = 100 mT, the magnitude of the peak reaches a value of 53 % around 360 K. It is a remarkably high value since we observed only –31% dc magnetoresistance even at $\mu_0 H$ = 7 T [Fig. 7. 3(a)]. The inset shows the frequency dependence of the peak value of the magnetoresistance under $\mu_0 H$ = 100 mT. The magnitude of $\Delta R/R$ initially increases with frequency, shows a maximum of 53 % around f = 2-3 MHz and then decreases to 8 % at f = 20 MHz. The temperature dependence of ac magnetoreactance $-\Delta X/X(\%) = [X(0)-X(H)]/X(0)\text{x}100$ for f = 2 MHz under different field values also shows a peak around T_C [Fig. 7. 7(b)]. The magnitude of the peak increases from ≈7 % under $\mu_0 H$ = 10 mT to ≈17 % under $\mu_0 H$ = 100 mT. The inset of Fig. 7. 7(b) indicates that the magnitude of the magnetoreactance is higher at the lowest frequency; it decreases with increasing frequency. Notably, $\Delta X/X$ changes sign from negative to positive around 12 MHz.

The observed peak in the temperature dependence of the *ac* magnetoresistance in both the configurations close to T_C is opposite to the behavior of the grain boundary related magnetoresistance in polycrystalline manganites. In polycrystalline ferromagnetic manganites, the low field magnetoresistance at low temperatures arises from the spin polarized tunneling of e_g holes between misaligned ferromagnetic grains through spin disordered grain boundaries [150]. This tunneling magnetoresistance is largest at 4.2 K and decreases to zero at T_C. Intrinsic magnetoresistance of intra-grain origin is dominant close to the magnetic phase transition and it shows a sharp peak around T_C when a sufficiently large dc magnetic field is applied [151]. Our above results indicate that the high frequency *ac* magnetoresistance in our sample is sensitive to the intra-grain magnetization process rather than to the tunneling magnetoresistance. Majumdar and Littlewood [152] proposed a phenomenological model which attributes the large magnetoresistance observed near T_C in wide band width itinerant ferromagnets such as $La_{0.7}Sr_{0.3}MO_3$ (M = Co, Mn) to the

suppression of magnetic fluctuations by an external magnetic field. This model predicts a large magnetoresistance around T_C and negligible magnetoresistance for $T << T_C$ and $T >> T_C$ which closely resembles our observations.

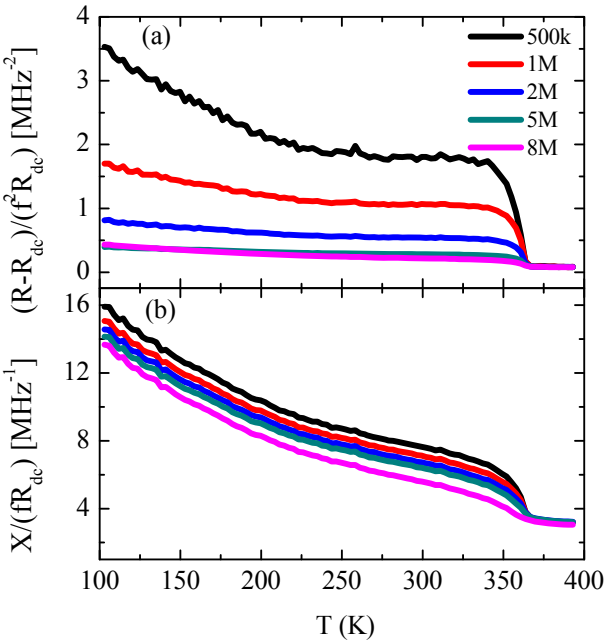

Fig. 7. 8: Temperature dependence of the (a) normalized ac resistance $(R\text{-}R_{dc})/(R_{dc}f^2)$ and (b) normalized reactance, $X/(R_{dc}f)$ in zero external magnetic field for f ≤ 8 MHz. Here f is the frequency of the ac current excitation and $R_{dc} \approx R_{100kHz}$.

The high frequency current imprints magnetic signature on the electrical transport through change in the magnetic penetration depth. From the classical theory of electromagnetic wave propagation, the electrical impedance of a current carrying conductor of cylindrical wire of radius a is given by,

$$Z/R_{dc} = (ka)J_0(ka)/2J_1(ka),$$

where R_{dc} is the dc resistance, $k = (1+i)/\delta$, J_0 and J_1 are zero and first-order Bessel functions [61]. If the skin is effect is weak, the real part of the impedance for the cylindrical geometry is written as,

$$Z' = R = R_{dc}[1+1/48(a/\delta)^4]$$

$$= R_{dc}[1+(\mu_t\sigma\omega a^2)^2/192],$$

where the impedance,

$$Z = Z'+iZ'' = R + iX.$$

Thus, the ac resistance in the ferromagnetic state will rise above the dc resistance if the 2nd term in the bracket dominates the dc resistance. The 2nd term in the bracket is due to the eddy current which shields the interior of the ferromagnetic grains from the alternating magnetic field. Upon rearrangement,

$$(R-R_{dc})/(R_{dc}f^2)= \mu_t^2 \sigma^2(A^2\pi^2/48),$$

where A is the cross sectional area of the wire. Thus, the normalized resistance is proportional to the products of the squares of the transverse permeability (μ_t) and the conductivity (σ). On the other hand, the reactance

$$Z'' = X = ¼\ R_{dc}(a/\delta)^2$$

$$= R_{dc}(\mu_t\sigma\omega a^2)/8,$$

and hence,

$$X/(R_{dc}f) = \sigma\mu_t A/4.$$

Hence, the reactance is proportional to μ_t. Thus, the observed features in R and X in the absence of magnetic field are proportional to μ_t^2 and μ_t, respectively. Fig. 7. 8(a) shows the normalized resistance $[R-R_{dc}]/(f^2R_{dc})$ as a function of temperature T, where R is the resistance at frequency f and R_{dc} is the dc resistance. Since the dc resistance was found to be identical to the ac resistance at 100 kHz, we take R_{dc} = R(100 kHz). We find that the normalized resistance is nearly zero and independent of the frequency in the paramagnetic state, but it rises rapidly at T_C and then increases gradually with lowering temperature. The magnitude of the normalized resistance below T_C decreases with increasing frequency. In Fig. 7. 8(b) we show $X/(fR_{dc})$ versus T. The $X/(fR_{dc})$ is nearly same for all the frequencies above T_C, but increases monotonically with decreasing temperature below T_C for each frequency. Note that the magnitude of $X/(fR_{dc})$ below T_C decreases with increasing frequency. As the dc magnetic field applied along the long axis of the sample increases, the transverse permeability decreases which leads to suppression of R and X. The temperature dependence of the zero field R [Fig. 7. 5(a)] at 100 kHz is identical to the temperature dependence of R at 2 MHz in a

field of 70 mT, which clearly suggests that the external field is sufficient to destroy the excess resistance observed near T_C in zero field for f= 2 MHz.

The decrease in the amplitude and downward shift of R and X in temperature with increasing *dc* bias field is reminiscent of the behavior of *ac* susceptibility under increasing *dc* bias magnetic field, as reported in a variety of systems including spin glass [$BiMn_{0.6}Sc_{0.4}O_3$, Ref. 153] and cluster glass ($La_{0.67}Ca_{0.33}Mn_{1-x}Ta_xO_3$, $x \geq 0.05$, Ref. 154) compounds as well as in long-range itinerant ferromagnets such as $ZrZn_2$ [155], $Pr_{0.5}Sr_{0.5}CoO_3$ [156] and $La_{0.73}Ba_{0.27}MnO_3$ [Ref. 157]. In a long range ferromagnet such as the titled compound, the observed behavior is most likely connected with the dynamics of domain walls. Application of a *dc* bias field enlarges the domain size and aligns the magnetization of a domain along its direction. Hence, the smaller *ac* magnetic field is unable to move the domain walls further. As a result, the amplitude of the *ac* susceptibility decreases with increasing bias field. Very close to T_C, the suppression of spin fluctuations further dramatically reduces the ac susceptibility and leads to an increase in the magnetic penetration depth ($\delta = \sqrt{(2\rho/\omega\mu)}$, resulting in a huge negative magnetoimpedance as observed. The position of the maximum in the temperature dependence of susceptibility is most likely determined by the competition between the thermal energy, which enhances the spin fluctuations and energies involved in pinning the domain walls. Spin dependent scattering of charges by oscillating domain walls could influence the resistivity and ac magnetoresistance close to the Curie temperature as suggested by Machado *et al.* [158] for cobalt based amorphous ribbons but we have yet to understand its impact in our complex oxides.

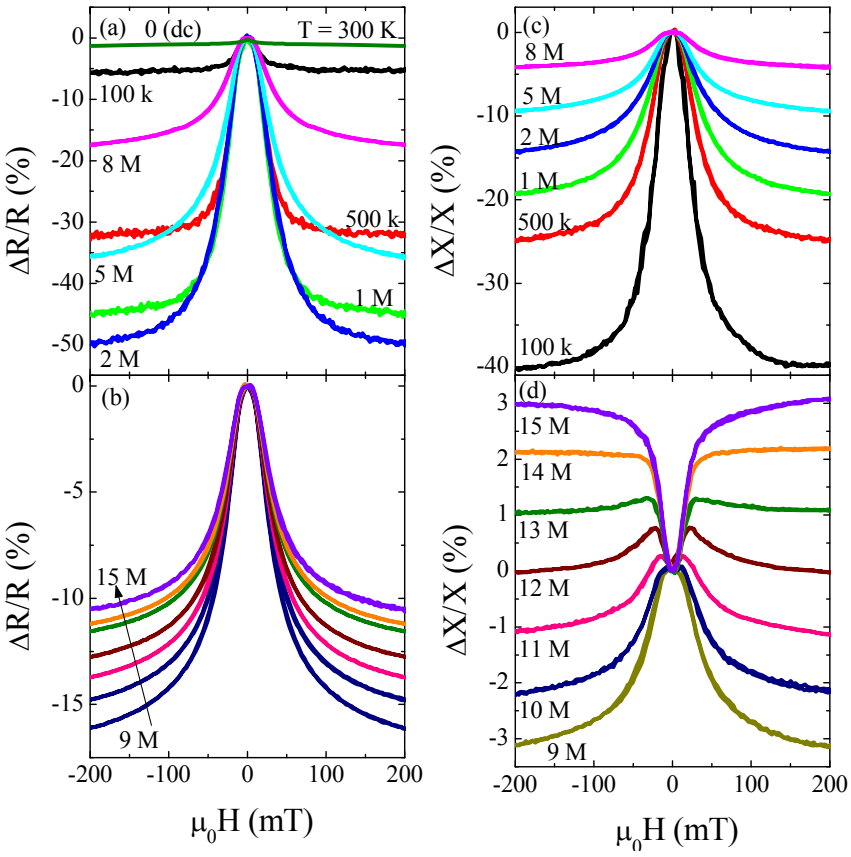

Fig. 7. 9: Magnetic field dependence of the ac magnetoresistance ($\Delta R/R$) for (a) $f < 9$ MHz and (b) $f \geq 9$ MHz at 300 K. The ac magnetoreactance ($\Delta X/X$) at various fixed frequencies for (c) $f < 9$ MHz and (d) $f \geq 9$ MHz. The labels indicate the frequencies in Hz.

Having looked into the temperature dependence of the ac magnetoresistance and magnetoreactance, we now discuss the field dependence of $\Delta R/R$ at room temperature (T= 300 K) in Fig. 7. 9(a) for $f < 9$ MHz and Fig. 7. 9(b) for $f \geq 9$ MHz. The magnitude of $\Delta R/R$ increases rapidly in the field range -50 mT < $\mu_0 H$ < 50 mT. At still higher fields, $\Delta R/R$ varies gradually with increasing magnetic field. The magnitude of $\Delta R/R$ at 200 mT reaches a maximum of 51 % for f = 2 MHz and decreases with increasing frequency above 5 MHz. The observed ac magnetoresistance of -51 % at 2 MHz in a small magnetic field of 200 mT is indeed remarkable compared to the smaller dc magnetoresistance (< -2 % at 200 mT). Fig. 7. 9(c) and Fig. 7. 9(d) show the magnetoreactance ($\Delta X/X$) as a function of field. The $\Delta X/X$ is negative and has a maximum value of -40 % at 100 kHz. As the frequency increases, $\Delta X/X$ decreases, becomes less negative and it crosses over to a positive value around f = 12 MHz. Instead of a single peak behavior in the field dependence of ΔX/X observed for $f \leq 10$ MHz

(centered around the origin $\mu_0 H$= 0 mT), $\Delta X/X$ for $f \geq 10$ MHz exhibits a double peak behavior with the two peaks positioned at $\pm H_K$, as exemplified in Fig. 7. 9(d). Although the double peak initially shifts upward in field with increasing frequency within a narrow range of frequencies (9-13 MHz), the peaks become less distinguishable at higher frequencies. The rounding of the peaks is due to the distribution of the anisotropies. The shift of the peak position (H_K) with increasing frequency is plotted in Fig. 7. 10.

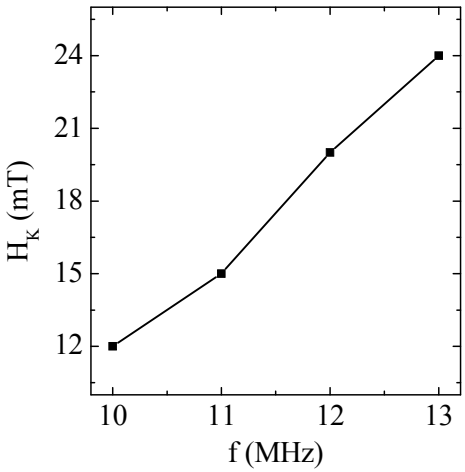

Fig. 7. 10: Shift in the double peak position (H_K) with increasing frequency at 300 K

Both domain wall oscillation and domain magnetization rotation contribute to the circular permeability at low frequencies. At low frequencies $\omega \leq \omega_r$ where ω_r is a characteristic relaxation frequency of the domain wall movement, the main contribution to the permeability of the material comes from the motion of domain walls, which bulges or enlarges under the ac magnetic field. The external magnetic field applied to the sample restricts domain displacement, which results in decrease of the effective permeability. This in turn, results in increase in skin depth and decrease in the electrical impedance, thereby causing a single peak in both $\Delta R/R$ and $\Delta X/X$ at the origin and monotonous increase in the magnitude with increasing field. However, at higher frequencies, domain wall oscillation is damped out due to microeddy currents and hence the major contribution to the permeability is due to domain magnetization rotation. Suppose the sample consists of domains, whose magnetization points along the easy axis determined by the anisotropy field (H_K), and the *dc* magnetic field (H) is

applied along the hard axis which is normal to the direction of H_K. When H is increased, the magnetization in each domain rotates towards the external field axis, increasing the circular permeability and in turn the impedance. The permeability reaches a maximum when H balances the transverse anisotropy field H_K, wherein occurs an abrupt rotation of domain magnetization (M) towards the *dc* field direction [159]. For $H>H_K$, M is along the field direction. Using energy minimization in an ideal circumferential domain structure, it has been theoretically shown that the transverse susceptibility can show a divergence when $H = \pm H_K$ and dispersion in anisotropy can remove this divergence [159]. As a consequence, a peak occurs in the impedance at $H = \pm H_K$. In particular, the transition from single to double peak with increasing frequency is due to the change in magnetization dynamics from domain wall oscillation to domain magnetization rotation. For $f \geq 13$ MHz, we see that the impedance increases rapidly at low fields but does not decrease at higher magnetic fields. This is because the permeability is independent of magnetic field at high frequencies.

In the very high frequency range (from a few MHz to a few GHz), not only the penetration depth undergoes large variations, but also effects leading to ferromagnetic resonance (FMR) can occur, which results in huge changes of the effective magnetic permeability of sample. It has been demonstrated, both theoretically and experimentally, that a GMI measurement is analogous to a FMR experiment at high enough exciting frequencies and presents the basic features of the ferromagnetic resonance process [160]. Though ferromagnetic resonance is generally observed in the GHz range in saturated ferromagnetic samples, it can also appear in the MHz range in multi domain (unsaturated state) state [161] or in the internal anisotropy field (H_K) in the sample. It has been recently shown that there is no lower limit to the minimum frequency needed to observe the FMR features [162]. In unsaturated samples, the resonant frequency is mainly controlled by the dispersion of the anisotropy axes [163], by the internal DC and AC fields, that is by the domain structure of the wire [164], and by the damping mechanisms. Recently, ferromagnetic resonance–like behavior in magnetoimpedance (a change in sign of X and shift of X with frequency) was reported in a few materials that include amorphous CoFeSiBNb wire around 900 kHz [165],

NiFe/Cu/NiFe multilayers around 500 MHz [166], and Fe-Co-Si-B amorphous ribbon around 100 MHz [167]. The occurrence of both ferromagnetic resonance and antiresonance in magnetoimpedance was also demonstrated in certain amorphous ribbons [160]. However, signature of ferromagnetic resonance in the MHz range in manganites has not been reported so far. Another possibility is the magnetoelastic resonance of domain walls. Maartense and Searle [168] found transition from single to double peak behavior in the *rf* transverse susceptibility of α-Fe_2O_3 below 80 MHz and attributed to the coupling between crystal's acoustic resonance modes and low-lying spin-wave modes excited near local crystal strains. Recently, *rf* current induced domain wall resonance was also reported in a permalloy nanowire [169].

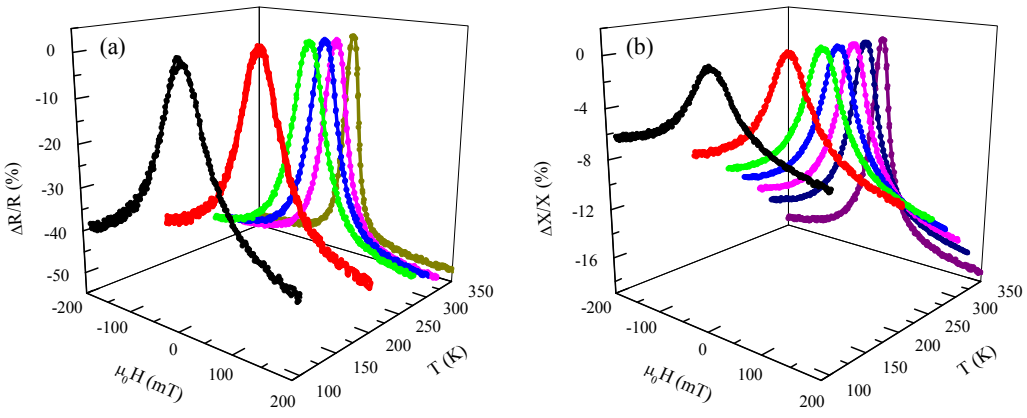

Fig. 7. 11: Magnetic field dependence of the (a) ac magnetoresistance $\Delta R/R$ and (b) ac magnetoreactance $\Delta X/X$ for f = 2 MHz at different temperatures.

Since the magnitude of the ac magnetoresistance and magnetoreactance are largest around T_C, the field dependence of $\Delta R/R$ and $\Delta X/X$ for representative frequencies f= 2, 12 and 20 MHz were studied at various temperatures. We show the evolution of $\Delta R/R$ and $\Delta X/X$ with changing temperature in Fig. 7. 11(a) and Fig. 7. 11(b), respectively for f= 2 MHz. Though the magnitude of the $\Delta R/R$ and $\Delta X/X$ at 200 mT decreases with decreasing temperature, both show a single peak behavior centered at origin ($\mu_0 H$= 0 T) at all the temperatures. For example, at $\mu_0 H$= 200 mT, the magnitude of $\Delta R/R$ ($\Delta X/X$) decreases from 52 (18) % at T= 350

K to 39 (6) % at T= 100 K. Near to the T_C, the magnitudes of both $\Delta R/R$ and $\Delta X/X$ approach saturation at low field values whereas at low temperatures it tends to saturate at higher field values. This behavior resembles the behavior of *M-H* curves, wherein the magnetization tends to saturate at lower magnetic fields for temperatures near T_C compared to far below T_C (please see Fig. 7. 2). It is discussed earlier that the change in the impedance at low frequencies under the magnetic field originates from the permeability changes caused by the effect of magnetic field on the domain wall displacements.

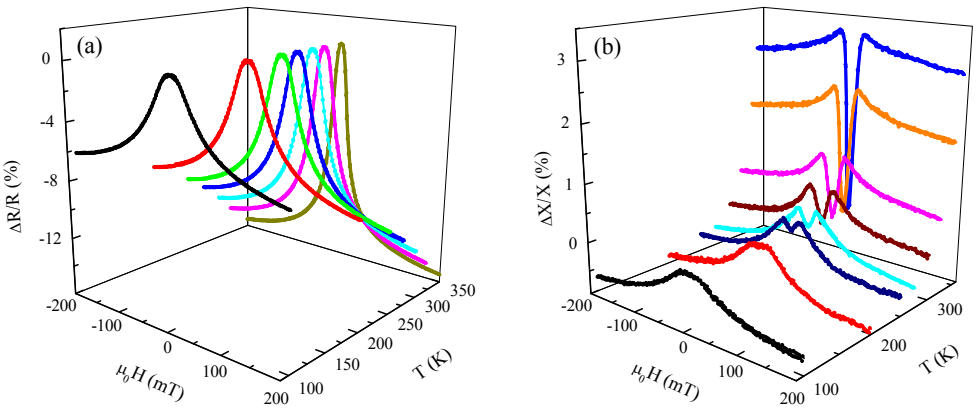

Fig. 7. 12: Magnetic field dependence of the (a) ac magnetoresistance $\Delta R/R$ and (b) ac magnetoreactance $\Delta X/X$ for f = 12 MHz at different temperatures.

More interesting is the evolution of $\Delta R/R$ and $\Delta X/X$ with temperature for f= 12 MHz. As can be seen in Fig. 7. 12(a), the magnitude of $\Delta R/R$ dramatically decreases with decreasing temperature for f = 12 MHz compared to 2 MHz data [Fig. 7. 11(a)]. In contrast to $\Delta X/X$ for f= 2 MHz [Fig. 7. 11(b)] which shows a single peak behavior at all temperatures, we see prominent double peak behavior at temperatures close to T_C for f= 12 MHz. Upon decreasing the temperature, the double peak behavior becomes less visible at 12 MHz. A change of sign from negative to positive is clearly visible with increasing temperature. For f= 20 MHz, $\Delta R/R$ remains negative whereas $\Delta X/X$ remains positive at all temperatures, as shown in Fig. 7. 13(a) and Fig. 7. 13(b), respectively.

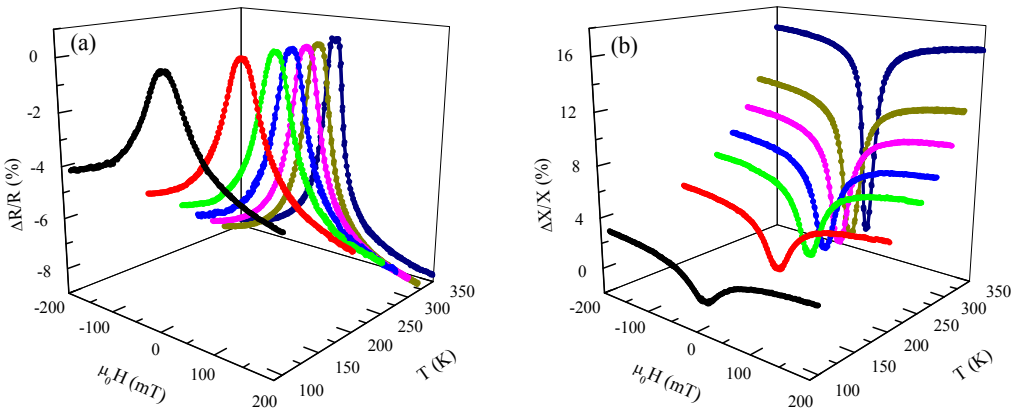

Fig. 7. 13: Magnetic field dependence of the (a) ac magnetoresistance $\Delta R/R$ and (b) ac magnetoreactance $\Delta X/X$ for f = 20 MHz at different temperatures.

Next, we discuss in detail how the magnitude of the magnetoresistance and the features in the magnetoreactance are affected by the measurement geometry in LSMO in ambient environment for the first time. We have performed two types of distance variation: (i) the length between the voltage probes (l_v) are varied while keeping the length between the current electrodes (l_i) constant and (ii) The length between voltage probes fixed, but the length of the sample and hence the distance between the current electrodes changed. The former method is equivalent to mapping the profile of the magnetoimpedance.

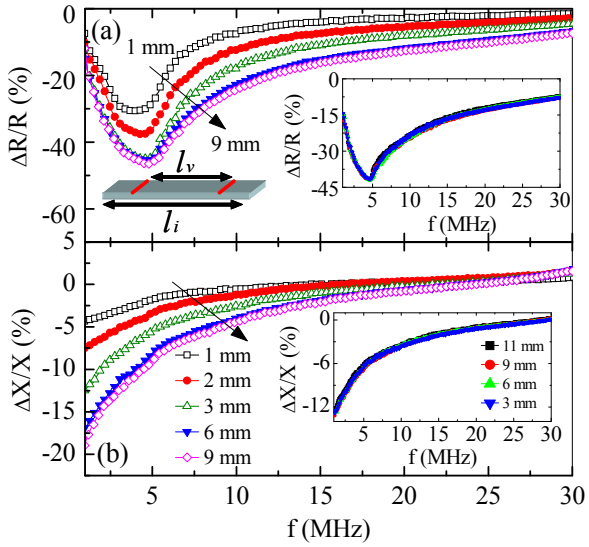

Fig. 7. 14: Frequency dependence of (a) $\Delta R/R$ and (b) $\Delta X/X$ for various lengths between the voltage probes (l_v). The insets show the respective frequency dependence for various lengths between the current probes (l_i).

The frequency dependence of the ac magnetoresistance, $\Delta R/R$ and magnetoreactance, $\Delta X/X$ in $\mu_0 H$= 100 mT for different lengths between the voltage probes in the four probe impedance measurements are shown in Fig. 7. 14. The schematic of the experimental configuration is shown in the inset. In Fig. 7. 14(a), we show the frequency dependence of $\Delta R/R$ at 300 K for a sample with different lengths between the voltage probes (l_v (in mm) = 9, 6, 3, 2 and 1) where the distance between the current probes was kept constant (l_i= 11 mm). When l_v = 9 mm, $\Delta R/R$ initially increases, shows a maximum (= 47 %) around 5 MHz and then decreases at higher frequencies. The frequency dependence of $\Delta R/R$ for other l_vs also shows a similar behavior. The $\Delta R/R$ is nearly independent of frequency below 1 MHz, but shows a marked dependence on l_v above 1 MHz. The magnitude of the maximum in $\Delta R/R$ decreases with decreasing l_v (≈ 47 % for l_v = 9mm to ≈ 30 % for l_v = 1 mm). Fig. 7. 14(b) shows the frequency dependence of $\Delta X/X$ for various lengths between the voltage probes. Here, the magnitudes of $\Delta X/X$, particularly below 5 MHz, are dramatically affected by varying l_v. In the insets of Fig. 7. 14(a) and Fig. 7. 14(b), we show the frequency dependence of $\Delta R/R$ and $\Delta X/X$ respectively, for various length between the current probes (l_i (in mm) = 11, 9, 6, and 3), for a fixed distance between the voltage probes (l_v= 2.5 mm). Interestingly, the frequency dependence does not show any remarkable variation for different distance between the current probes.

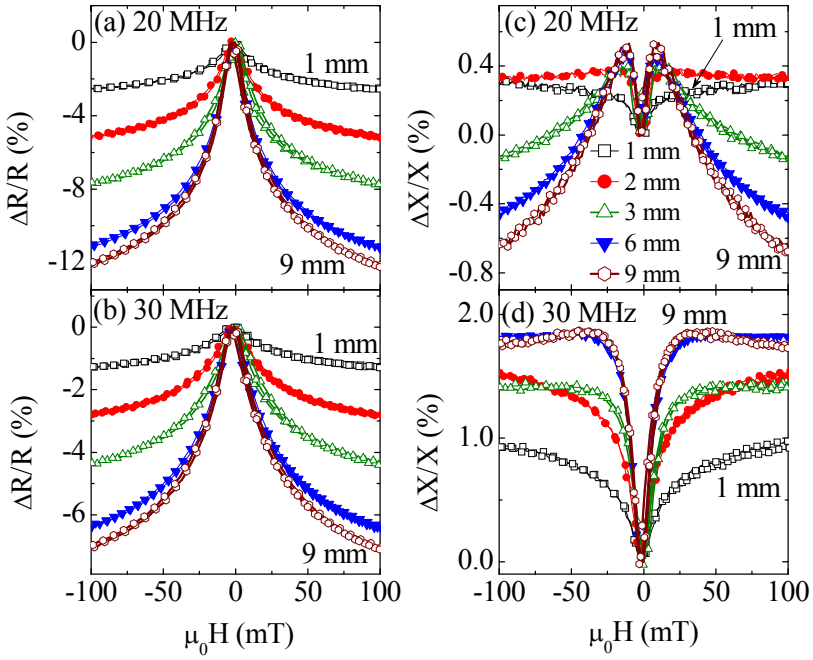

Fig. 7. 15: Magnetic field dependence of the ac magnetoresistance $\Delta R/R$ at (a) f = 20 MHz and (b) 30 MHz for various l_vs. The magnetoreactance $\Delta X/X$ at (c) f = 20 MHz and (d) 30 MHz are also shown. Note that the $\Delta X/X$ for 30 MHz remains positive for all l_vs.

Next, we show how the distance between the voltage probes (l_v) influences the magnetic field dependence of impedance at two selected frequencies, f = 20 and 30 MHz, where the double peak structures are prominent. Fig. 7. 15(a) and Fig. 7. 15(b) show the field dependence of $\Delta R/R$ at f = 20 MHz, and 30 MHz respectively. We find that the magnitude of $\Delta R/R$ systematically decreases with decreasing l_v. For example, the magnitudes of $\Delta R/R$ at the maximum field for 20 (30) MHz is > 12 (7) % when l_v= 9mm, but it reduces to < 3 (1) % when l_v = 1 mm. More interestingly, $\Delta X/X$ shows a striking difference between different l_vs. While $\Delta X/X$ for l_v = 9 mm at 20 MHz [Fig. 7. 15(c)] shows a positive double peak at H_p = ± 30 mT and negative values at higher fields, it shows an increasing tendency to be positive with decreasing l_v. It can be seen that $\Delta X/X$ is positive over the entire field range for l_v = 1 mm. However, the $\Delta X/X$ at 30 MHz [Fig. 7. 15(d)] for all l_vs remains positive and the magnitude of the peak decreases with decrease in l_v. We have also measured the dc magnetoresistance for various l_v, but the observed difference between the longest and the shortest l_v was almost negligible within experimental errors.

Thus, our results clearly show that the observed magnetoimpedance effects are dependent not only on the frequency of the ac signal and the strength of the dc magnetic field, but also on the length between the voltage probes of the sample. The ac impedance of a ferromagnetic sample is sensitive to the frequency and field dependence of the circular permeability, $\mu_\varphi(\omega,H)$. When the skin effect is weak ($\delta >>$ thickness of the sample), $Z = R_{dc} + j\omega L_i$ where R_{dc} is the dc resistance, ω is the angular frequency of the *rf* current, and L_i is the internal inductance of the sample, which depends on the circular permeability through $L_i = G\mu_\varphi(\omega,H)$ where G is the geometrical factor. Note that when the skin effect is strong, $Z \propto (1+j)\sqrt{(\omega\rho\mu_0\mu_\varphi/2)}$, the circular permeability affects both the ac resistance and the reactance [170]. Considering the complex nature of the permeability ($\mu_\phi = \mu_\phi' - j\mu_\phi''$), impedance in the weak skin effect regime under a magnetic field H becomes $Z(\omega,H) = R_{dc}(H) + G\omega\mu_0\mu_\phi(\omega,H)'' + jG\omega\mu_0\mu_\phi(\omega,H)'$. Thus, the reactance ($X$) depends on the real part of the circular permeability and the ac resistance (R) depends on the magnetic loss determined by the imaginary part of the permeability. Hence, the observed dependence on the distance between the voltage probes suggests that the high frequency electrical transport probes the local variations of circular permeability of ferromagnetic grains enclosed between the voltage probes. As l_v increases, more number of ferromagnetic grains is sampled and as a result, average transverse permeability can increase in magnitude. Vázquez *et al*. [171] have found similar results in amorphous ferromagnetic FeCrSiBCuNb alloy wires, when one of the voltage probes was fixed at one end of the sample and another one was varied along the length of the sample. They have reported the total impedance (ΔZ/Z) and the measurements were confined to a maximum frequency of 5 MHz. From the local measurement of *B-H* loops, they have observed that the magnetization decreases and coercivity increases with decreasing distance between the voltage probes. It was suggested that the closure domain structure and domain wall pinning promotes magnetic hardness at the ends of the sample. The magnetoimpedance in our samples, surprisingly, does not depend on

the length of the sample as long as the distance between the voltage probes is fixed and the magnetic field is applied along the length of the sample. This suggests that demagnetization effect plays less important role in the magnetoimpedance of bulk and thick manganites in axial dc magnetic field, which is opposite to the behavior found in other amorphous ferromagnetic alloys [172].

7. 6 Conclusions

Major results drawn out of the investigation of magnetoimpedance in $La_{0.7}Sr_{0.3}MnO_3$, as discussed in this chapter, can be summarized as follows:

1. A huge *ac* magnetoresistance (= -51 % in $\mu_0 H$ = 200 mT, f = 2 MHz) is observed at room temperature compared to the smaller *d*c magnetoresistance (<–2 %). Thus, we could propose an alternative strategy to improve the low field magnetoresistance at room temperature for device applications.
2. It is shown that, while the magnetoresistance and magnetoreactance exhibit a single peak centered at $\mu_0 H$ = 0 T at low frequencies, the single peak in magnetoreactance at low frequencies transforms into a valley at the origin and a double peak at $H=\pm H_k$ at high frequencies. While the magnetoresistance is negative for all frequencies, the sign of magnetoreactance changes from negative to positive with increasing frequency.
3. The observed high frequency features are related to the magnetization dynamics arising from magnetization rotation and domain wall motion. In spite of a large body of reports on magnetoresistance and dc electrical transport in manganites, the details of high frequency micro-magnetism in manganites related to magnetization dynamics and domain structure under low magnetic fields are scarce and are beyond the scope of present study. However, the dynamics of domain wall oscillations at low frequencies and

magnetization rotation at higher frequencies and their respective contribution to the magnetic permeability are theoretically studied in amorphous wires, as explained in this chapter. Therefore, we feel that such mechanisms play the key role behind the observed magnetoimpedance results in LSMO. The possibility of domain wall ferromagnetic resonance is also discussed.

4. We have also investigated the influence of measurement geometry on the magnetoimpedance features and demonstrated that the high frequency electrical transport is sensitive to local variations in magnetic permeability.

5. While detail understanding of the observed results requires knowledge of micro-magnetism related to magnetization dynamics and domain structure, our results may set certain guidelines while considering the MI effect for practical applications. Our results suggest magnetoimpedance as an effective tool to spatially map the local magnetic profile of magnetic materials.

Chapter 8

Conclusions and Future Works

In this thesis, we have investigated electroresistance, magnetoimpedance and magnetocaloric effects in selected manganites of different electronic and magnetic ground states. The intriguing results observed in the study are correlated with different intrinsic and extrinsic mechanisms. While the observed electroresistance in manganites at high current strength is mostly attributed to Joule heating mechanisms which is often neglected in the literature, the large magnetocaloric effects are correlated to the intrinsic nanoscale phase separation and metamagnetic transition in manganites. Notably, huge and unusual magnetoimpedance effects are observed in manganites at low magnetic fields, which are explained on the basis of magnetization dynamics. In this chapter, main conclusions drawn out from the results of this work are summarized and some of the possible future works are proposed.

8. 1 Conclusions

8. 1. 1 Colossal electroresistance in selected manganites

Electroresistance effects were studied in both charge ordered and phase separated compounds such as $Nd_{0.5}Ca_{0.5}Mn_{1-x}Ni_xO_3$ (x=0.0, 0.05, 0.07) [173] and narrow bandwidth systems such as $Sm_{1-x}Sr_xMnO_3$ (x= 0.4, 0.5) [174]. A comprehensive study of both direct and pulsed current induced electroresistance effects were carried out in these systems, which were rarely investigated earlier by other researchers. Various exotic current induced behaviors such as negative differential resistance [173], magnetoresistance avalanche [175] and first order insulator-metal transition [174] are discussed. A quantitative study is carried out to understand the role of joule heating and plausible intrinsic mechanisms in CER effect. The main findings in the study are:

1. It is observed that, the strong nonlinear *VI* characteristics, current induced electroresistance effects and negative differential resistance behavior in $Nd_{0.5}Ca_{0.5}Mn_{1-x}Ni_xO_3$ (x= 0, 0.05, and 0.07) are accompanied by large changes in the surface temperature of the sample in the dc mode. Therefore, the observed strong nonlinear effects are attributed to the joule heating mechanism under high current strength in manganites.
2. It is suggested that, the direct measurement of the surface temperature of the sample is essential and mandatory in electroresistance measurements, before attributing the electroresistance effects to various exotic mechanisms. Our study suggests that cryostat temperature can be much different from the actual surface temperature of the sample during the electroresistance behavior.
3. A nonlinear effect and resistivity switching is observed in the pulsed mode with changing pulse period and pulse width in Ni-doped NCMO manganites, which is assisted by phase separation and accompanied by a negligible change in the surface temperature. Therefore, these results are ascribed to the role played by intrinsic mechanisms, which are often masked by the thermal changes in the dc mode.
4. The effect of dc current strength on the field dependence of the magnetoresistance in $Nd_{0.5}Ca_{0.5}Mn_{1-x}Ni_xO_3$ (x= 0.05, 0.07) is also investigated. A current induced magnetoresistance avalanche at critical values of the magnetic field is demonstrated. Surprisingly, the avalanche in magnetoresistance is accompanied by abrupt changes in the temperature of the sample ($\Delta T \approx 47$ K).
5. It is shown that, the nonlinear *VI* characteristics in a narrow band width manganite $Sm_{0.6}Sr_{0.4}MnO_3$ at low temperatures exhibits more sharp

negative differential resistance (NDR) behavior and wider hysteresis compared to the Ni-doped NCMO samples.

6. Interestingly, a current induced first order insulator to metal transition (I-M) is observed in $Sm_{0.6}Sr_{0.4}MnO_3$. It is shown that with increasing magnitude of the current, the I-M transition shifts down in temperature and accompanied by an abrupt decrease in temperature of the sample. These results underscores the importance of inhomogeneous Joule heating that leads to coexistence of high temperature paramagnetic phase with low temperature ferromagnetic phase over a wide temperature range. The results could be well described by a phenomenological electrothermal model. It is also demonstrated that Joule heating can be fine tuned to enhance the low field magnetoresistance in manganites over a wide temperature range.

8. 1. 2 Magnetocaloric effect in selected manganites

Magnetotransport and magnetocaloric effects were investigated, mainly in $Sm_{1-x}Sr_xMnO_3$ (x= 0.3–0.5) [176]. The major results can be summarized as follows:

1. It is shown that a magnetic field-driven first-order metamagnetic transition occurs in the paramagnetic state in x= 0.4 and 0.5 and a second order transition in x= 0.3

2. A large magnetic entropy change ($-\Delta S_m$= 6.2 J/kgK for ΔH= 5 T at T= 125 K) is observed in $Sm_{0.6}Sr_{0.4}MnO_3$, which is associated with the metamagnetic transition resulting form the field-induced growth and coalescence of ferromagnetic nanoclusters pre-existing in the paramagnetic state.

3. Based on the aforementioned results, it is suggested that manganites with nanoscale phase separation, particularly those with interacting

superparamagnetic clusters in the paramagnetic phase can be good candidates for magnetic refrigeration.

8. 1. 3 Magnetoimpedance effect in selected manganites

The four probe ac resistance and reactance are studied as a function of temperature, frequency and external magnetic field in a canonical double exchange manganite $La_{0.7}Sr_{0.3}MnO_3$ [177, 178, 179]. A large magnetoimpedance is observed at low magnetic fields in $La_{0.7}Sr_{0.3}MnO_3$ at or above room temperature and the major findings can be summarized as follows:

1. A huge *ac* magnetoresistance (= –51 % in $\mu_0 H$ = 200 mT, f = 2 MHz) is observed at room temperature compared to the smaller *d*c magnetoresistance (<–2 %). Thus, an alternative strategy is proposed to improve the low field magnetoresistance at room temperature for device applications.
2. It is shown that, while the magnetoresistance and magnetoreactance exhibit a single peak centered at $\mu_0 H$ = 0 T at low frequencies, the single peak in magnetoreactance at low frequencies transforms into a valley at the origin and a double peak at $H=\pm H_k$ at high frequencies. While the magnetoresistance is negative for all frequencies, the sign of magnetoreactance changes from negative to positive with increasing frequency. The observed features are related to the magnetization dynamics arising from magnetization rotation and domain wall motion. The possibility of domain wall ferromagnetic resonance is also discussed.
3. The influence of measurement geometry on the magnetoimpedance features is also investigated for the first time. It is demonstrated that high frequency electrical transport in bulk manganites is sensitive to the local

variations in magnetic permeability rather than on the demagnetization factor.

4. While detail understanding of the observed results requires knowledge of micro-magnetism related to magnetization dynamics and domain structure, the results in this study may set certain guidelines while considering the MI effect for practical applications. It is also suggested that magnetoimpedance can be an effective tool to spatially map the local magnetic profile of magnetic materials.

8. 2 Future works

8. 2. 1 Extension of electroresistance studies in manganites.

Although we could measure the actual surface temperature of the sample during the electroresistance measurements and observe large change in T_S in bulk manganites, the behavior in thin films and single crystals need not be the same. Therefore, it is worthy to synthesize the thin films of aforementioned sample and investigate the origin of electroresistance, though the measurements are comparatively difficult. It is clear from our electroresistance results that the intrinsic mechanisms are overshadowed by the thermal behavior in the sample. Therefore, one of our prime objectives is to single out these mechanisms and look for similar materials that can show electroresistance behavior with less thermal effects. It is also worthwhile to investigate the relevance of hysteresis and switching behavior observed in our samples in the context of memristors, which has recently attracted a lot of attention [180].

Another remarkable observation is the magnetoresistance avalanches at critical magnetic field values, which are accompanied by abrupt changes in the temperature of the sample. Such a strong magnetothermal coupling resembles magnetothermal phenomena like Ettingshausen effect and magneto-Peltier effects, which are rarely investigated in manganites. The flow of high dc current in a sample transverse to the magnetic field can also create temperature gradient transverse to the direction of the current (Ettingshausen effect [104]) or

along the direction of the current (magneto-Peltier effect [105]).The prospects of magneto-Peltier effects and Ettingshausen cooling effects have to be explored in detail in manganites due to their potential significance in the recent quest for alternative refrigeration technologies. Most importantly, further experiments have to be designed to investigate the possibility of a temperature gradient in the sample. Though our results indicate a strong interplay between magnetoresistance and thermal behavior, the mechanism of the coupling is not clear at present and further work has to be carried out to understand the observed effects.

8. 2. 2 Further investigation of magnetoimpedance in manganites.

Magnetoimpedance was investigated mainly in $La_{0.7}Sr_{0.3}MnO_3$ sample which showed a huge and unusual magnetoimpedance behavior at or above room temperature. This large low field magnetoimpedance at or above room temperature in manganites can be exploited for various sensor applications. The results were attributed to the suppression of magnetic fluctuations near T_C, which causes an increase in the magnetic penetration depth and a decrease in the impedance. However, there are mainly three questions still remains unanswered: Firstly, what is the role of tunneling magnetoresistance at higher frequencies? Secondly, can we observe the low-field ac magnetoresistance in single crystals or epitaxial thin films? Finally, what are the influences of microstructure on the magnetoimpedance? Note that the detailed knowledge of domain structure in these manganites is rather scarce. Further investigation of magnetoimpedance in samples whose electrical transport is dominated by tunneling mechanisms, extending the study of influence of geometry of the sample and thickness dependence of magnetoimpedance etc. can shed light on the exact origin of the observed magnetoimpedance effect at high frequencies. In addition, it will be worthwhile to correlate the observed unusual magnetoimpedance effects with the domain structure in the sample. Also, further studies above 30 MHz and in a completely saturated state in the aforementioned samples will be useful to understand the possibility of ferromagnetic resonance in manganites.

8. 2. 3 Continuation of magnetocaloric studies in manganites.

It is also promising to find out materials that can show a large entropy change around room temperature for magnetic refrigerator applications. Nanoscale phase separation in the paramagnetic state is one of the key points behind manganites that can show large magnetocaloric effects, as indicated by the results in $Sm_{1-x}Sr_xMnO_3$. Therefore magnetocaloric studies have to be extended to manganites which have superparamagnetic clusters in the paramagnetic state around room temperature.

Our study of electroresistance, magnetoimpedance and magnetocaloric effects in selected manganites reveal interesting results both in the view point of fundamental physics as well as technological applications. The potential applications include memory devices, sensors and refrigeration. The results of the present study can be exploited to design and develop versatile devices using manganites. Indeed, manganites well deserve to be called as multifunctional materials based on the results presented in this work.

Bibliography

[1] Y. Tokura (Ed.), *Colossal Magnetoresistive Oxides* (Gordon & Breach Science Publishers, Singapore, 2000); C. N. R. Rao, and B. Raveau (Eds.), *Colossal Magnetoresistance, Charge Ordering and Related Properties of Manganese Oxides* (World Scientific, Singapore, 1998).

[2] K. A. Müller, and J. G. Bednorz, Science **237**, 1133 (1987).

[3] R. von Helmolt, J. Wecker, B. Holzapfel, L. Schultz, and K. Samwer, Phys. Rev. Lett. **71**, 2331 (1993).

[4] V. M. Goldschmidt, *Geochemistry* (Oxford University Press, Oxford, 1958); J. B. Goodenough, J. A. Kafalas, and J. M. Longon, *Preparation Methods in Solid State Chemistry* P. Hagenmuller (Ed.) (Academic, New York, 1972); A. Manthiram and J. B. Goodenough, J. Solid State Chem. **92** 231, (1991).

[5] S. Blundell, *Magnetism in Condensed Matter* (Oxford Universiy Press, New York, 2001)

[6] W. E. Pickett and D. J. Singh, Phys. Rev. B **53** 1146 (1995).

[7] J. Kanamori, J. Appl. Phys. **31** 14S (1960).

[8] R. Orbach, and H. J. E. Stapleton, *Spin-Lattice Relaxation Electron Paramagnetic Resonance*, S Geschwind (Ed.) (Plenum, New York, 1972) chapter 2.

[9] K. I. Kugel and D. I. Khomskii, Uspekhi Fizicheskikh Nauk **136**, 621 (1982); Y. Murakami, J. Hill, D. Gibbs, M. Blume, I. Koyama, M. Tanaka, H. Kawata, T. Arima, Y. Tokura, K. Hirota, and Y. Endoh, Phys. Rev. Lett. **81**, 582 (1998).

[10] F. Duan and J. Guojun, *Introduction to Condensed Matter Physics* (World Scientific, Singapore, 2005) chapter 13.

[11] P.W. Anderson, and H. Hasegawa, Phys. Rev. **100**, 67 (1955).

[12] C. Zener, Phys. Rev. **82**, 403 (1951).

[13] P.-G. de Gennes, Phys. Rev. **118**, 141 (1960).

[14]A. Urushibara, Y. Moritomo, T. Arima, A. Asamitsu, G. Kido, and Y. Tokura, Phys. Rev. B **51**, 14103 (1995).

[15]R. Mahendiran, S. K. Tiwary, A. K. Raychaudhuri, T. V. Ramakrishnan, R. Mahesh, N. Rangavittal, and C.N. R. Rao, Phys. Rev. B, **53,** 3348 (1996) ; R. Mahendiran, A. K. Raychaudhuri, A. Chainani, D. D. Sarma, and S. B. Roy, Appl. Phys. Lett. **66,** 233 (1995).

[16] A.J. Millis, P.B. Littlewood, B.I. Shraiman, Phys. Rev. Lett. **74**, 5144 (1995); A.J. Millis, R. Mueller, B.I. Shraiman, Phys. Rev. B **54**, 5405 (1996).

[17] C.M. Varma, Phys. Rev. B 54 (1996) 7328.

[18] M. Kataoka, M. Tachiki, Physica B **237** 24 (1997).

[19] J. B. Goodenough, and A. L. Loeb, Phys. Rev. **98**, 391 (1955); J. B. Goodenough, *ibid*. **100**, 564 (1955); J. Kanamori, J. Phys. Chem. Solids **10**, 87 (1959); J. B. Goodenough, *ibid*. **6**, 287 (1958).

[20] E. J. W. Verwey, and P. W. Haaymann, Physica **8**, 979 (1941).

[21] C. N. R. Rao, A. Arulraj, P. N. Santosh, and A. K. Cheetham, Chem. Mater. **10**, 2714 (1998).

[22] E. O. Wollan, and W. C. Koehler, Phys. Rev. **100**, 545 (1955).

[23] Z. Jirak, S. Krupicka, Z. Simsa, M. Dlouha, and S. Vratislav, J. Magn. Magn. Mater. **53**, 153 (1985).

[24] For a recent review, see Y. Tokura, and N. Naogosa, Science **288**, 462 (2000).

[25] C. H. Chen and S. W. Cheong, Phys. Rev. Lett. **76** 4042 (1996); C. H. Chen, S. W. Cheong and H. Y. Hwang, J. Appl. Phys. **81** 4326 (1997).

[26] C. N. R. Rao, and B. Raveau, *Transition Metal Oxides: Structure, Properties and Synthesis of Ceramic Oxides*, 2nd Ed. (Wiley, New York, 1998); E. Sigmund and A. K. Müller (Eds.) *Phase Separation in Cuprate Superconductors* (Springer, Heidelberg, 1994).

[27] E. Dagotto (Ed.), *Nanoscale Phase separation and Colossal Magnetoresistance* (Springer, Berlin, 2002); E. Dagotto, T. Hotta and A. Moreo, Phys. Rep. **344** 1 (2001); A. Moreo, S. Yunoki and E. Dagotto Science **283** 2034 (1999).

[28] E. L. Nagaev, JETP Lett. **6** 18 (1967); E. L. Nagaev, Sov. Phys. Lett. **27**, 122 (1968); E. L. Nagaev, JETP Lett. **16** 3948 (1972); E. L. Nagaev, *Physics of Magnetic Semiconductors* (Mir Publisher, Moscow, 1986); E. L. Nagaev, Phys. Rep. **346**, 387 (2001).

[29] C. N. R. Rao, A. Arulraj, A. K. Cheetham, and B. Raveau, J. Phys.: Condens. Matter **12**, R83, 2000.

[30] M. Uehara, S. Mori, C. H. Chen and S. W. Cheong, Nature **399** 560 (1999).

[31] F. Fath, S. Freisem, A. A. Menovsky, Y. Tomioka, J. Aarts and J. A. Mydosh, Science **285**, 1540 (1999).

[32] L. Zhang, C. Israel, A. Biswas, R. L. Greene and A. de Lozanne, Science **298**, 805 (2002).

[33] Y. Tokura, Rep. Prog. Phys. **69**, 797 (2006).

[34] H. Kuwahara, Y. Tomioka, A. Asamitsu, Y. Moritomo, and Y. Tokura, Science **270**, 961 (1995).

[35] K. Miyano, T. Tanaka, Y. Tomioka, and Y. Tokura, Phys. Rev. Lett. **78**, 4257 (1997).

[36] M. Fiebig, K. Miyano, Y. Tomioka, and Y. Tokura, Science **280**, 1925 (1998).

[37] A. Asamitsu, Y. Tomioka, H. Kuwahara, and Y. Tokura, Nature (London) **388**, 50 (1997).

[38] A. Guha, N. Khare, A. K. Raychaudhuri, and C. N. R. Rao, Phys. Rev. B **62**, R11941 (2000); A. Guha, A. Ghosh, A. K. Raychaudhuri, S. Parashar, A. R. Raju and C. N. R. Rao, Appl. Phys. Lett. **75**, 3381 (1999).

[39] R. Y. Gu, Z. D. Wang, and C. S. Ting, Phys. Rev. B **67**, 153101 (2003).

[40] A. Sawa, Materialstoday **11**, 28 (2008).

[41] For a short review, see N. A. Tulina, Physics-Uspekhi **50**, 1171 (2007).

[42] A. Beck, J. G. Bednorz, Ch. Gerber, C. Rossel, and D. Widmer, Appl. Phys. Lett. **77**, 139 (2000).

[43] M. Quintero, P. Levy, A. G. Leyva, and M. J. Rozenberg, Phys. Rev. Lett. **98**, 116601 (2007); A. Baikalov, Y. Q. Wang, B. Shen, B. Lorenz, S. Tsui, Y. Y. Sun, Y. Y. Xue, and C. W. Chu, Appl. Phys. Lett. **83**, 957 (2003).

[44] N. A. Tulina, G. A. Emelchenco, A. B. Kulakov, Phys. Lett. A **204**, 74 (1995); N. A. Tulina, Physica C **333**, 214 (2000); N. A. Tulina, S. A. Zver'kov, Y. M. Mukovskii, and D. A. Shulyatev, Europhys. Lett. **56**, 836 (2001).

[45] R. Fors, S. I. Khartsev, and A. M. Grishin, Phys. Rev. B **71**, 045305 (2005).

[46] T. Oka, and N. Nagaosa, Phys. Rev. Lett. **95**, 266403 (2005).

[47] D. C. Kim, S. Seo, S. E. Ahn, D.-S. Suh, M. J. Lee, B.-H. Park, I. K. Yoo, I. G. Baek, H.-J. Kim, E. K. Yim, J. E. Lee, S. O. Park, H. S. Kim, U-In Chung, J. T. Moon, and B. I. Ryu, Appl. Phys. Lett. **88,** 202102 (2006).

[48] B. J. Choi, D. S. Jeong, S. K. Kim, C. Rohde, S. Choi, J. H. Oh, H. J. Kim, C. S. Hwang, K. Szot, R. Waser, B. Reichenberg, and S. Tiedke, J. Appl. Phys. **98,** 033715 (2005).

[49] J. G. Simmons, and R. R. Verderber, Proc. R. Soc. Lond. A **301,** 77 (1967).

[50] A.Sawa, T. Fujii, M. Kawasaki, and Y. Tokura, Appl. Phys. Lett. **88,** 232112 (2006).

[51] T. Fujii, M. Kawasaki, A. Sawa, H. Akoh, Y. Kawazoe, and Y. Tokura, Appl. Phys. Lett. **86,** 012107 (2005).

[52] G. I. Meijer, U. Staub, M. Janousch, S. L. Johnson, B. Delley, and T. Neisius, Phys. Rev. B **72,** 155102 (2005).

[53] L. Esaki, R. B. Laibowitz, and P. J. Stiles, IBM Tech. Discl. Bull. **13,** 2161 (1971).

[54] H. Kohlstedt, N. A. Pertsev, J. R. Contreras, and R. Waser, Phys. Rev. B **72,** 125341 (2005); E. Y. Tsymbal, and H. Kohlstedt, Science **313,** 181 (2006).

[55] L.V. Panina, and K.Mohri, Appl Phys Lett. **65**, 1189 (1994).

[56] J. E. Lenz, *A Review of Magnetic Sensors*. Proc IEEE **78**, 973 (1990); T.Meydan, J. Magn. Magn. Mater **133**, 525 (1994).

[57] P.Ripka (Ed.), *Magnetic Sensors and Magnetometers* (Artech House Publishers, London, 2001).

[58] M. Vazquez, and A. Hernando, J Phys D: Appl Phys **29**, 939 (1996); H. Chiriac, T. A. Ovari, Prog Mater Sci **40**, 333 (1996).

[59] M. Vazquez, J Magn. Magn. Mater, **226** 693 (2001); M. Knobel, and K. R. Pirota, J Magn. Magn. Mater, **242** 33 (2002).

[60] M. Knobel, M. Vazquez, L. Kraus, *Giant magnetoimpedance in Handbook of magnetic materials*, K. H. Buschow (Ed.), vol. 15. (Elsevier Science, Amsterdam, 2003); L. Kraus, Sens Acta A **106**, 187 (2003); C. Tannous, and J. Gieraltowski, J Mater. Sci. Mater for Elec., **15**, 125 (2004).

[61] L. D. Landau, E. M. Lifshitz and L. P. Pitaevskii, *Electrodynamics of Continuous Media*, 2nd ed. (Butterworth-Heinemann, Oxford, 2004).

[62] M. Ziese, Rep. Prog. Phys. **65** 143 (2002).

[63] K. A. Gschneidner, Jr., V. K. Pecharsky, and A. O. Tsokol, Rep. Prog. Phys. **68**, 1479 (2005), and references therein.

[64] M. H. Phan, S. C. Yu, J. Magn. Magn. Mater. **308**, 325 (2007) and references therein.

[65] J. Mira, J. Rivas, F. Rivadulla, C. Vázquez-Vázquez, and M. A. López-Quintela, Phys. Rev. B **60**, 2998 (1999).

[66] A. Asamitsu, Y. Moritomo, Y. Tomioka, T. Arima, and Y. Tokura, Nature (London) **373**, 407 (1995).

[67] H. Terashita, B. Myer, and J. J. Neumeier, Phys. Rev. B **72**, 132415 (2005); G. F. Dionne, J. Appl. Phys. **101,** 09C509 (2007).

[68] R. Mahendiran, B. G. Ueland, P. Schiffer, A. Maignan, C. Martin, M. Hervieu, B. Raveau, M. R. Ibarra, and L. Morellon, e-print arXiv:cond-mat/0306223 (2003).

[69] C. N. R. Rao, *Chemical Approaches to the Synthesis of Inorganic Materials* (Wiley Eastern Ltd., New Delhi, 1994).

[70] B. D. Cullity, *Elements of X-ray Diffraction* (Addison-Wesley, Massachusetts, 1972); H. P. Klug, and L. E. Alexander, *X-ray Diffraction Procedures* (John Wiley & Sons, New York, 1954).

[71] *Agilent Impedance Measurement Handbook* (4th edition, Agilent Technologies), downloaded from web http://www.home.agilent.com/agilent/home.jspx?cc=US&lc=eng

[72] A. Sawa, T. Fujii, M. Kawasaki, and Y. Tokura, Appl. Phys. Lett. **85**, 4073 (2004).

[73] A. Odagawa, H. Sato, I. H. Inoue, H. Akoh, M. Kawasaki, Y. Tokura, T. Kanno, and H. Adachi, Phys. Rev. B **70**, 224403 (2004).

[74] A. Wahl, S. Mercone, A. Pautrat, M. Pollet, Ch. Simon, and D. Sedmidubsky, Phys. Rev. B **68**, 094429 (2003).

[75] N. Noginova, G. B. Loutts, E. S. Gillman, V. A. Atsarkin, and A. A. Verevkin, Phys. Rev. B **63**, 174414 (2001).

[76] A. K. Debnath, and J. G. Lin, Phys. Rev. B **67**, 064412 (2003).

[77] Y. F. Chen, M. Ziese, and P. Esquinazi, Appl. Phys. Lett. **89**, 082501(2006); A. S. Carneiro, R. F. Jardim and F. C. Fonseca, Phys. Rev. B **73**, 012410 (2006).

[78] M. Tokunaga, Y. Tokunaga, and T. Tamegai, Phys. Rev. Lett. **93**, 037203 (2004); A. Palanisami, M. B. Weissman, and N. D. Mathur, Phys. Rev. B **71**, 094419 (2005).

[79] G. Cao, J. Zhang, S. Wang, J. Yu, C. Jing, S. Cao, and X. Shen, J. Magn. Magn. Mater. **301**, 147 (2006); T. Kimura, Y. Tomioka, R. Kumai, Y. Okimoto, and Y. Tokura, Phys. Rev. Lett. **83**, 3940 (1999).

[80] F. Millange, S. de Brion, and G. Chouteau, Phys. Rev. B **62**, 5619 (2000).

[81] V. Ponnambalam, S. Parashar, A. R. Raju, and C. N. R. Rao, Appl. Phys. Lett. **74**, 206 (1999); D. Hsu, J. G. Lin, and W. F. Wu, *ibid.* **88**, 222507 (2006).

[82] C. H. Ahn, J.-M. Triscone, and J. Mannhart, Nature (London) **424,** 1015 (2003); R. Waser and M. Aono, Nature Mater. **6**, 833 (2007).

[83] S. Q. Liu, N. J. Wu, and A. Ignatiev, Appl. Phys. Lett. **76**, 2749 (2000).

[84] B. Raveau, C. Martin, A. Maignan, M. Hervieu, and R. Mahendiran, Physica C **341**, 711 (2000); R. Mahendiran, M. Hervieu, A. Maignan, C. Martin, and, B. Raveau, Solid State Commun. **114**, 429 (2000).

[85] R. Shoji, S. Mori, N. Yamamoto, A. Machida, Y. Moritomo, and T. Katsufuji, J. Phys. Soc. Jpn. **70**, 267 (2001); S. Mori, R. Shoji, N. Yamamoto, A. Machida, Y. Moritomo, and T. Katsufuji, ibid. **71**, 1280 (2002)

[86] R. Mahendiran, B. Raveau, M. Hervieu, C. Michel, and A. Maignan, Phys. Rev. B **64**, 064424 (2001).

[87] S. B. Roy, P. Chaddah, V. K. Pecharsky, and K. A. Gschneidner Jr., Acta Mater. **56**, 5895 (2008).

[88] P. Kushwaha, R. Rawat, and P. Chaddah, J. Phys.: Condens. Matter **20**, 022204 (2008); R. Mahendiran, A. Maignan, C. Martin, M. Hervieu, and B. Raveau, arXiv:cond-mat/0303007v1 (2003).

[89] R. Schmidt, Phys. Rev. B **77**, 205101 (2008).

[90] S. T. Hsu, T. Li, and N. Awaya, J. Appl. Phys. **101**, 024517 (2007).

[91] M. J. Rozenberg, I. H. Inoue, and M. J. Sánchez, Phys. Rev. Lett. **92**, 178302, (2004).

[92] N. Žurauskienė, Thin Solid Films **515**, 576 (2006)

[93] D. M. Kroll, Phys. Rev. B **9,** 1669 (1974).

[94] Y. F. Chen, and M. Ziese, J. Appl. Phys. **101,** 103902 (2007).

[95] T. Mori, T. Ozawa, Y. Bando, T. Kawamoto, S. Niizeki, H. Mori, and I. Terasaki, Phys. Rev. B **79,** 115108 (2009).

[96] R. Mahendiran, A. Maignan, S. Hébert, C. Martin, M. Hervieu, B. Raveau, J.F. Mitchell, and P. Schiffer, Phys. Rev. Lett. **89**, 286602 (2002).

[97] K. Kumar, A. K. Pramanik, A. Banerjee, and P. Chaddah, S. B. Roy, S. Park, C. L. Zhang, and S.-W. Cheong, Phys. Rev. B. **73**, 184435 (2006).

[98] M. Tokunaga, H. Song, Y. Tokunaga, and T. Tamegai, Phys. Rev. Lett. **94**, 157203 (2005).

[99] R. Rawat, K. Mukherjee, K. Kumar, A. Banerjee and P. Chaddah, J. Phys.: Condens. Matter. **19**, 256211 (2007).

[100] Y. Yamato, M. Matsukawa, Y. Murano, R. Suryanarayanan, S. Nimori, M. Apostu, A. Revcolevschi, K. Koyama, N. Kobayashi, Appl. Phys. Lett. **94**, 092507 (2009).

[101] M. S. Reis, V. S. Amaral, J. P. Araújo, P. B. Tavares, A. M. Gomes, and I. S. Oliveira, Phys. Rev. B **71**, 144413 (2005).

[102] L. Ghivelder, R.S. Freitas, M.G. das Virgens, M.A. Continentino, H. Martinho, L. Granja, M. Quintero, G. Leyva, P. Levy, F. Parisi, Phys. Rev. B **69**, 214414 (2004).

[103] M. Roy, J. F. Mitchell, A. P. Ramirez, P. Schiffer, Phys. Rev. B **62**, 13876 (2000).

[104] B. J. O'Brien, C. S. Wallace, J. Appl. Phys. **29**, 1010 (1958).

[105] R. T. Delves, Rep. Prog. Phys. **28**, 249 (1965).

[106] Z. B. Guo, Y. W. Du, J. S. Zhu, H. Huang, W. P. Ding, and D. Feng, Phys. Rev. Lett. **78**, 1142 (1997).

[107] X. Bohigas, J. Tejada, E. del Barco, X. X. Zhang, and M. Sales, Appl. Phys. Lett. **73**, 390 (1998).

[108] H. Terashita, J. J. Garbe, and J. J. Neumeier, Phys. Rev. B **70**, 094403 (2004); J. S. Amaral, N. J. O. Silva and V. S. Amaral, Appl. Phys. Lett. **91**, 172503 (2007).

[109] D. S. Rodbell and C. P. Bean, J. Appl. Phys. **33**, 1037 (1962).

[110] V. K. Pecharsky, and K. A. Gschneidner, Jr. Phys. Rev. Lett. **78**, 4494 (1997); L. Morellon, J. Blasco, P. A. Algarabel, and M. R. Ibarra, Phys.Rev. B **62**, 1022 (2000).

[111] O. Tegus, E. Brück, K. H. J. Buschow, and F. R. de Boer, Nature **415**, 150 (2002).

[112] F. Hu, B. Shen, and J. Sun, Appl. Phys. Lett.**76**, 3460 (2000); F. Casanova, X. Batlle, A. Labarta, J. Marcos, L. Mañosa, and A. Planes. Phys. Rev. B **66**, 100 401 (R) (2002).

[113] C. Martin, A. Maignan, M. Hervieu, and B. Raveau, Phys. Rev. B **60**, 12191 (1999); A. I. Kurbakov, A. V. Lazuta, V. A. Trounov, I. I. Larionov, C. Martin, A. Maignan, and M. Hervieu, Phy. Rev. B. **72**, 184432 (2005).

[114] L. M. Fisher, A. V. Kalinov, I. F. Voloshin, N. A. Babushkina, D. I. Khomskii, Y. Zhang, and T. T. M. Palstra, Phy. Rev. B. **70**, 212411 (2004); M. Egilmez, K. H. Chow, J. Jung, and Z. Salman, Appl. Phys. Lett. **90**, 162508 (2007).

[115] Y. Tomioka, H. Hiraka, Y. Endoh, and Y. Tokura, Phys. Rev. B **74**, 104420 (2006).

[116] R. P. Borges, F. Ott, R. M. Thomas, V. Skumryev, J. M. D. Coey, J. I. Arnaudas, and L. Ranno, Phy. Rev. B. **60**, 12847 (1999).

[117] J. M. De Teresa, M. R. Ibarra, P. Algarabel, L. Morellon, B. Garcia-Landa, C. Marquina, C. Ritter, A. Maignan, C. Martin, B. Raveau, A. Kurbakov, and V. Trounov, Phys. Rev. B **65**, R100403 (2002).

[118] E. Saitoh, Y. Tomioka, T. Kimura, and Y. Tokura, J. Phys. Soc. Jpn. **69**, 2403 (2000).

[119] P. Sarkar, P. Mandal, and P. Choudhury, Appl. Phys. Lett. **92**, 182506 (2008).

[120] P. M. Woodward, T. Vogt, D. E. Cox, A. Arulraj, C. N. R. Rao, P. Karen, and A. K. Cheetham, Chem. Mater. **10**, 3652 (1998).

[121] E. M. Levin and P. M. Shand, J. Magn. Magn. Mater. **311**, 675 (2007).

[122] S. K. Banerjee, Phys. Lett. **12,** 16 (1964).

[123] K. A. Gschneidner, Jr., V. K. Pecharsky, and A. O. Tsokol, Rep. Prog. Phys. **68**, 1479 (2005), and references therein.

[124]I. S. Jacobs and C. P. Bean, *Magnetism*, edited by G. T. Rado and H. Suhl (Academic, New York, 1963).

[125] J. I. Gittleman, Y. Goldstein, and S. Bozowski, Phys. Rev. B **5**, 3609 (1972).

[126] D. T. Morelli, A. M. Mance, J. V. Mantese, and A. L. Micheli, J. Appl. Phys. **79**, 373 (1996).

[127] X. X. Zhang, J. Tejada, Y. Xin, G. F. Sun, and K. W. Wong, Appl. Phys. Lett. **69**, 3596 (1996).

[128] Y. Sun, X. Xu, and Y. Zhang, J. Magn. Magn. Mater. **219**, 183 (2000).

[129] V. K. Pecharsky, and K. A. Gschneidner, Jr., Appl. Phys. Lett. **70**, 3299 (1997).

[130] K. A. Gschneidner, Jr., and V. K. Pecharsky, J. Appl. Phys. **85**, 5365 (1999).

[131] Y. Sun, W. Tong, and Y. H. Zhang, J. Magn. Magn. Mater. **232**, 205 (2001).

[132] S. K. Barik, and R. Mahendiran, J. Appl. Phys. **107**, 093906 (2010).

[133] R. Mahendiran, M. Hervieu, A. Maignan, C. Martin, and B. Raveau, Solid State Commun. **114**, 429 (2000).

[134] L. Jia, G. J. Liu, and J. Z. Wang, J. R. Sun, H. W. Zhang, and B. G. Shen, Appl. Phys. Lett. **89**, 122515 (2006).

[135] J. Gao, S. Q. Shen, T. K. Li, and J. R. Sun, Appl. Phys. Lett. **82**, 4732 (2003); J. Gao, and F. X. Hu, Appl. Phys. Lett. **86**, 092504 (2005).

[136] E. Rozenberg, V. Markovich, Ya. Yuzhelevskii, G. Gorodetsky, and M. Ziese, J. Appl. Phys. **95**, 7103 (2004).

[137] A. I. Abramovich, L. I. Koroleva, A. V. Michurin, O. Y. Gorbenko, and A. R. Kaul, Physica B **293**, 38 (2000).

[138] L. Sudheendra, and C. N. R. Rao, J. Appl. Phys. **94**, 2767 (2003).

[139] A. V. Gurevich, and R. G. Mints, Rev. Mod. Phys. **59**, 941 (1987).

[140] J. M. D. Coey, M.Viret, and S. von Molnar, Adv. Phys. **48**, 167 (1999).

[141] M. Ziese, G. Heydon, R. Hohne, P. Esquinazi, and J. Dienelt, Appl. Phys. Lett. **74**, 1481 (1999); J. B. Philipp, C. Höfener, S. Thienhaus, J. Klein, L. Alff, and R. Gross, Phys. Rev. B **62**, R9248 (2000).

[142] M. Bowen, M. Bibes, A. Barthélémy, J.- P. Contour, A. Anane, Y. Lemaitre, and A. Fert, Appl. Phys. Lett. **82**, 233 (2003).

[143] L. M. Wang, C. –C. Liu, H. C. Yang, and H. E. Horng, J. Appl. Phys. **95**, 4928 (2004).

[144] S. D. Tyagi, S. E. Lofland, M. Dominguez, S. M. Bhagat, C. Kwon, M. C. Robson, R. Ramesh and T. Venkatesan, Appl. Phys. Lett. **68**, 2893 (1996); V. V. Srinivasu, S. E. Lofland, and S. M. Bhagat, J. Appl. Phys. **83**, 2866 (1998).

[145] J. Wosik, L.-M. Xie, M. Strikovski, J. H. Miller, Jr., and P. Przyslupski, Appl. Phys. Lett. **74**, 750 (1999).

[146] D. L. Lyfar, S. M. Ryabchenko,V. N. Krivoruchko, S. I. Khartsev, and A. M. Grishin, Phys. Rev. B **69**, 100409 (2004); M. Golosovsky, P. Monod, P. K. Muduli, R. C. Budhani, L. Mechin, and P. Perna, Phys. Rev. B **76**, 184414 (2007).

[147] J. Hu, H. Qin, H. Niu, L. Zhu, J. Chen, W. Xiao, and Y. Pei, J. Magn. Magn. Mater. **261**, 105 (2003); G. M. B. Castro, A. R. Rodrigues, F.L.A. Machado, R.F. Jardim, J. Magn. Magn. Mater. **272**, 1848 (2004), and references therein.

[148] P. Dutta, P. Dey and T. K. Nath, J. Appl. Phys. **102,** 073906 (2007).

[149] T. Shimura, T. Hayashi, Y. Inaguma, and M. Itoh, J. Solid State Chem. **124,** 250 (1996); R. N. Singh, C. Shivakumara, N. Y. Vasanthacharya, S. Subramanian, M. S. Hegde, H. Rajagopal, and A. Sequeira, J. Solid State Chem. **137,** 19 (1998).

[150] H. Y. Hwang, S. -W. Cheong, N. P. Ong, and B. Batlogg, Phys. Rev. Lett. **77**, 2041 (1996); R. Mahesh, R. Mahendiran, A. K. Raychaudhuri, and C. N. R. Rao, Appl. Phys. Lett. **68**, 2291 (1996).

[151] Y. Tokura, and Y. Tomioka, J. Magn. Magn. Mater. **200**, 1 (1999).

[152] P. Majumdar and P. B. Littlewood, Nature (London) **395**, 479 (1998).

[153] A. A Belik, and E. Takayama-Muromachi, J. Phys.: Condens. Matter. **20**, 025211 (2008).

[154] L. S. Lakshmi, K. Dörr, K. Nenkov, A. Handstein, K. -H. Müller, and V. S. Sastry, J. Phys.: Condens. Matter. **19,** 216218 (2007).

[155] M. D. Vannette, A. S. Sefat, S. Jia, S. A. Law, G. Lapertot, S.L. Bud'ko, P. C. Canfield, J. Schmalian and R. Prozorov, J. Magn. Magn. Mater. **320**, 354 (2008).

[156] R. Mahendiran, and P. Schiffer, Phys. Rev. B **68**, 024427 (2003).

[157] T. Brown, W. Li, H. P. Kunkel, X. Z. Zhou, G. Williams, Y. Mukovskii, and A. Arsenov, J. Phys.: Condens. Matter. **17**, 5997 (2005).

[158] F. L. A. Machado, B. L. da Silva, S. M. Rezende, and C. S. Martins, J. Appl. Phys. **75**, 6563 (1994).

[159] L. V. Panina, K. Mohri, T. Uchiyama, M. Noda, and K. Bushida, IEEE Trans. Magn. **31**, 1249 (1995).

[160] M. R. Britel, D. Ménard, L. G. Melo, P. Ciureanu, A.Yelon, R. W. Cochrane, M.Rouabhi, and B. Cornut, Appl. Phys. Lett. **77**, 2737 (2000); D.Ménard, M.Britel, P.Ciureanu, A.Yelon, V. P. Paramonov, A. S.Antonov, P.Rudkowski, and J. O. Ström-Olsen, J. Appl. Phys. **81**, 4032 (1997).

[161] T. E. Hasty, J. Appl. Phys. **35**, 1434 (1964).

[162] L. Kraus, Z. Frait, K. R. Pirota, and H. Chiriac, J. Magn. Magn. Mater. **254**, 399 (2003).

[163] K. R. Pirota, L. Kraus, M. Knobel, P. G. Pagliuso, and C. Rettori, Phys. Rev. B **60**, 6685 (1999).

[164] L. Kraus, A. N. Medina, F. G. Gandra, M. Knobel, and V. Haslar, Mater. Sci. Forum **302**, 224 (1999).

[165] J. G. S. Duque, C. Gomez-Polo, A. Yelon, P. Ciureanu, A. E. P. de Araujo, and M. Knobel, J. Magn. Magn. Mater. **271**, 390 (2004).

[166] D. de Cos, V. N. Lepalovskij, G. V. Kurlyandskaya, A. Garcia-Arribas, and J. M. Barandiaran, J. Magn. Magn. Mater. **320**, e954 (2008).

[167] D. de Cos, A. Garcia-Arribas, and J. M. Barandiaran, IEEE Trans. Magn. **41**, 3649 (2005); J. M. Barandiaran, A. Garcia-Arribas, and D. de Cos, J. Appl. Phys. **99**, 103904 (2006).

[168] I. Maartense, and C. W. Searle, J. Appl. Phys. **42**, 2349 (1971).

[169] E. Saitoh, H. Miyajima, T. Yamaoka and G. Tatara, Nature **432**, 203 (2004).

[170] J. Hu, and H. Qin, J. Magn. Magn. Mater. **234**, 419 (2001); H. Qin, J. Hu, J. Chen, Y. Wang, and Z. Wang, J. Appl. Phys. **91**, 10003 (2002); H. Qin. J. Hu, B. Li, Y. Hao, J. Chen, and M. Jiang, J. Magn.Magn. Mater. **320**, 2770 (2008).

[171] M. Vázquez, Y.-F. Li, and D.-X. Chen, J. Appl. Phys. **91**, 6539 (2002).

[172] K. C. Mendes, and F. L. A. Machado, J. Magn. Magn. Mater. **177**, 111 (1998); V. Zhukova, N. A. Usov, A. Zhukov, and J. Gonzalez, Phys. Rev. B **65**, 134407 (2002).

[173] A. Rebello, and R. Mahendiran, Solid. State. Commun. **149**, 673 (2009); A. Rebello, and R. Mahendiran, Appl. Phys. Lett. **94**, 112107 (2009).

[174] A. Rebello, and R. Mahendiran, Appl. Phys. Lett. **96**, 152504 (2010).

[175] A. Rebello, and R. Mahendiran, Solid. State. Commun. **150**, 961 (2010); A. Rebello, and R. Mahendiran, Appl. Phys. Lett. **95**, 232509 (2009).

[176] A. Rebello, and R. Mahendiran, Appl. Phys. Lett. **93**, 232501 (2008), and references therein.

[177] A. Rebello, V. B. Naik, and R. Mahendiran, J. Appl. Phys. **106**, 073905 (2009); A. Rebello, and R. Mahendiran, Europhys. Lett. **86**, 27004 (2009).

[178] A. Rebello, C. L. Tan, and R. Mahendiran, Solid. State. Commun. **149**, 1204 (2009); S. K. Barik, A. Rebello, C. L. Tan, and R. Mahendiran, J. Phys. D: Appl. Phys. **41**, 022001 (2008).

[179] A. Rebello, and R. Mahendiran, Appl. Phys. Lett. **96**, 032502 (2010).

[180] D. B. Strukov, G. S. Snider, D. R. Stewart, and R. S. Williams, Nature **453** 80 (2008); L. O. Chua, IEEE Trans. Circuit Theory **18**, 507 (1971).